Time resolved 2D Doppler imaging of ion dynamics

Inauguraldissertation

zur

Erlangung des akademischen Grades eines

doctor rerum naturalium (Dr. rer. nat.)

an der Mathematisch-Naturwissenschaftlichen Fakultät

der

Ernst-Moritz-Arndt-Universität Greifswald

vorgelegt von
Jinil Chung
geboren am 19.02.1976
in Seoul

Greifswald, im Juni 2004

Dekan:	....
1. Gutachter:	....
2. Gutachter:	....
Tag der Promotion:	....

Abstract

Imaging sensor technologies such as CCDs (charge coupled devices) and CMOS (complementary metal-oxide-semiconductor) have made remarkable progress in recent years. There are now many imaging diagnostics using sensors with good temporal and spatial resolutions and being used in fusion research devices. Since 2-dimensional (2D) imaging considerably improves the investigation of 3-dimensional (3D) structural physics, it is very important for fusion plasma diagnostics. In stellarator devices, a novel divertor concept called island divertors is a good example. Island divertors are inherently asymmetrical in the poloidal and toroidal directions and therefore they are fully 3D structures.

Within the scope of this thesis the first 2D imaging MOSS (Modulated Optical Solid State) spectrometer using a high-resolution 2D CCD camera was constructed to study ion temperatures and flow velocities using the 468.6 nm He II line emission. The MOSS spectrometer is essentially a Fourier-transform spectrometer about a fixed delay. It is designed to function in the optical region of the spectrum, and the heart of the device is electro-optic birefringence crystals that modulate the wave delay. This MOSS spectrometer uses a CCD camera as a detector and is used with suitable imaging optics so that the system can be used to measure 2-dimensional ion temperature and flow velocity distributions.

To construct the MOSS spectrometer we have created a coherence simulation code and its proper model for the He II line at 468.6 nm and C III line at 464.9 nm. The simulation code provides a very effective way to identify suitable isolated spectral lines and to determine the optimum thickness of the required birefringence crystals. To test the suitability of such a system as a possible W7-X divertor diagnostic, initial experiments were performed in W7-AS stellarator. This has allowed us to complete the development of the 2D MOSS spectrometer. After the experimental campaign, the MOSS spectrometer construction was finished, and it was installed in the WEGA stellarator to study the poloidal profiles of the ion temperature and flow velocity at different toroidal positions.

More detailed studies were carried out on the WEGA stellarator by changing the primary machine control parameters such as Electron Cyclotron Resonance Heating (ECRH) power and neutral gas pressure. Resonance magnetic field and rotational transform scan experiments were also performed to study the ion temperature profile behavior and poloidal rotation velocities in WEGA plasmas. The ion temperature of Helium plasmas in WEGA is $1.5 - 2.0$ eV at maximum (26 kW) ECRH power. The

temperature of a mixed gas (H_2+He) plasma was $2.0 - 2.5$ eV, and the temperature increased when the neutral gas pressure was decreased. The ion temperature profile gets broader and flatter as the power is increased.
The poloidal flow velocity was negative at the top of the plasma, and positive at the bottom of the plasma. The speed was around $500 - 1000$ m/s, and it was somewhat faster at higher ECRH power. To make sure that the velocity was induced by the plasma we reversed the toroidal magnetic field direction and measured the line shift using the Echelle grating spectrometer for both the standard and reversed toroidal magnetic field directions. The ion temperature result from the MOSS spectrometer was also crosschecked with an Echelle grating spectrometer. Using the measured plasma parameters the ion energy confinement time is estimated to be around 0.1 ms for pure Helium plasmas in WEGA at the maximum ECRH power. The behavior of the ion temperature and poloidal flow, and the status of the ECR heating in WEGA are discussed.

Contents

1

Introduction

1.1 Nuclear fusion and magnetic confinement

Energy production by nuclear fusion and fission is based on the fact that the mass difference between an atomic nucleus and the sum of the constituent nucleons is a maximum near mass number $A \approx 56$. This mass difference represents the nuclear binding energy which can be calculated by Einstein's well-known energy-mass equation, $E = \Delta mc^2$. Here the energy release per nucleon is of the order of 1 MeV for the fission reaction, and several times greater for the fusion reaction. To induce the fusion reaction between two positively charged nuclei, a large amount of energy is needed to overcome the mutual repulsion. According to the classical theory (Coulomb potential) the required energy is $E = 0.28 Z_1 Z_2$ MeV, where Z_1 and Z_2 are the atomic numbers of the two reacting nuclei. This means that the kinetic energy required for fusion is impractically high, even for the H-H reaction. However, as the α-particle decay occurs already at room temperature (found in 1928 by Gamov [1]) via the tunnelling effect, fusion reactions can occur at reasonable temperatures required to overcome the Coulomb barrier. The maximum cross-section occurs at just over 100 keV [2]. Since the cross-section of pure hydrogen ($_1H^1$) is too small, Deutrium, Trituim, and light Helium are preferred as *fuel* for the nuclear fusion reaction. Possible candidates for fusion energy are

$$\begin{aligned} D - T &\longrightarrow {}^4\mathrm{He} + \mathrm{n} + 17.59\,\mathrm{MeV} \\ D - D &\longrightarrow {}^3\mathrm{He} + \mathrm{n} + 3.27\,\mathrm{MeV}(50\%) \\ &\quad\; or \quad \mathrm{T} + \mathrm{p} + 4.03\,\mathrm{MeV}(50\%) \\ D - {}^3\mathrm{He} &\longrightarrow {}^4\mathrm{He} + \mathrm{p} + 18.35\,\mathrm{MeV}. \end{aligned}$$

The most promising method to achieve the fusion reaction (sometimes called thermonuclear fusion) is to heat and to confine the fuel as a plasma at a sufficiently high temperature. In the plasma state at high temperature, all atoms are completely ionized and the thermal velocities of the ionized particles are high enough to produce fusion reactions. The temperature is usually not as high as the corresponding

maximum cross-section energy because the reaction occurs in the high energy tail of the Maxwellian velocity distribution of the ionized particles. For example, the necessary temperature is around 10 keV for the D-T reaction.

Two types of toroidal magnetic confinement methods have been developed to overcome the end losses in the linear magnetic confinement devices of the 1950s. One is the stellarator which was invented in 1951 by Lyman Spitzer Jr. in Princeton, USA [3], and the other, the tokamak, was proposed the following year by Tamm and Sakharov in Russia [4].

The main difference between the two toroidal confinement concepts is the method of twisting a simple toroidal magnetic field in order to avoid an outward $E \times B$ drift of the whole plasma. A tokamak provides the necessary twist by passing a current in the toroidal direction through the plasma, and a stellarator provides the twist by deforming the magnetic field structure itself. The advantage of the stellarator is that the field line twist is determined by external currents only, but it is of three-dimensional geometry and much more difficult to construct. Classical stellarators such as WEGA [5] and W7-A [6] have been replaced by modular stellarators such as W7-AS [7] and W7-X [8], where the planar toroidal coils and the helical coils have been replaced by a modular system of non-planar coils. As a consequence of the twisting of the magnetic field lines in tokamaks and stellarators, plasma parameters are usually constant.

The normalized plasma pressure

$$\beta = \frac{< p >}{\mathbf{B}^2/2\mu_0} \tag{1.1}$$

and the energy confinement time

$$\tau_E = \frac{W_{plasma}}{P_{heat}} \tag{1.2}$$

are of particular importance, since they are measures for the efficiency of the confinement. The fusion power output roughly scales as p^2, and $\mathbf{B}$ and P_{heat} are provided externally.

Today, the use of superconducting magnetic coils is mandatory for steady-state operation and for obtaining a positive power balance. The construction or upgrading of superconducting stellatators and tokamaks around the world, such as W7-X, LHD [9], Tore Supra [10], KSTAR [11], and JT-60SC [12], will provide excellent experience for the construction of the International Thermonuclear Experimental Reactor (ITER) [13].

1.2 Classical plasma spectroscopy

The accurate diagnosis of a plasma without disturbing it, such as by spectroscopic methods, is very important for fusion research devices. Hence it is of great interest to improve such diagnostic methods for better understanding of the physical phenomena of the plasma.
Spectroscopy is the science of using the electromagnetic emission spectrum to understand what something is made of. Here the word *spectrum* comes from the Latin *spectare*, which means *to make a display out of something*, and the electromagnetic spectrum covers all energies of light extending from low energy radio waves through very high energy X and γ rays. In fusion research, a variety of spectroscopic diagnostics covering the entire spectrum range is being used to understand atomic processes and characterize physics parameters in high temperature plasmas. In the visible spectral region a commonly used instrument is the grating spectrometer, since it is easily available and well understood.

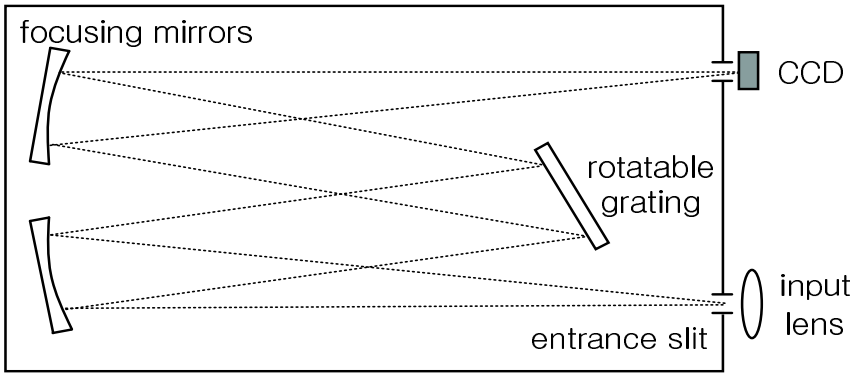

Figure 1.1: Principle layout of a Czerny-Turner grating spectrometer, consisting of a rotatable diffraction grating, focusing mirrors, an entrance and a detector.

The grating spectrometer is a device that allows precise measurements of the angle between two rays of light. Because the light from the source to be studied is often not a narrow beam like a laser, it must be gathered and focused by lenses. The light from the source is first passed through a slit, which should be as narrow as possible, consistent with letting enough light through to be visible. The light spreads out from the slit to the focusing mirror, which makes it into a parallel beam. The parallel beam of light then strikes the diffraction grating. From the grating, the light travels in various directions due to diffraction and interference. Depending on the position of the grating, light of a particular wavelength and order of interference will finally be focused on a CCD (Charge Coupled Device) chip. The spectrometer contains dispersive elements such as gratings. An object is imaged on an entrance slit, and the slit width determines the spectral resolution and optical throughput ($\equiv$ etendue $= \Omega \cdot A$). Spectral resolution is also determined by the grating constant and focal length. The element in the entire optical setup which has the lowest etendue determines the throughput of the system.

In the present work, a conventional grating spectrometer was used to find candidate lines for diagnostic development. An Echelle grating spectrometer (see Section 6.2.2) having very high spectral resolution was also used to crosscheck the result. This thesis reports on the design, theory, and construction of a time resolved 2-dimensional Doppler spectroscopic instrument using a MOSS (Modulated Optical Solid State) spectrometer (see Chapter 4). A proof-of-principle study is carried out in a low temperature plasma confinement experiment, the WEGA stellarator in Greifswald. A first attempt to use the camera on the fusion research device W7-AS is also reported.

1.3 Thesis structure

This thesis is structured as follows:

In Chapter 2 important broadening mechanisms are discussed with some examples of the He II line at 468.6 nm which will be studied in detail in this thesis. The results of these examples are very important for creating a simulation model which is discussed in Chapter 3. In Chapter 3 coherence simulations for the MOSS spectrometer construction are presented. The physical background of the simulation, simulation models and physical assumptions, and some important simulation results are discussed. In Chapter 4 the principles of the MOSS spectrometer and its performance are discussed from a theoretical view-point. Detailed measurement principles and experimental apparatus are also introduced in this chapter. Chapter 5 describes the first 2D MOSS spectrometer for W7-AS using a 2D CCD camera, and will conclude with a summary of the first test measurements made during the end of the W7-AS experimental campaign. Chapter 6 describes the experimental setup of the MOSS and Echelle grating spectrometer on the WEGA stellarator. A brief introduction to the WEGA stellarator is also given. In chapter 7 the experimental plasma physics results from the ECR heated Helium and mixed (H_2 + He) gas plasmas in the WEGA stellarator are presented. Ion temperature and poloidal flow velocity profiles as a function of time from machine control parameter changes, resonance magnetic field and rotational transform scan experiments, and some other interesting physics investigations are given in this chapter. Chapter 8 discusses the results of experimental studies shown in Chapter 7 including variations of poloidal profiles of the ion temperature and flow velocity for many different plasma conditions in the WEGA stellarator. The status of the ECR heating in the WEGA stellarator and estimations of the ion energy confinement time using a power balance equation are also discussed. Finally, chapter 9 summarizes and concludes the thesis work.

2

Broadening of Spectral Lines

The plasma is assumed to have a high enough temperature so that all the molecular bonds are broken and most of the atoms are ionized. Passive plasma spectroscopic techniques can be used to study the properties of the electrons and ions in the plasma by measuring the emitted spectral line profile of the electromagnetic radiation. The line emission profile is measured without any disturbance to the plasma. It contains information on the kinetic temperature of the emitting atom and the density of perturbing particles. This information can be estimated by understanding the dominant broadening mechanisms of the line emission. The line width is very sensitive to the local microfield around the emitting ions and the strong enough external fields. A spectral line is broadened by several mechanisms as described below:

Natural line broadening is the simplest broadening mechanism due to the finite lifetime of the excited states. Since natural line broadening is much smaller than the other broadening mechanisms, its effect is almost always completely negligible in applications of plasma spectroscopy. The shape of the natural spectral line is a Lorentzian.

Doppler broadening is due to the thermal velocity distribution of the emitting ions. The width of the Doppler broadening is proportional to the plasma temperature and inversely proportional to atomic mass. Under certain plasma conditions described in this thesis, the Doppler broadening is dominant. The resulting profile is a Gaussian.

Stark broadening is due to the electrostatic field generated by nearby ions, which split and shift the energy levels of the radiating ion. The Stark broadening is proportional to the electron density. The resulting profile is approximately Lorentzian. If the electron density is less than $10^{19}\,\mathrm{m}^{-3}$, it can be ignored in this thesis.

Zeeman splitting is the result of external magnetic fields by means of the Zeeman effect. The splitting depends on the magnetic field strength and the observation direction to the magnetic field. The splitting must be considered when external fields are strong compared to the ion temperature. The weak and strong field approximation of the Zeeman effect is considered in this thesis.

Instrumental broadening or instrument function is due to the optical instrument itself causing a broadening of the spectrum. It must be considered and corrected for all instruments.

The MOSS spectrometer measures the ion temperature by measuring the line broadening, it is very important to consider the possible broadening mechanisms in the experimental conditions such as plasma temperature, density, and the strength of external fields. In this chapter, the above important broadening mechanisms are discussed with some examples for the He II line at 468.6 nm which will be studied in detail in this thesis. The results of these examples are very important to create a simulation model which is discussed in the next chapter.

2.1 Natural line broadening

Natural broadening is the simplest broadening mechanism due to the finite lifetime of ionic excited states. The quantum mechanical treatment of radiation shows that the number N of excited atoms decreases according to [18]

$$N = N_0 e^{-\Gamma t} \tag{2.1}$$

where $1/\Gamma$ is the lifetime of the state in which the number N decays to N/e. In analogy to Equation (2.1), the amplitude of the emitted light waves decrease exponentially. The emitted waves have a damped oscillatory time dependence in complex notation,

$$A(t) \propto e^{i\omega_0 t} e^{-\Gamma t/2}. \tag{2.2}$$

Here $\omega_0 = (E_i - E_f)/\hbar$ is the frequency, where E_i and E_f are the energies of the initial and final atomic states, respectively. The Fourier transform of Equation (2.2) is proportional to

$$A(\tilde{\omega}) \propto \frac{1}{\sqrt{2\pi}} \int_{-\infty}^{\infty} \exp\left[-\left(\frac{\Gamma}{2} + i(\omega - \omega_0) \right) t \right] dt. \tag{2.3}$$

The spectral intensity distribution is proportional to the square of the amplitude of the emitted waves

$$I(\omega) \propto \left| A(\tilde{\omega}) \right|^2 . \tag{2.4}$$

The natural line profile has a Lorentzian shape

$$I(\omega) = \frac{\Gamma}{2\pi} \frac{1}{(\omega - \omega_0)^2 + (\Gamma/2)^2} \tag{2.5}$$

where a normalization factor has been added [16]. The natural line broadening amounts to about 10^{-5} nm. This is much less than other broadening mechanisms and is therefore negligible in applications of plasma spectroscopy. The most important spectral broadening processes in magnetized plasmas are Doppler effect, Pressure broadening, and Zeeman splitting. These are discussed in the following sections.

2.2 Doppler broadening

In a plasma the random motion of the radiating particles causes a Doppler broadening of spectral lines [14]. According to the Doppler effect, the frequency ω of the detected photon in the laboratory frame differs from the frequency ω_0 emitted in the frame of the moving ion by

$$\omega = \omega_0 \left(1 \pm \frac{v}{c}\right) \tag{2.6}$$

where c is the velocity of light, and v is the component of the emitter along the line of sight to the detector. The frequency is increased when the atoms are moving toward the detector, and decreased when they are moving away. At thermal equilibrium, the velocity has a Maxwell-Boltzmann distribution,

$$n(v)dv = N \left(\frac{m_0}{2\pi kT}\right)^{1/2} \exp\left(\frac{m_0 v^2}{2kT}\right) dv. \tag{2.7}$$

Here N is the total number of atoms, k is the Boltzmann constant, T is the absolute temperature, and m_0 is the atomic mass. According to Equation (2.6), a frequency displacement is associated with the velocity v. Thus we obtain an intensity distribution given by

$$I(\omega) = const \cdot \exp\left(-\frac{m_0 c^2 (\omega_0 - \omega)^2}{2kT\omega_0^2}\right) \tag{2.8}$$

which means that the effect of the ion motion in the plasma has a Gaussian shape. The Full-Width at Half-Maximum (FWHM) $\Delta\omega_D$ of a spectral line of mean frequency ω_0, due to thermal motion, is given by [17]

$$\Delta\omega_D = \frac{2\sqrt{2\ln 2}}{c} \omega_0 \left(\frac{kT}{m_0}\right)^{1/2} \tag{2.9}$$

where $\Delta\omega_D$ has units of frequency, and the temperature T is in K. According to the above equation, since the line width is inversely proportional to the atomic mass m_0, hydrogen gives the broadest spectral lines at a given temperature. For the sake

of convenience, the width of the Doppler broadening can be written as

$$\Delta\lambda_D = 7.716 \times 10^{-5}\lambda_0 \left(\frac{T_{eV}}{A_{rel}}\right)^{1/2} \tag{2.10}$$

or

$$T_{eV} = 1.68 \times 10^{8} A_{rel} \left(\frac{\Delta\lambda_D}{\lambda}\right)^{2}. \tag{2.11}$$

Here $\Delta\lambda_D$ has units of wavelength, T_{eV} is the temperature in eV, A_{rel} is the relative atomic mass, and λ_0 is the wavelength of the spectral lines. The width of the Doppler broadening depends only on the plasma temperature for a spectral line, and does not depend on electron density. For example, the width of the Doppler broadening for the 4686 Å He II line ($A_{rel} = 4$) at $T = 100\,\text{eV}$ is $\Delta\lambda_D = 0.181\,\text{Å}$. As we will later see the Doppler broadening is the dominant broadening mechanism described in this thesis.

2.3 Pressure broadening

Pressure broadening is due to the interaction of the radiating atom with surrounding particles which cause a frequency disturbance and hence an additional phase shift. The frequency disturbance is different for different types of interaction and are here discussed separately. Resonance broadening occurs between identical species and is confined to lines with the upper or lower level having an electric dipole transition to the ground state. Van der Waals broadening arises from the dipole interaction of an excited atom with the induced dipole of a ground state atom. Finally, Stark broadening is due to charged perturbers in plasmas. Here the resonance broadening and the Van der Waals broadening is generally of minor importance in plasma physics due to the fact that interaction with the dipole or higher multipole fields of neutral particles is always less efficient than interaction with the Coulomb field of perturbing ions or electrons [19]. Line shapes are often approximately Lorentzian. In this thesis, only the Stark broadening needs to be considered since there is no transition to the ground state for the candidate spectral lines studied in this thesis.

2.3.1 Resonance broadening

Resonance broadening, or self broadening, occurs only between identical species and is confined to lines with the upper or lower level having an electric dipole transition to the ground state. The FWHM may be estimated as [20]

$$\Delta\lambda_R \simeq 8.6 \times 10^{-30} \left(\frac{g_i}{g_k}\right)^{1/2} \lambda^2 \lambda_r f_r N_i \tag{2.12}$$

where $\Delta\lambda_R$ is in Å. If the wavelength of the observed line λ and the wavelength of the resonance line λ_r are in Å then g_k and g_i are the statistical weights of its upper and lower levels. f_r is the oscillator strength and N_i is the population density of the ground state in cm^{-3}.

2.3.2 Van der Waals broadening

In plasma spectroscopy the necessity of interpreting line profiles in terms of Van der Waals interaction arises only in cool gases with a low degree of ionization [19]. Van der Waals broadening occurs due to the dipole interaction of an excited atom with the induced dipole of a ground state atom. An approximate formula for the FWHM, strictly applicable to hydrogen and hydrogen-like ions only, is [20]

$$\Delta\lambda_W \simeq 3.0 \times 10^{16} \lambda^2 C_6^{2/5} \left(\frac{T}{\mu}\right)^{3/10} N \tag{2.13}$$

where μ is the atom-perturber reduced mass in units of u, N is the perturber density in cm^{-3}, and C_6 is the interaction constant.

2.3.3 Stark broadening

The central mechanism for Stark broadening is the electrostatic field generated by the perturber on the radiator. Stark broadening is valid when the interaction time between a perturber and the radiator is longer than the time between two collisions. This is the case when the perturber is an ion whose velocity is much less than that of electrons [16]. The FWHM $\Delta\lambda_0$ of a line in Å is given by [21]

$$\Delta\lambda_S = 2W \left(\frac{N_e}{10^{16}}\right) + 3.5A \left(\frac{N_e}{10^{16}}\right)^{1/4} [1 - 1.2N_D^{-1/3}] W \left(\frac{N_e}{10^{16}}\right) \tag{2.14}$$

The first term above is the contribution from electron broadening and the second term is the ion broadening correction. W is the electron impact parameter which can be interpolated at different temperatures [18] and A is the ion broadening parameter. Here both W and A are weak functions of temperature. N_e is the electron density in cm^{-3} and N_D is the number of particles in the Debye sphere. Since the contribution from ion broadening is much smaller than the electronic contribution, the second term can be ignored.

The theoretical Stark broadening profiles numerically calculated for hydrogen lines are usually presented as one half of the symmetrical profile $S(\alpha)$ where α is a reduced wavelength distance, given by [14]

$$\alpha \equiv \frac{\Delta\lambda}{F_0} \tag{2.15}$$

here $\Delta\lambda$ denotes the distance from the line center in Å, and the F_0 is the Holtzmark field strength, given by

$$F_0 = 1.25 \times 10^{-9} N_e^{2/3} \tag{2.16}$$

The FWHM for hydrogen lines is [14]

$$\Delta\lambda_S = 2.50 \times 10^{-13} \alpha_{1/2} N_e^{2/3} \tag{2.17}$$

where N_e is in m^{-3}. The theoretical half-width $\alpha_{1/2}$ is the value of α at which $S(\alpha)$ is half of its maximum value. Equation (2.17) can also be used for the He II line which is studied in this thesis. The values of $\alpha_{1/2}$ for the ionized Helium lines for $n = 4$ to $n = 3$ transition are found in [24]. In Table 2.1, the temperature T is in 10^3 K, and electron density N_e is in m^{-3}. For example, the width of the Stark broadening for the He II line at 4686 Å ($n = 4 \rightarrow 3$) at $T = 10^4$ K and $N_e = 10^{20}\,\mathrm{m}^{-3}$ is $\Delta\lambda_S = 0.013$ Å.

2.4 Fine structure splitting

For the hydrogen atom and hydrogen-like ions with small nuclear charge Z, the fine structure can be calculated. The fine structure splitting (or *multiplet splitting*) is the sum of the energy due to relativistic effects. The relativistic effects are the velocity dependence of electron mass and the spin-orbit interaction. Here the energy due to the velocity dependence of electron mass is given by [31]

$$\Delta E'_{nl} = -\alpha^2 \left(\frac{1}{l + 1/2} - \frac{3}{4n} \right) \frac{Z^4}{n^3} R_\infty \tag{2.18}$$

and the energy due to the spin-orbit interaction is given by

$$\Delta E''_{nlj} = \alpha^2 \frac{j(j+1) - l(l+1) - s(s+1)}{2l(l+1)(l+1/2)} \frac{Z^4}{n^3} R_\infty. \tag{2.19}$$

Table 2.1: The half-width parameter $\alpha_{1/2}$ for the He II lines of $n = 4 \rightarrow 3$

	$N_e = 10^{20}$	10^{21}	10^{22}	10^{23}	10^{24}
$T = 5$	$2.84 \cdot 10^{-3}$	$4.92 \cdot 10^{-3}$	-	-	-
10	$2.48 \cdot 10^{-3}$	$4.46 \cdot 10^{-3}$	$6.78 \cdot 10^{-3}$	$9.80 \cdot 10^{-3}$	$1.24 \cdot 10^{-2}$
20	-	$4.11 \cdot 10^{-3}$	$6.39 \cdot 10^{-3}$	$9.21 \cdot 10^{-3}$	$1.22 \cdot 10^{-2}$
40	-	$3.21 \cdot 10^{-3}$	$5.81 \cdot 10^{-3}$	$8.90 \cdot 10^{-3}$	$1.26 \cdot 10^{-2}$
80	-	-	$5.18 \cdot 10^{-3}$	$8.37 \cdot 10^{-3}$	$1.24 \cdot 10^{-2}$
160	-	-	-	$7.99 \cdot 10^{-3}$	$1.24 \cdot 10^{-2}$

The fine structure splitting is then obtained by

$$\Delta E_{nlj} = \Delta E'_{nl} + \Delta E''_{nlj} = \alpha^2 \left(\frac{3}{4n} - \frac{1}{j+1/2} \right) \frac{Z^4}{n^3} R_\infty. \tag{2.20}$$

Here

$$\alpha = \frac{\mu_0 c e^2}{2h} = 7.297 \times 10^{-3} \tag{2.21}$$

is the fine structure constant, and

$$R_\infty = \frac{m_e c \alpha^2}{2h} = 1.097 \times 10^7 m^{-1} = 13.6\,\text{eV} \tag{2.22}$$

is the Rydberg constant. From Equation (2.20), it follows that fine structure splitting decreases with an increase of n approximately as $1/n^3$, therefore this splitting is important for lower levels. When $l \neq 0$ the energy between levels $j = l + 1/2$ and $j = l - 1/2$ is simply

$$\Delta E_{FS} = \frac{\alpha^2 Z^4 R_\infty}{n^3 l(l+1)}. \tag{2.23}$$

For example, for the He II ion the splitting of level $n = 4$ for $l = 1, 2, 3$ is $9.052 \times 10^{-5}\,\text{eV}$, $3.017 \times 10^{-5}\,\text{eV}$, and $1.509 \times 10^{-5}\,\text{eV}$, respectively. This field free fine structure ($nlj \rightarrow nlj'$ transition) concept will be used for the comparison between the anomalous Zeeman and Paschen-back effect in the following sections. The transition $nlj \rightarrow n'l'j'$ is called a multiplet, in which the selection rule with respect to the quantum number j is $\Delta j = 0, \pm 1$.

2.5 Zeeman Splitting

Spectral line broadening can also result from magnetic fields by way of Zeeman splitting. This splitting of the energy term of atoms in a magnetic field can be observed as a splitting of the frequencies of transitions in the optical spectra. The energy splitting depends on the magnetic field strength while the effective broadening also depends on the observation direction to the magnetic field.
The Zeeman effect that occurs for spectral lines resulting from a Zeeman transition between singlet states is traditionally called the Normal Zeeman effect, while that which occurs when the total spin of either the initial or final states, or both, is nonzero is called the Anomalous Zeeman effect for the case of a weak magnetic field. When the magnetic field is sufficiently strong the Anomalous Zeeman effect is called the Paschen-Back effect.

2.5.1 Normal Zeeman effect

For singlet states, the total spin is zero and the total angular momentum **J** is equal to the orbit angular momentum **L**. The energy of interaction of an atom with a uniform external magnetic field of flux density **B** is

$$\Delta E = -\mu \cdot \mathbf{B} = -\mu_z B \tag{2.24}$$

where the z direction is defined by the direction of **B**. Since $\mu_z = -m_l \mu_B$, $\mu_B = -M_l(e\hbar/2m_e)$, we get

$$\Delta E = m_l \frac{e\hbar}{2m_e} B = m_l \mu_B B \tag{2.25}$$

where μ_B is the Bohr magnetron. Each energy level splits into $2l + 1$ levels since there are $2l + 1$ values of m_l.

2.5.2 Anomalous Zeeman effect (Weak magnetic fields)

The anomalous Zeeman effect occurs when the spin of either the initial or the final states, or both, is nonzero. The calculation of the energy-level splitting is complicated by the fact that the magnetic moment due to spin is 1 rather than $\frac{1}{2}$ Bohr magnetron, and as a result the total magnetic moment is not parallel to the total angular momentum. The total angular momentum is

$$\mathbf{J} = (\mathbf{L} + \mathbf{S}) \tag{2.26}$$

where **L** and **S** are the orbital angular momentum and spin, respectively. Whereas the total magnetic moment is

$$\mu = -\frac{\mu_B}{\hbar}(\mathbf{L} + \mathbf{S}). \tag{2.27}$$

Each energy level is split into $2j + 1$ levels, corresponding to the possible values of m_j. For the usual laboratory magnetic fields, which are weak compared with the internal magnetic field associated with the spin-orbit effect, the level splitting is small compared with the fine-structure splitting. Unlike the case of the singlet levels in the Normal effect, the Zeeman splitting of these levels depends on j, l, and s, and in general there are more than three different transition energies due to the fact that the upper and lower states are split by different amounts. The level splitting is the energy shift relative to the position of the no-field energy level, and can be written as [25]

$$\Delta E = g m_j \left(\frac{e\hbar B}{2m_e} \right) = g m_j \mu_B B \tag{2.28}$$

Table 2.2: Relative intensities of Zeeman components

Transverse observation

Transition	I_π	$I_\sigma(m_j \to m_j - 1)$	$I_\sigma(m_j \to m_j + 1)$
$J \to J$	m_j^2	$\frac{1}{4}(J+m_j)(J+1-m_j)$	$\frac{1}{4}(J-m_j)(J+1+m_j)$
$J \to (J\text{-}1)$	$J^2\text{-}m_j^2$	$\frac{1}{4}(J+m_j)(J-1+m_j)$	$\frac{1}{4}(J-m_j)(J-1-m_j)$
$J \to (J+1)$	$(J+1)^2\text{-}m_j^2$	$\frac{1}{4}(J+1-m_j)(J-m_j+2)$	$\frac{1}{4}(J+1+m_j)(J+m_j+2)$

Longitudinal observation

Transition	I_π	$I_\sigma(m_j \to m_j - 1)$	$I_\sigma(m_j \to m_j + 1)$
$J \to J$	0	$\frac{1}{2}(J+m_j)(J+1-m_j)$	$\frac{1}{2}(J-m_j)(J+1+m_j)$
$J \to (J\text{-}1)$	0	$\frac{1}{2}(J+m_j)(J-1+m_j)$	$\frac{1}{2}(J-m_j)(J-1-m_j)$
$J \to (J+1)$	0	$\frac{1}{2}(J+1-m_j)(J-m_j+2)$	$\frac{1}{2}(J+1+m_j)(J+m_j+2)$

where the Landé factor g is given by

$$g = 1 + \frac{j(j+1) + s(s+1) - l(l+1)}{2j(j+1)}. \tag{2.29}$$

In many-electron atoms, the quantum numbers s, l, and j are replaced by S, L, and J. The Anomalous Zeeman effect is of special interest because of the importance of the Zeeman data in the analysis and theoretical interpretation of complex spectra. The rules for the relative intensities of Zeeman components are tabulated in Table 2.2 [31]. In the transverse direction the intensity of the σ components is less than along z axis by a factor of two. For example, Figure 2.1 shows an Anomalous Zeeman effect of the $4d^2D_{5/2} \to 3p^2P_{3/2}$ He II line at $B = 0.1\,\mathrm{T}$, where the Zeeman splitting $\Delta\lambda_Z$ is $0.029\,\text{Å}$, and the selection rule is $\Delta m_j = 0, \pm 1$. The relative intensities (transverse observation) of the π and σ components of the line are also shown in this figure where σ components are in the negative direction by convention. The detailed calculation of the line splitting is summarized in Appendix A, and the transition with a strong magnetic field will be discussed in the next section as an example of the Paschen-Back effect.

2.5.3 Paschen-Back effect (Strong magnetic fields)

In the previous section, the Zeeman splitting was considered for weak magnetic fields, where *weak* means that the splitting of energy levels in the magnetic field is small compared to the fine structure splitting. In other words, the coupling between the orbital and spin moments (the spin-orbit coupling) is stronger than the coupling of either the spin or the orbital moment alone to the external magnetic field. Since spin-orbit coupling increases rapidly with increasing nuclear charge Z, the conditions for a *strong* field are met at a much lower field with light atoms than with heavy atoms [17].

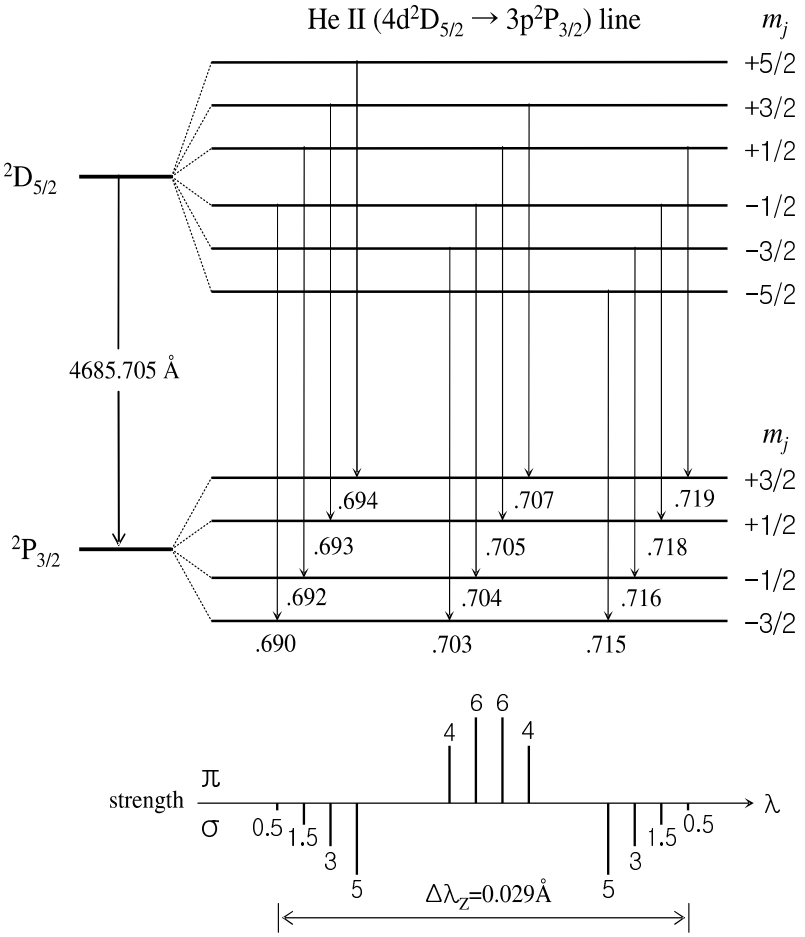

Figure 2.1: Anomalous Zeeman effect of the $4d^2D_{5/2} \rightarrow 3p^2P_{3/2}$ He II line at $B = 0.1$ T. The transition splits into 12 components in a weak magnetic field.

If the magnetic field B is strong enough so that the fine structure splitting can be neglected, the Zeeman splitting is given by [25]

$$\Delta E = (m_l + 2m_s)\left(\frac{e\hbar B}{2m_e}\right) = (m_l + 2m_s)\mu_B B. \tag{2.30}$$

The transitions have to satisfy the selection rules

$$\Delta m_s = 0 \tag{2.31}$$

and

$$\Delta m_l = 0, \pm 1 \tag{2.32}$$

where Δm_l depends on the polarization of the light [26].
The splitting is then similar to the Normal Zeeman effect and only three lines are observed. This behavior in a strong magnetic field is called the Paschen-Back effect after its discoverers, F. Paschen and E. Back. For example, Figure 2.2 shows a comparison of the weak magnetic field Anomalous Zeeman effect and the strong magnetic field Paschen-Back effect for the $4d^2D_{5/2} \rightarrow 3p^2P_{3/2}$ He II line at $B = 0.1$ T

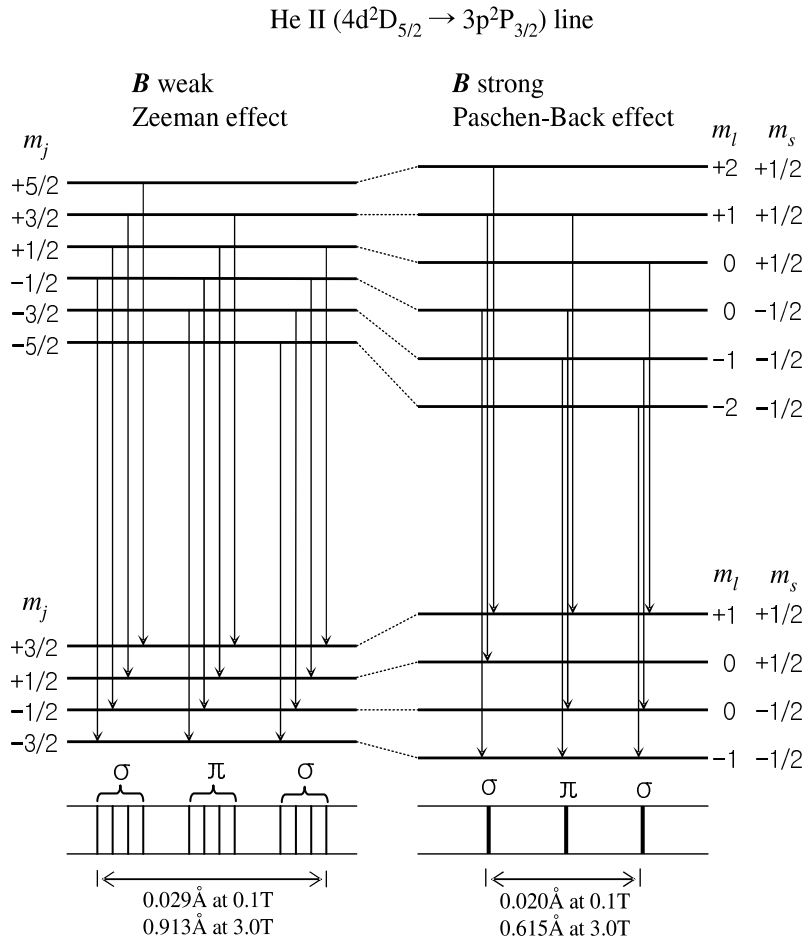

Figure 2.2: Comparison of the weak magnetic field Anomalous Zeeman effect and strong magnetic field Paschen-Back effect for the $4d^2D_{5/2} \rightarrow 3p^2P_{3/2}$ He II line at $B = 0.1\,\mathrm{T}$ and $3.0\,\mathrm{T}$. In the strong magnetic field the transition splits into 3 components.

and 3.0 T.

2.6 Instrument broadening

In this section we consider broadening caused by the instrument itself. Observed spectral line profiles are the result of several simultaneously acting line broadening mechanisms as discussed in the previous sections. In most cases the instrument broadening or instrument function may be an essential problem of the spectral line broadening because the instrument is not ideal. Accordingly, the instrument function is of special interest because it is important to observe a physical phenomenon accurately. It must be considered and corrected for in all instruments. For example, the instrument function of a grating spectrometer is formed by the image of the entrance slit on the detector. If the entrance slit is uniformly filled with monochromatic light, the image plane will show the superposition of a large number of diffraction patterns. This slit function can be estimated by a deconvolution process (See Chapter 2 of [22]). In the MOSS spectrometer the instrument phase and

contrast cause the instrument broadening, which is similar to the finite resolution of the grating spectrometer. It will be discussed in Section 4.6.

2.7 Spectral line profiles

In general, line profiles are the result of several line broadening mechanisms. As shown in the previous sections in this chapter, pressure broadening and natural line broadening give spectral profiles that are Lorentzian.

$$L(\omega - \omega_0, \Gamma) = \frac{\Gamma}{2\pi} \frac{1}{(\omega - \omega_0)^2 + (\Gamma/2)^2} \tag{2.33}$$

where Γ is the full width of the distribution at half the density. The spectral profile of the radiation emitted by the moving atoms is found by averaging the equation (2.33) over the thermal distribution of the Doppler shifted atoms, and is given by

$$G(\omega - \omega_0, \sigma) = \frac{1}{\sqrt{2\pi}\sigma} \exp\left[-\frac{1}{2}\left(\frac{\omega - \omega_0}{\sigma}\right)^2\right]. \tag{2.34}$$

In most cases the line shape is either Lorentzian (2.33) or Gaussian (2.34). Both distributions attain their maximum at $\omega = \omega_0$. The Lorentzian line shape attains a maximum of $L(0) = 2/\pi\Gamma$, while for a Gaussian distribution $G(0) = 1/\sqrt{2\pi\sigma}$. Γ and σ determine the width of the distributions. $\Gamma/2$ is the half-width of the spectral line at half of its peak value, $L(\omega) = \frac{1}{2}L(0)$ for $\omega - \omega_0 = \pm\Gamma/2$. In a similar manner, in a Gaussian distribution, $G(\omega)$ decreases to about 0.606 of its maximum value when $\omega - \omega_0 = \pm\sigma$, and the intensity of the line reduces to one-half of its value at the line center when $\omega - \omega_0 = \pm\sigma\sqrt{2\log 2} = \pm 1.177\sigma$. Generally, both $\Gamma \ll \omega_0$ and $\sigma \ll \omega_0$, so that the line profile is a function which takes nonzero values only in a very narrow part of the spectrum [16].
Combining the functions (2.33) and (2.34) gives [23]

$$\begin{aligned} V(\omega - \omega_0, \Gamma/\sigma) &= L \otimes G \\ &= \int_{-\infty}^{\infty} L(\omega - \omega_0, \Gamma) \cdot G(\omega - \omega_0, \sigma) d\omega_0 \end{aligned} \tag{2.35}$$

This profile is known as the Voigt line profile. Figure 2.3 shows a comparison between Lorentz, Gauss, and Voigt line profiles. The shape of the Voigt profile is determined by the ratio of Γ/σ. In this thesis it will be assumed that the spectral line profile is approximately Gaussian since the Stark broadening which is approximately Lorentzian is small compared to the Doppler broadening in the experimental condition. (see Section 3.3).

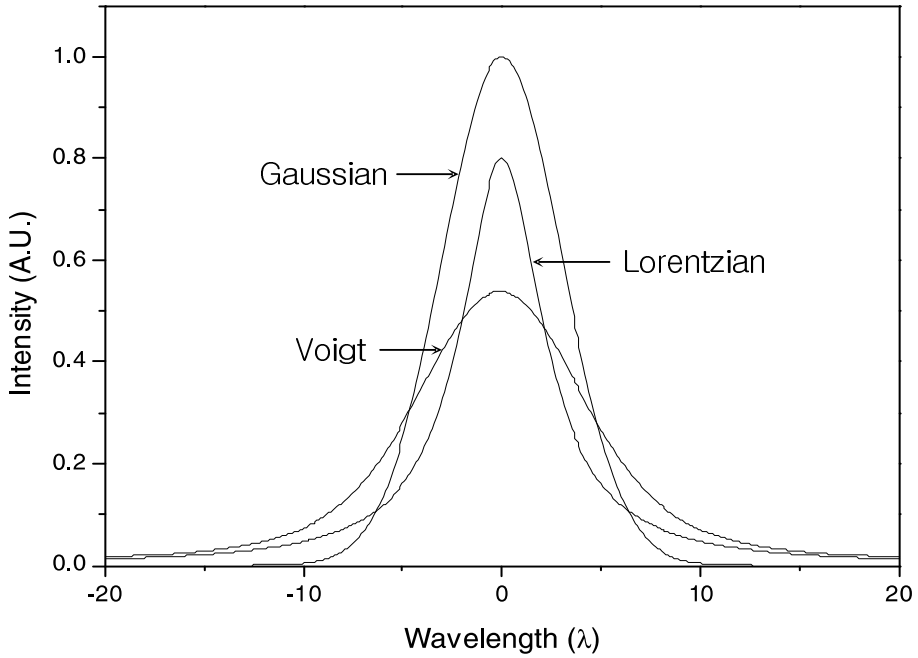

Figure 2.3: Comparison between Lorentz, Gauss, and Voigt line profiles.

3

Coherence simulations for the MOSS spectrometer construction

The MOSS spectrometer is based on the principle of the Fourier-transform spectrometer about a fixed delay. The isolated line to be used must be determined before constructing the MOSS spectrometer. It is not only important for the construction of the MOSS spectrometer, but also very important to understand the measured signal correctly. To accomplish this, a MOSS simulation code and suitable models were created. The simulation code provides an effective way to select suitable optical components such as filters and crystals. In this chapter, the physical background of the simulation, simulation models and physical assumptions, and some important simulation results are discussed. The reason to discuss the simulation before discussing the theory of the MOSS spectrometer is that the simulation is closely related to atomic physics and the basic concept of coherence theory. It is also very helpful to understand what the MOSS spectrometer measures. The theory of the MOSS spectrometer will be discussed in the following chapter.

3.1 Line width and coherence

Assume the lifetime of the excited state is *infinite*, and an atomic oscillator emitting a continuous radiation of amplitude $F(t)$ such that

$$F(t) = F_0 \exp(i\omega_0 t). \tag{3.1}$$

The Fourier transform of this amplitude is given by

$$\tilde{F}(\omega) = \frac{1}{\sqrt{2\pi}} \int_{-\infty}^{+\infty} F(t) \exp(-i\omega t) dt = F_0 \cdot \delta(\omega - \omega_0). \tag{3.2}$$

In this case, the oscillation and the emitted photons have only one sharply defined frequency, ω_0, and its line profile is a Dirac delta function,

$$D(\omega) = \delta(\omega - \omega_0). \tag{3.3}$$

Figure 3.1 illustrates the Fourier transform relation between the continuous radiation amplitude and its line shape.

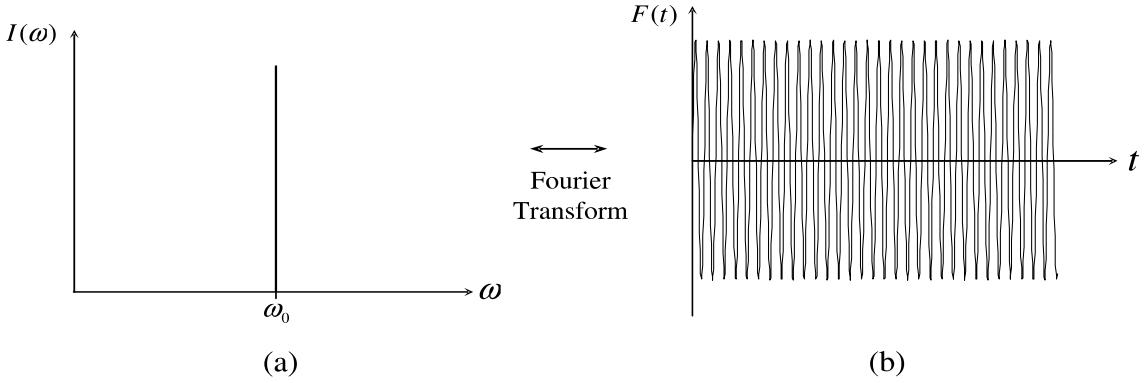

Figure 3.1: Fourier transform relation between (b) the continuous radiation amplitude and (a) its line shape. The line shape is a Dirac delta function.

But in reality the lifetime of the excited state is always *finite*. This is also the reason why the natural line shape is Lorentzian as discussed in the previous chapter. In analogy to Equation (2.1), the amplitude of the emitted light decreases exponentially. The radiation field amplitude F has the form in complex notation

$$F(t) = F_0 \left(e^{i\omega_0 t} e^{-\Gamma t/2} \right) \tag{3.4}$$

where $t > 0$ since the excitation occurs at $t = 0$, and there is no light when $t < 0$.

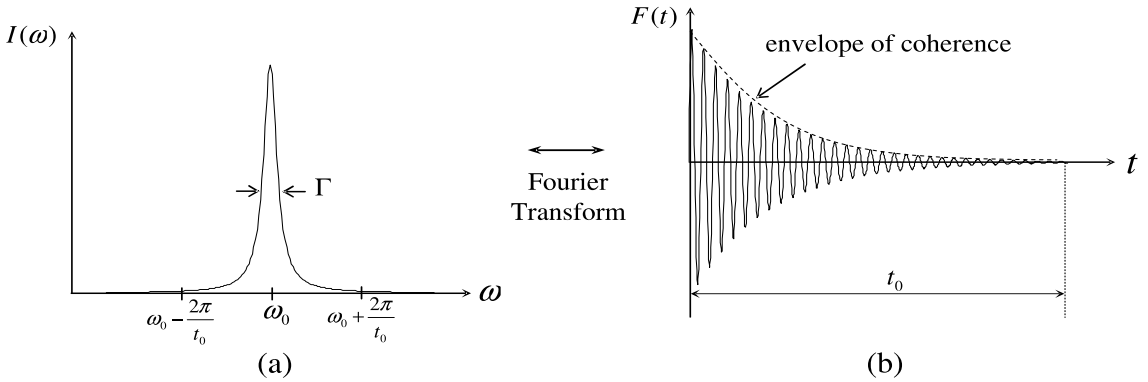

Figure 3.2: Fourier transform relation between (b) the exponential decay of the radiation field amplitude F and (a) its Lorentzian line shape.

Figure 3.2 shows the decreasing form of the radiation field amplitude F and its line shape. The line has a Lorentzian line width, Γ. It also tells that the Fourier transformed amplitude of an emission line profile decreases exponentially if the line profile has a finite line width. Here the spectral distribution is maximum for $\omega = \omega_0$ and drops to zero for $\omega = \omega_0 \pm 2\pi/t_0$, where t_0 is the decay time of the emission amplitude. Now if we consider the sequence of the atomic transition, the average

time $\langle t_0 \rangle$ is called the *coherence time* of the radiation and is given by

$$\langle t_0 \rangle = \frac{1}{\Delta\nu}. \tag{3.5}$$

A *coherence length* in terms of wavelength can also be defined as

$$l_c = \frac{c}{\Delta\nu} = \frac{\lambda^2}{\Delta\lambda} \tag{3.6}$$

where $\Delta\nu$ and $\Delta\lambda$ are the widths of the spectrum line on the frequency and wavelength scales respectively. For example, the coherence length and time for the He II line at 4686 Å having a line width of 1 Å, from Equations (3.5) and (3.6), is about 7.3×10^{-12} s and 2.2 mm, respectively.
In many cases Doppler broadening is the dominant broadening mechanism and is proportional to the plasma temperature for the emission line as discussed in the previous chapter. Consequently, when the emission line is broadened, which means the plasma temperature for the emission line is increased, its Fourier transformed envelope of amplitude decreases rapidly in time delay. This is actually what the MOSS spectrometer measures in a fixed delay.

3.2 Creating a simulation model

The MOSS spectrometer measures the coherence of the emission line about a fixed delay, which means that if there are two or more emission lines existing in the optical region where the MOSS spectrometer is looking, the coherence or fringe visibility in time delay must be complicated. Figure 3.3 shows that two individual lines make a

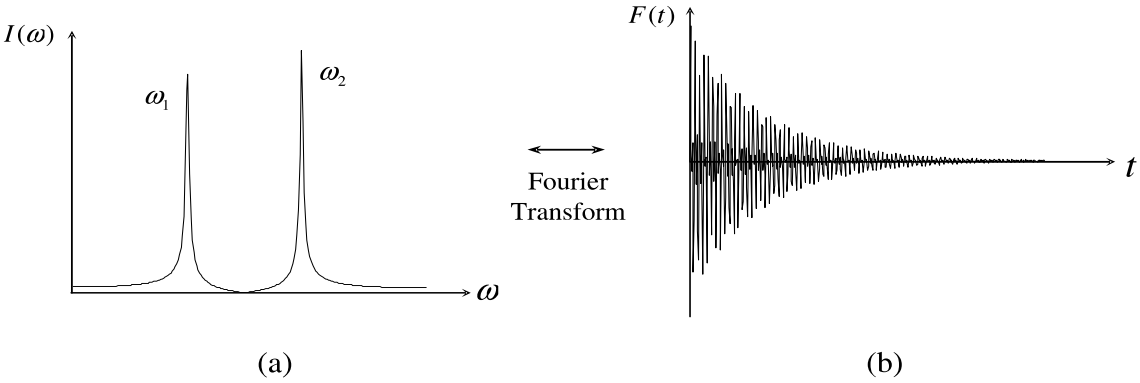

Figure 3.3: (a) Two individual lines, frequencies of ω_1 and ω_2 (b) make a more complicated fringe visibility.

more complicated amplitude variation in time. In order to avoid such a complicated situation and to select an isolated line, a narrow-band optical filter needs to be used. However, an optical filter alone is still not enough to isolate only one individual line since even if a filtered line looks like an isolated line, it probably consists of multiplets

or many individual lines which cannot be resolved with usual grating spectrometers in hot temperature plasmas. The aim of the MOSS coherence simulation is to draw the envelope of coherence (see Figure 3.2) of the numerically resolved and filtered line under different plasma conditions such as plasma temperature, density, and external magnetic field strength.
The procedure for creating a simulation model is as follows : (1) Get a spectrum from the target plasma with a grating spectrometer in the optical region. (2) Select candidate lines from the spectrum. (3) Resolve the candidate lines if they are not singlets. The relative line intensities must be considered. (4) Estimate all of the possible broadening mechanisms in the experimental conditions. (5) Create the line models with the numerically resolved individual lines and the estimated broadening effects. (6) Create a filter model. It must be possible to order from the market. (7) Create and execute the MOSS coherence simulation code with the simulation models in various plasma conditions. The code generates the Fourier transform of the simulation model, and draws the envelope of coherence in the desired ion temperature range. These procedures are discussed in the following sections in more detail.

3.2.1 Candidate lines for investigations of divertor plasmas

First of all, to create the simulation model, it is necessary to first investigate the spectrum of the target plasma using a grating spectrometer in the visible spectral region in which the MOSS spectrometer works. The spectrum in Figure 3.4 shows two possible candidate lines from the W7-AS[1] divertor.
Since the two lines in the spectrum are separated by around 37 Å there will be no problem to observe each one of them separately using a 10 Å band width interference filter. The two strong lines in this spectral region, the C III line at 4649 Å and the He II line at 4686 Å, consist of 3 multiplet lines and 13 individual lines respectively. Figure 3.5 is an abridged version of the He II Grotrian Diagram for $n = 4 \rightarrow 3$ transition. The diagram illustrates many transitions near 4686 Å, which cannot be resolved with grating spectrometers. This is why the simulation is important for the MOSS spectrometer construction and for understanding its experimental results.

3.2.2 The relative line intensities of the candidate lines

To create a reliable simulation model, the relative line intensities of the C III multiplet and the He II individual lines should be calculated. The total power ε radiated in a spectral line of frequency ν per unit source volume and per unit solid angle is

$$\varepsilon_{line} = (4\pi)^{-1} h\nu A_{ki} N_k \tag{3.7}$$

[1]See Section 5.1

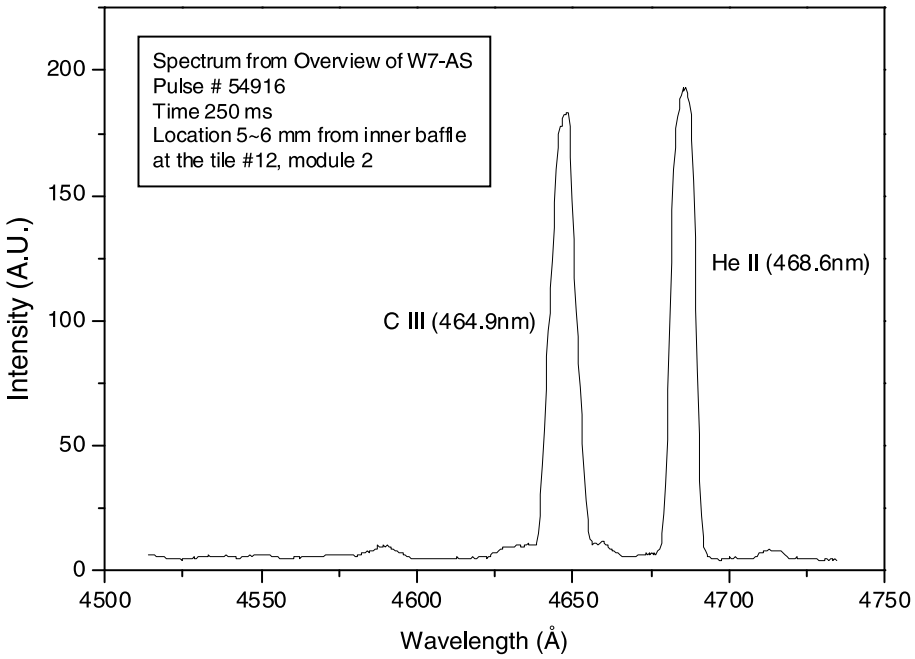

Figure 3.4: Spectrum of two candidate lines, C III at 464.9 nm and He II at 468.6 nm, from the W7-AS divertor target plasma measured with a low resolution spectrometer.

where A_{ki} is the atomic transition probability and N_k is the number per unit source volume (number density) of excited atoms in the upper (initial) level k. For a homogeneous optically thin plasma of length l the total emitted line intensity (radiance) is given by :

$$I_{line} = \varepsilon_{line} l = \int_0^{+\infty} I(\lambda) d\lambda = (4\pi)^{-1} \left(\frac{hc}{\lambda_0}\right) A_{ki} N_k l \tag{3.8}$$

where $I(\lambda)$ is the specific intensity at wavelength λ, and λ_0 is the wavelength at the line center [20]. The relative line intensity between two lines is given by

$$\frac{I}{I'} = \frac{A_{ki} N_k \lambda_0'}{A_{ki}' N_k' \lambda_0} \tag{3.9}$$

and if the levels are populated according to their statistical weights, then the relative line intensity is

$$\frac{I}{I'} = \frac{A_{ki} g_k \lambda_0'}{A_{ki}' g_k' \lambda_0} \tag{3.10}$$

where g_k is the statistical weight of the upper level k, and is given by

$$g = 2J + 1 \tag{3.11}$$

where J is the total angular momentum of the atom. Note that the Equation (3.10) is valid when a criteria

$$8.5 \times 10^{-16} \frac{n^{8.5}}{Z^{7.5}} N_e \geq 1 \tag{3.12}$$

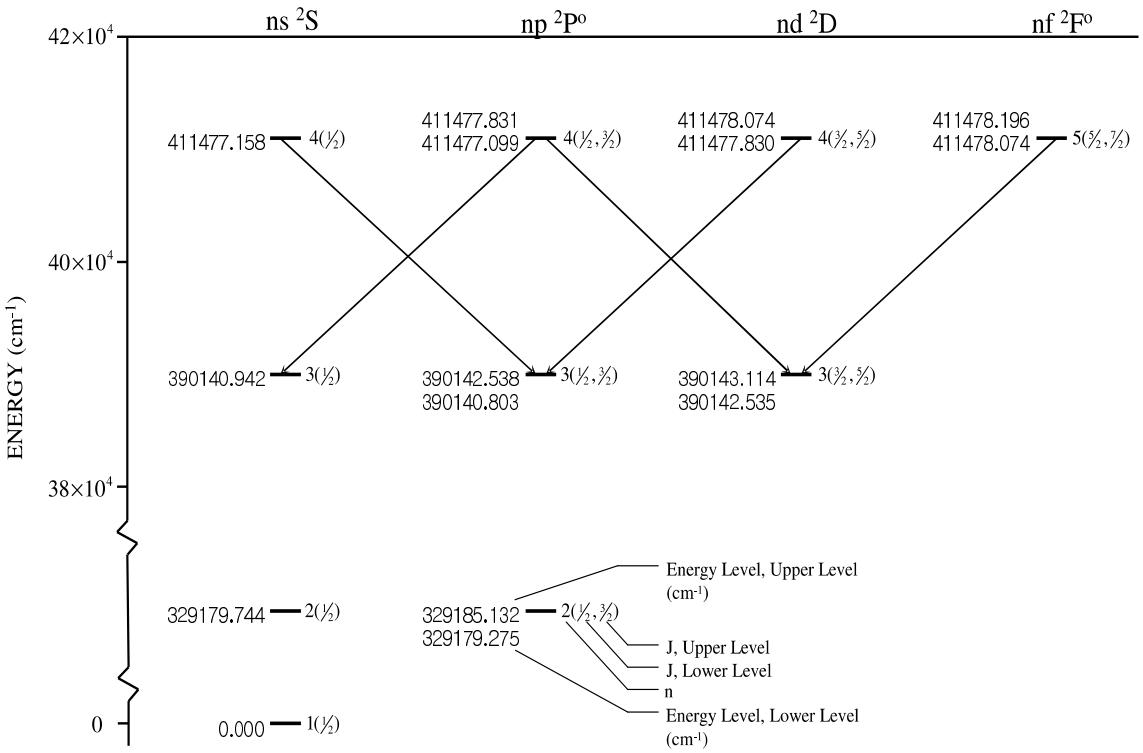

Figure 3.5: He II Grotrian Diagram near 468.6 nm. (This diagram has been abridged for the $n = 4 \rightarrow 3$ transition from the original He II Grotrian Diagram.)

is satisfied [27], where N_e is electron density in cm^{-3}. Our experimental conditions always satisfied the criteria for $n = 4$ and $Z = 1$. The He II lines cannot be resolved into the individual multiplet lines (J-levels) since the levels are too closely spaced. In this case it is sufficient to treat only the individual l-levels. Also, the statistical weights of the whole multiplets must be used. They can be calculated from

$$g(multiplet) = (2L + 1)(2S + 1) \tag{3.13}$$

where L is the total orbital angular momentum of the electrons and S is the total spin.

The relative line intensities of the C III multiplet and the He II individual lines were calculated and tabulated in Tables 3.1 and 3.2, respectively. All $n - n' = 4 - 3$ transitions were calculated in the Coulomb approximation using a code developed by J. Hey [28] while all the other required variables were taken from the NSRDS Atomic Transition Probabilities table book [29] and in the Grotrian Diagram [30].

3.2.3 Field free Simulation model

A simulation model was created for the C III and He II line and was discussed in the previous section. The relative line intensity values were applied to the model. Figure 3.6 shows the simulation model, which corresponds to the zero-temperature

Table 3.1: Relative intensities of C III multiplet lines at 464.9 nm.

♯	Transition	λ_{air}(Å)	$A_{ki}(10^8 s^{-1})$	g_k	g_i	I_{rel}
1	$3p^3P_2 \rightarrow 3s^3S_1$	4646.10	0.78	5	3	1.0000
2	$3p^3P_1 \rightarrow 3s^3S_1$	4648.86	0.78	3	3	0.5996
3	$3p^3P_0 \rightarrow 3s^3S_1$	4650.05	0.78	1	3	0.1998

Table 3.2: Relative intensities of He II multiplet lines at 468.6 nm.

♯	Transition	λ_{air}(Å)	$A_{ki}(10^8 s^{-1})$	g_k	g_i	I_{rel}
1	$4s^2S_{1/2} \rightarrow 3p^2P_{1/2}$	4685.53	0.0978	2	6	0.0063
2	$4s^2S_{1/2} \rightarrow 3p^2P_{3/2}$	4685.91	0.1958	2	6	0.0127
3	$4p^2P_{1/2} \rightarrow 3s^2S_{1/2}$	4685.57	0.4905	6	2	0.0953
4	$4p^2P_{1/2} \rightarrow 3d^2D_{3/2}$	4685.92	0.0556	6	10	0.0108
5	$4p^2P_{3/2} \rightarrow 3s^2S_{1/2}$	4685.41	0.4903	6	2	0.0953
6	$4p^2P_{3/2} \rightarrow 3d^2D_{3/2}$	4685.76	0.0055	6	10	0.0011
7	$4p^2P_{3/2} \rightarrow 3d^2D_{5/2}$	4685.89	0.0500	6	10	0.0097
8	$4d^2D_{3/2} \rightarrow 3p^2P_{1/2}$	4685.38	0.9384	10	6	0.3039
9	$4d^2D_{3/2} \rightarrow 3p^2P_{3/2}$	4685.76	0.1877	10	6	0.0608
10	$4d^2D_{5/2} \rightarrow 3p^2P_{3/2}$	4685.71	1.1260	10	6	0.3646
11	$4f^2F_{5/2} \rightarrow 3d^2D_{3/2}$	4685.71	2.0590	14	10	0.9334
12	$4f^2F_{5/2} \rightarrow 3d^2D_{5/2}$	4685.83	0.1471	14	10	0.0667
13	$4f^2F_{7/2} \rightarrow 3d^2D_{5/2}$	4685.81	2.2059	14	10	1.0000

situation. The He II line at 468.6 nm consists of 13 individual lines within a narrow interval of 0.05 nm which cannot be resolved, and the C III triplet at 464.9 nm is widely separated (0.4 nm) compared with the He II lines. The model assumes that the Doppler broadening is dominant so that the line shape of each individual line is a Gaussian. This assumption is reasonable in many cases, but one more model will be introduced after discussing the other possible major broadening mechanisms in the following sections. The filter transmission curve is approximated by a Lorentzian function (FWHM=10 Å) model and covers all lines.

3.3 Line broadening mechanisms

In the previous chapter, most of the known broadening mechanisms for plasmas were classified with some examples for the He II line. In this section, the broadening mechanisms are summarized briefly, and the three important broadening mechanisms, Doppler broadening, Stark broadening, and Zeeman splitting, are compared in detail so that the experimental conditions can be simulated properly in the simulation model.

First of all, natural broadening is the simplest mechanism because the finite lifetime

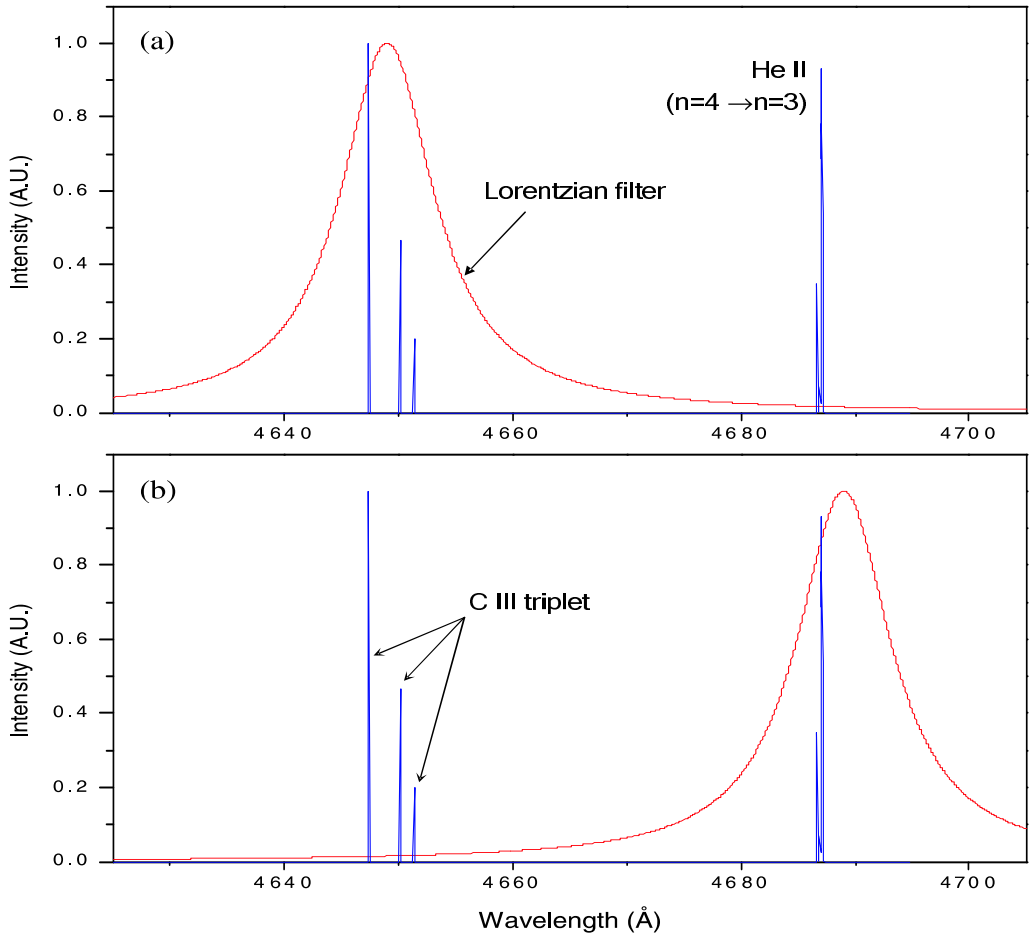

Figure 3.6: Simulation models of the candidate lines, (a) C III filtered and (b) He II filtered case. The filter profile is a Lorentzian with FWHM of 10 Å.

of ionic excited states amounts to about 10^{-4} Å. This is much less than other broadening mechanisms and is therefore negligible. Secondly, pressure broadening, which is due to the interaction of the radiating atom with surrounding particles, can be sub-divided into resonance broadening, Van der Waals broadening, and Stark broadening. Resonance broadening and Van der Waals broadening can be ignored since our candidate lines are not related to the ground states, hence only Stark broadening will be considered. Thirdly, Zeeman splitting, which results from external magnetic fields, will be considered since a plasma is confined by external magnetic fields. Finally, Doppler broadening, which is due to the thermal velocity distribution of the emitting ions, is used as a yardstick for Stark broadening and Zeeman splitting since it is a principal mechanism.

3.3.1 Stark broadening versus Doppler width

To compare Stark and Doppler broadening, recall their simplified equations, (2.10) and (2.17), from the previous chapter. Doppler broadening was given by

$$\Delta\lambda_D = 7.716 \times 10^{-5}\lambda_0 \left(\frac{T_{eV}}{A_{rel}}\right)^{1/2} \tag{3.14}$$

and Stark broadening was given by

$$\Delta\lambda_S = 2.50 \times 10^{-13}\alpha_{1/2}N_e^{2/3} \tag{3.15}$$

As shown in Equation (3.14) Doppler broadening is proportional to temperature and is not related to any density parameters. Stark broadening, on the other hand, is proportional to the electron density, and the theoretical half-width $\alpha_{1/2}$. The latter is proportional to the Stark width and is inversely proportional to the temperature as shown in the Table 2.1.

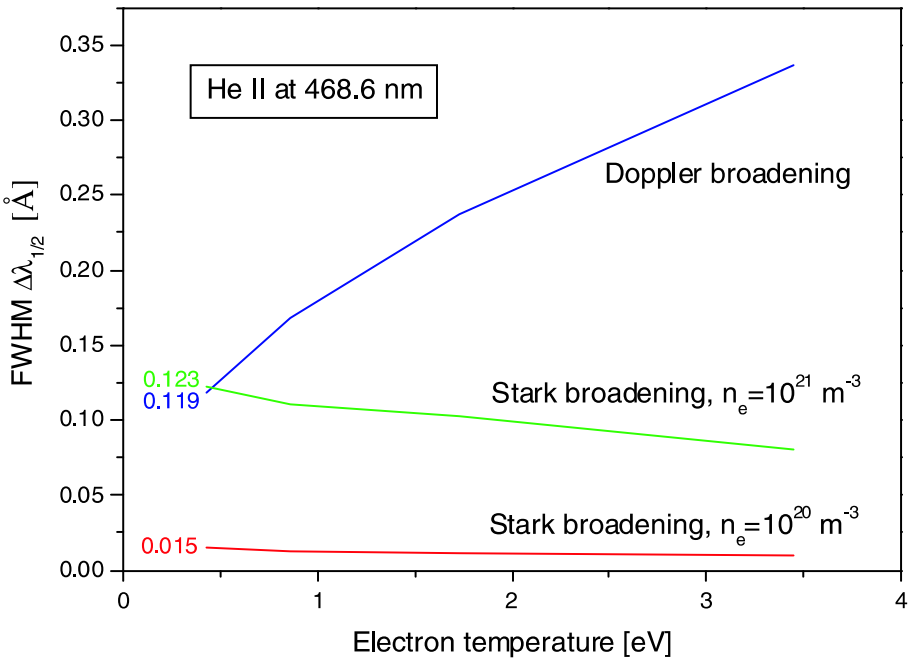

Figure 3.7: Comparison of the Doppler and Stark broadenings for the He II at 468.6 nm

The simulation code assumes the Doppler broadening to be dominant over the Stark broadening for the He II line at 468.6 nm. As shown in Figure 3.7, at 1 eV, the Doppler broadening is already over 10 times higher than the Stark broadening for an electron density of $10^{20}\,\mathrm{m}^{-3}$. As the temperature increased, the Doppler broadening is even higher compared to the Stark broadening which slightly decreases with increasing temperature. Figure 3.8 shows the Doppler broadening in the temperature range of $1 - 100$ eV. The dashed line in the figure is the Stark broadening at $T = 4$ eV and $n_e = 10^{21}\,\mathrm{m}^{-3}$.

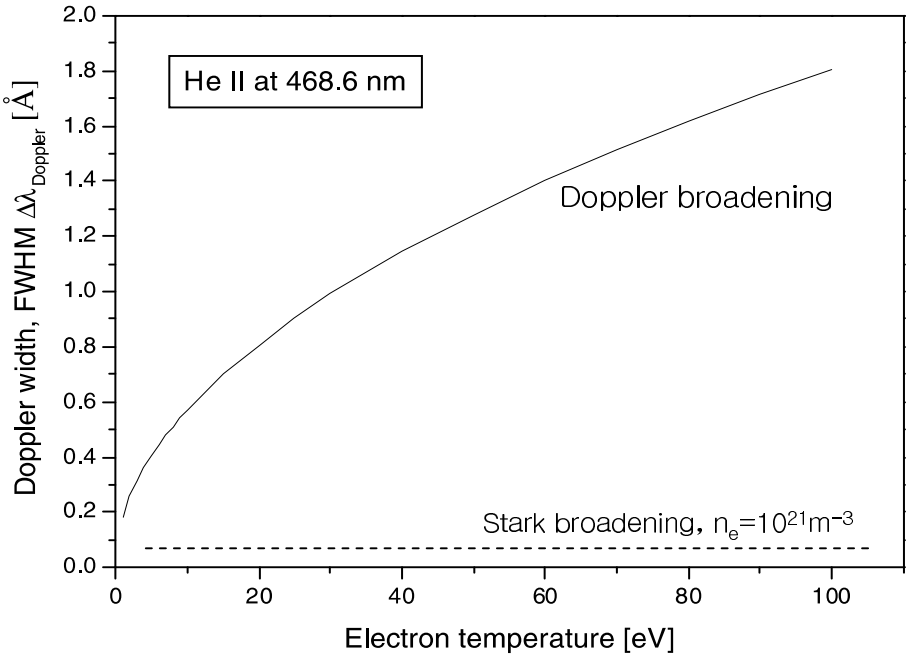

Figure 3.8: Doppler broadening for the He II at 468.6 nm in the temperature range of $1 - 100\,\mathrm{eV}$.

Consequently, the Stark broadening can be neglected for the He II line when

$$T < 1\,\mathrm{eV} \quad , \quad n_e < 10^{19}\,\mathrm{m}^{-3} \quad \Rightarrow \quad \text{WEGA stellarator}$$

$$1\,\mathrm{eV} < T < 10\,\mathrm{eV} \quad , \quad n_e < 10^{20}\,\mathrm{m}^{-3} \quad \Rightarrow \quad \text{WEGA, W7-AS divertor}$$

3.3.2 Regime of Zeeman Splitting

The anomalous Zeeman effect occurs when the splitting of energy levels in the magnetic field is small compared to the field free fine structure splitting, and the Paschen-Back effect occurs when the splitting is large compared to the field free fine structure splitting. The regimes of the anomalous Zeeman and Paschen-Back effects are defined by a dimensionless parameter [26]

$$\xi = \frac{B\mu_0}{\Delta E_{FS}} \tag{3.16}$$

where the external magnetic field strength B is in T, and the Bohr magnetron μ_0 is in eV/T. ΔE_{FS} denotes the field free fine structure splitting in eV which is given in Equation (2.23). The anomalous Zeeman regime occurs for $\xi \ll 1$ and the Paschen-Back regime occurs for $\xi \gg 1$. The dependence of the magnetic field strength on the dimensionless parameter $\xi = B\mu_0/\Delta E_{FS}$ is plotted in Figure 3.9 for the He II of $n = 4$. According to the figure, for low magnetic field devices such as the WEGA

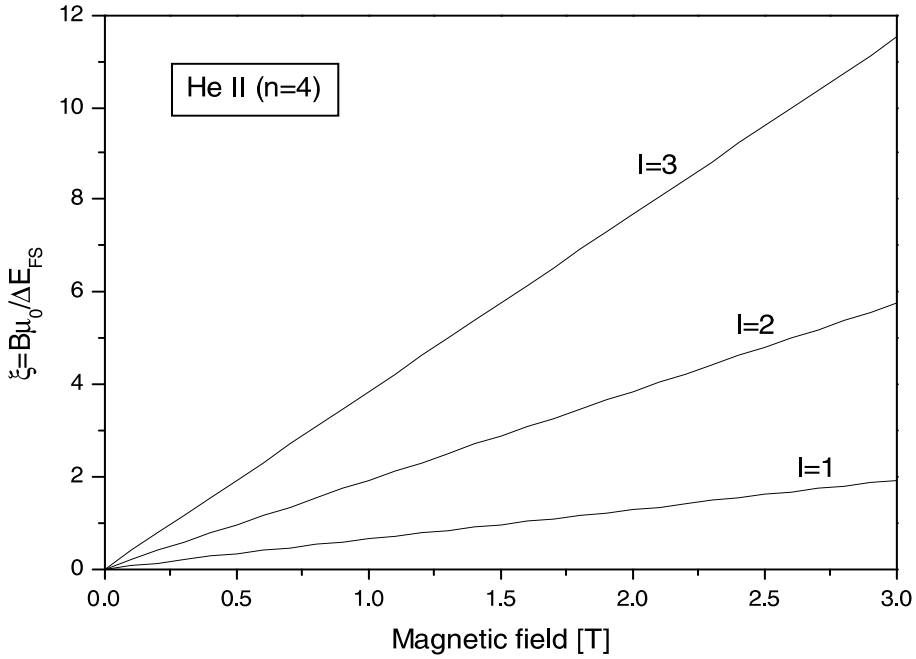

Figure 3.9: Dimensionless parameter $\xi = B\mu_0/\Delta E_{FS}$ for He II of n=4 plotted against the magnetic field strength B.

stellarator[2] ($B \leq 0.1\,\mathrm{T}$), the He II level $n = 4$ can be described by the anomalous Zeeman effect. By comparison, for high magnetic field devices such as the W7-AS divertor experiment ($B \sim 2.5\,\mathrm{T}$), the He II level $n = 4$ can be described by the Paschen-Back effect.

3.3.3 The simulation model for Zeeman splitting

In this section we describe how the new He II simulation models for the anomalous Zeeman and Paschen-Back regimes will be created. Since the He II line at 468.6 nm consists of 13 individual lines even in no magnetic field, we must begin by simplifying the situation. Figure 3.10 shows how the shape of the 13 individual He II lines changes with increasing temperature up to 10 eV. As indicated in Figure 3.10(a), four strong lines, $4d^2D_{3/2} \rightarrow 3p^2P_{1/2}$, $4d^2D_{5/2} \rightarrow 3p^2P_{3/2}$, $4f^2F_{5/2} \rightarrow 3d^2D_{3/2}$, and $4f^2F_{7/2} \rightarrow 3d^2D_{5/2}$, are dominant among 13 individual lines. As the temperature increases, the complicated shape becomes simpler, c.f. Figure 3.10(b) and (c), and finally becomes a single Gaussian profile c.f. Figure 3.10(d). According to Figure 3.10, it is sufficient to consider the Zeeman splitting only for the indicated 4 strong lines.

The relative line intensities of each component of anomalous Zeeman splitting for the 4 strong lines in a magnetic field of 0.1 T are calculated and illustrated in Figure 3.11 as a function of wavelength shift. The σ components are shown in the negative direction by convention. The sum of the intensity of two σ components is equal to

[2]See Section 6.1

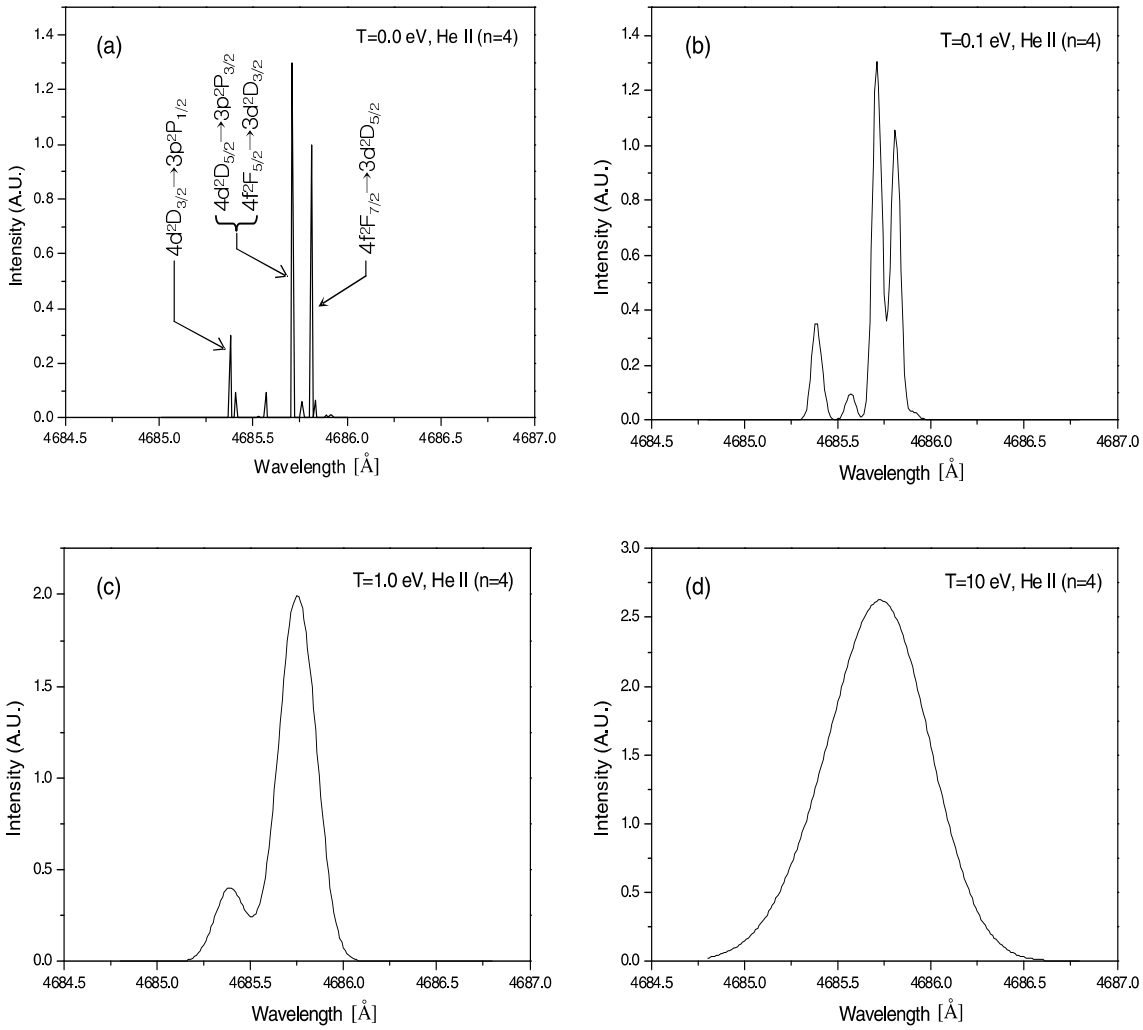

Figure 3.10: Doppler broadening of the He II lines ($n = 4 \rightarrow 3$) in no magnetic field. 13 individual lines are grouped within a narrow interval of 0.5 Å in (a). When the temperature is increased ((b),(c),and (d)), only four strong lines can be distinguished and finally the lines merge into a single Gaussian profile.

the intensity of one π component, and the sum of the intensity of all components is equal to the relative intensity of the individual line, which is shown in Table 3.2. The splitting shown in Figure 3.11 is the case for the transverse observation. When the lines are observed in the longitudinal direction (parallel to the magnetic field), the π component disappears and the intensity of the σ components doubles in strength as tabulated in Table 2.2. Although the splitting of the He II lines due to the anomalous Zeeman effect at $B = 0.1\,\mathrm{T}$ amounts to about 0.03 Å as shown in the figure, if the ion temperature is smaller than 1 eV, then the splitting is large enough compared to the Doppler broadening for the lines to be separable.

Figure 3.12 shows the relative line intensity of each Zeeman component in the Paschen-Back regime as a function of wavelength shift. As shown in this figure, the lines are widely separated compared to the other broadening mechanisms. For example, the splitting of the transition $4\mathrm{d}^2\mathrm{D}_{5/2} \rightarrow 3\mathrm{p}^2\mathrm{P}_{3/2}$ in red in Figure 3.12

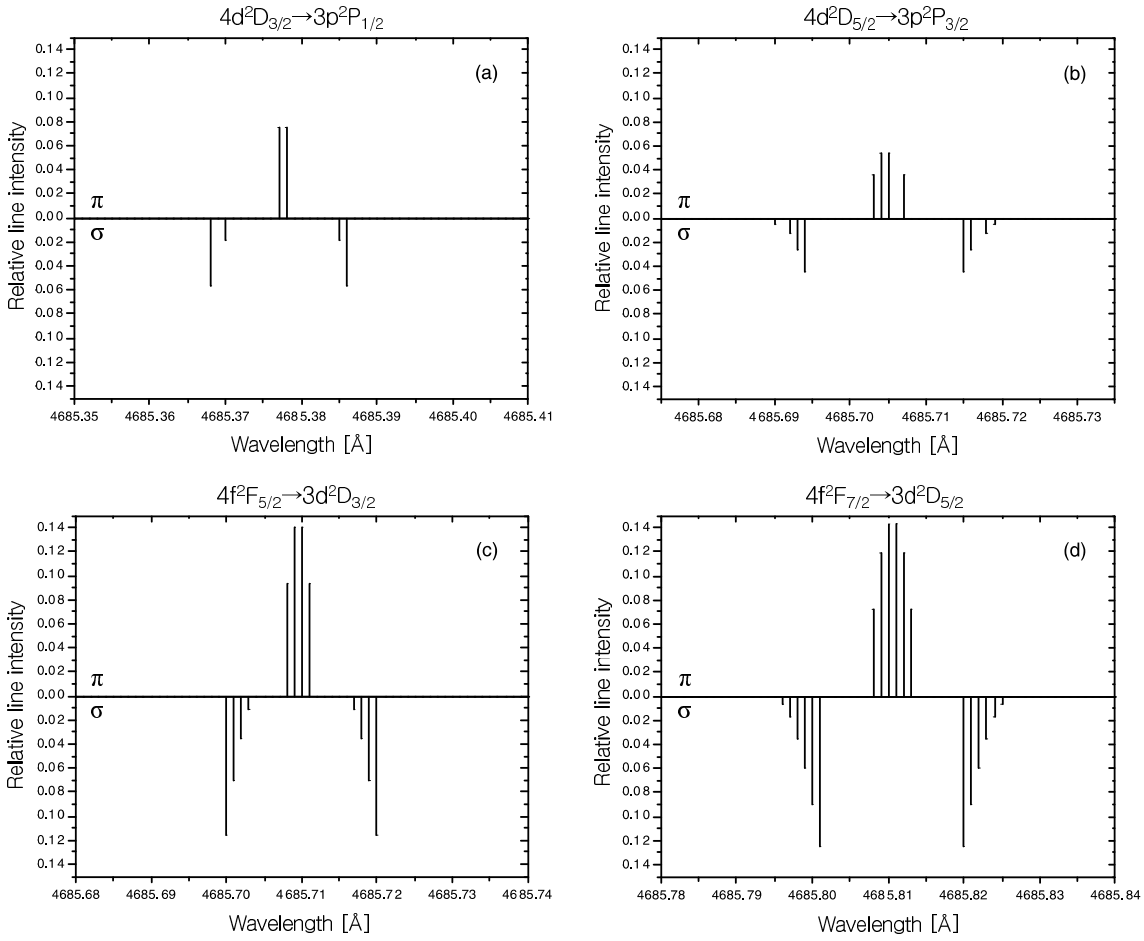

Figure 3.11: Anomalous Zeeman splitting of the He II lines for transverse observation, (a) $4d^2D_{3/2} \rightarrow 3p^2P_{1/2}$, (b) $4d^2D_{5/2} \rightarrow 3p^2P_{3/2}$, (c) $4f^2F_{5/2} \rightarrow 3d^2D_{3/2}$, and (d) $4f^2F_{7/2} \rightarrow 3d^2D_{5/2}$, as a function of wavelength shift at $B = 0.1\,\mathrm{T}$.

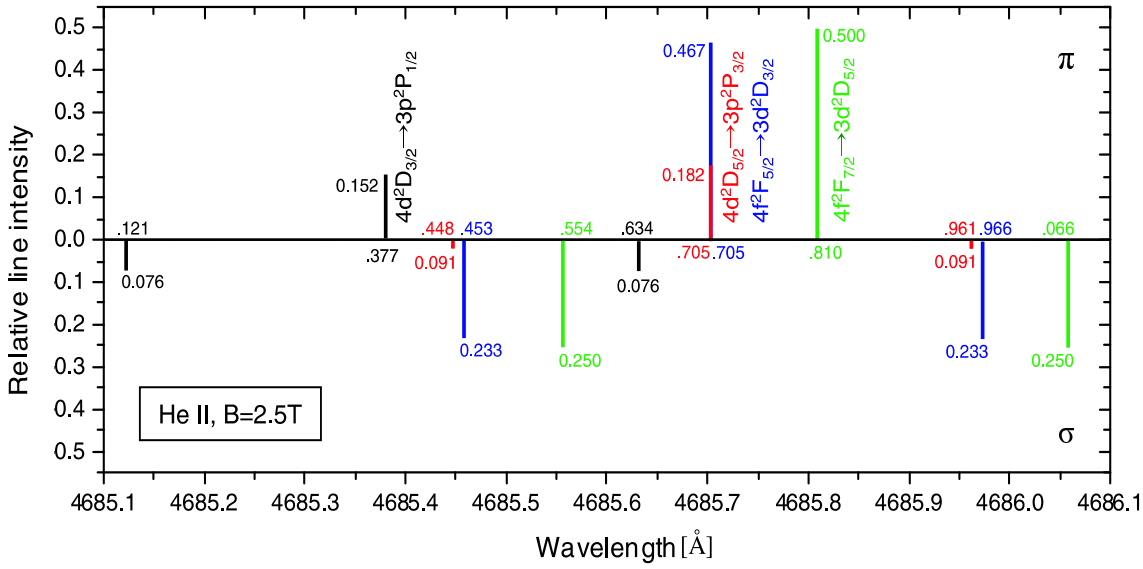

Figure 3.12: Splitting of the He II lines by the Paschen-Back effect at $B = 2.5\,\mathrm{T}$. The lines, $4d^2D_{3/2} \rightarrow 3p^2P_{1/2}$, $4d^2D_{5/2} \rightarrow 3p^2P_{3/2}$, $4f^2F_{5/2} \rightarrow 3d^2D_{3/2}$, and $4f^2F_{7/2} \rightarrow 3d^2D_{5/2}$, are colored in black, red, blue, and green, respectively.

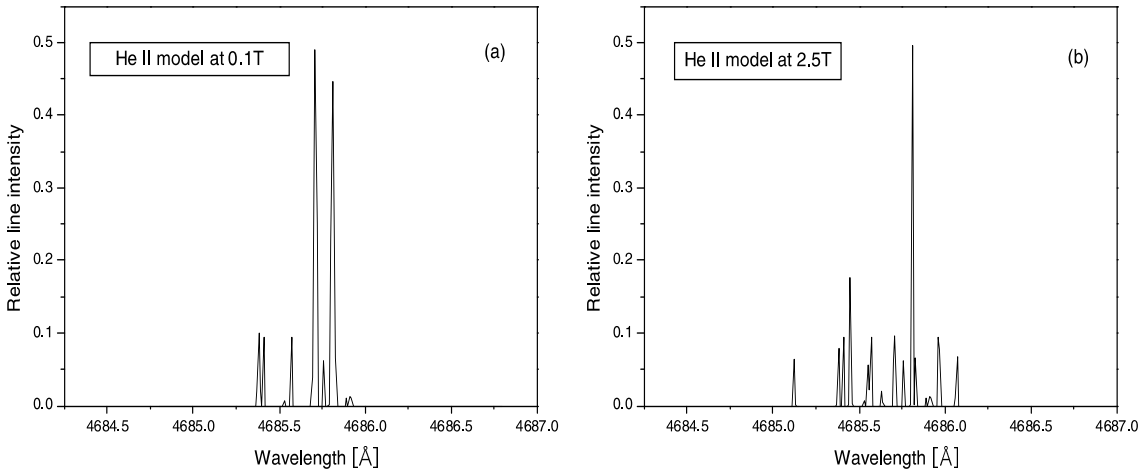

Figure 3.13: He II line models for the Zeeman splitting in (a) the Anomalous Zeeman regime ($B = 0.1\,\mathrm{T}$) and (b) the Paschen-Back regime ($B = 2.5\,\mathrm{T}$).

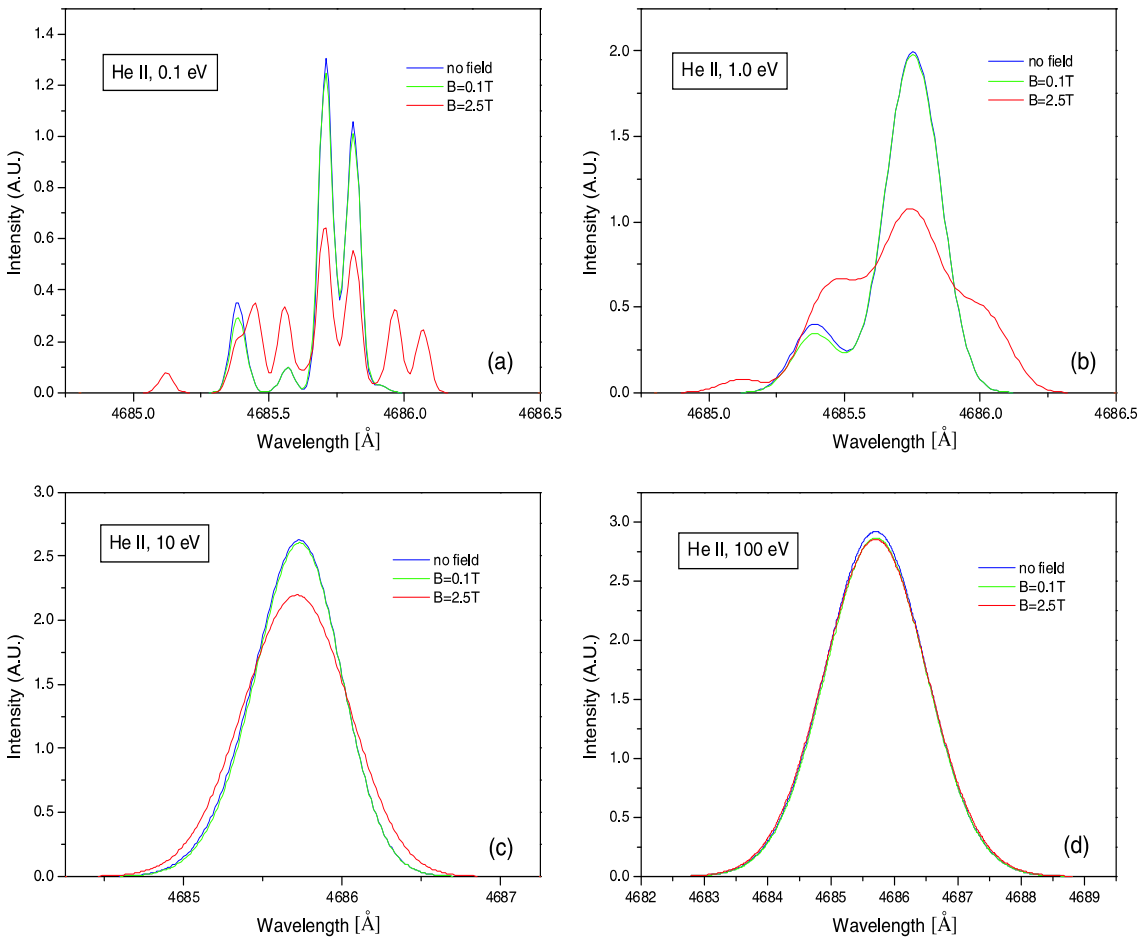

Figure 3.14: Comparison of the Doppler broadenings of three different He II line models by increasing the ion temperature up to 100 eV.

which separated by about 0.51 Å, i. e. equivalent to the Doppler broadening of the line at an ion temperature of 10 eV. The Doppler broadening for He II in the range of $1 - 100$ eV is shown in Figure 3.8. The field free simulation model for the He II line shown in Figure 3.6(b) can be improved by replacing the four strong He II multiplet lines, $4d^2D_{3/2} \rightarrow 3p^2P_{1/2}$, $4d^2D_{5/2} \rightarrow 3p^2P_{3/2}$, $4f^2F_{5/2} \rightarrow 3d^2D_{3/2}$, and $4f^2F_{7/2} \rightarrow 3d^2D_{5/2}$, with their Zeeman splitting components. Figure 3.13 shows the He II line models for the Zeeman splitting at $B = 0.1$ T and $B = 2.5$ T. Although the line split caused by the anomalous Zeeman effect leads to a larger number of components than by the Paschen-Back effect, Figure 3.13(a) shows a much simpler line profile because of the weak magnetic field strength. The Zeeman components in a high magnetic field are shifted by about one Doppler width at around 10 eV (Figure 3.13(b)). It can therefore be expected that the model will give quite different results in the low and the high temperature region. Figure 3.14 shows a comparison of the Doppler broadenings for the three different He II line models at magnetic field strengths of 0.0 T, 0.1 T, and 2.5 T, while increasing the ion temperature up to 100 eV. The model for no magnetic field is shown in blue, and the models at 0.1 T and 2.5 T are shown in green and red, respectively. The blue (no field) and green (0.1 T) lines are very similar to each other throughout the temperature range, but the red line which represents the splitting by the Paschen-Back effect at 2.5 T, behaves quite differently in the temperature range from 0.1 eV to 10 eV. At $T = 100$ eV all three line models are almost identical. The impact of the different models on the MOSS coherence simulations will be discussed in detail in the last section of this chapter.

3.4 Simulation algorithm

A MOSS coherence simulation code was created for the construction of the MOSS spectrometer. A flow chart describing the algorithm of the simulation code is shown in Figure 3.15. The simulation code creates a zero temperature spectral line model for a given condition and a Lorentzian filter model is added to the line model with a given wavelength and width as discussed in the previous sections. Then the Fourier transform of spectral feature, which is assumed to consist of individual only Gaussian shaped spectral lines, is determined. This calculation is performed for different temperatures within the temperature range of interest. The result of the simulation is the fringe visibility as a function of the number of waves.

3.5 Simulation results

The spectrum in Figure 3.4 shows the candidate lines from the W7-AS divertor, in which the He II line at 468.6 nm consists of 13 individual lines within a narrow

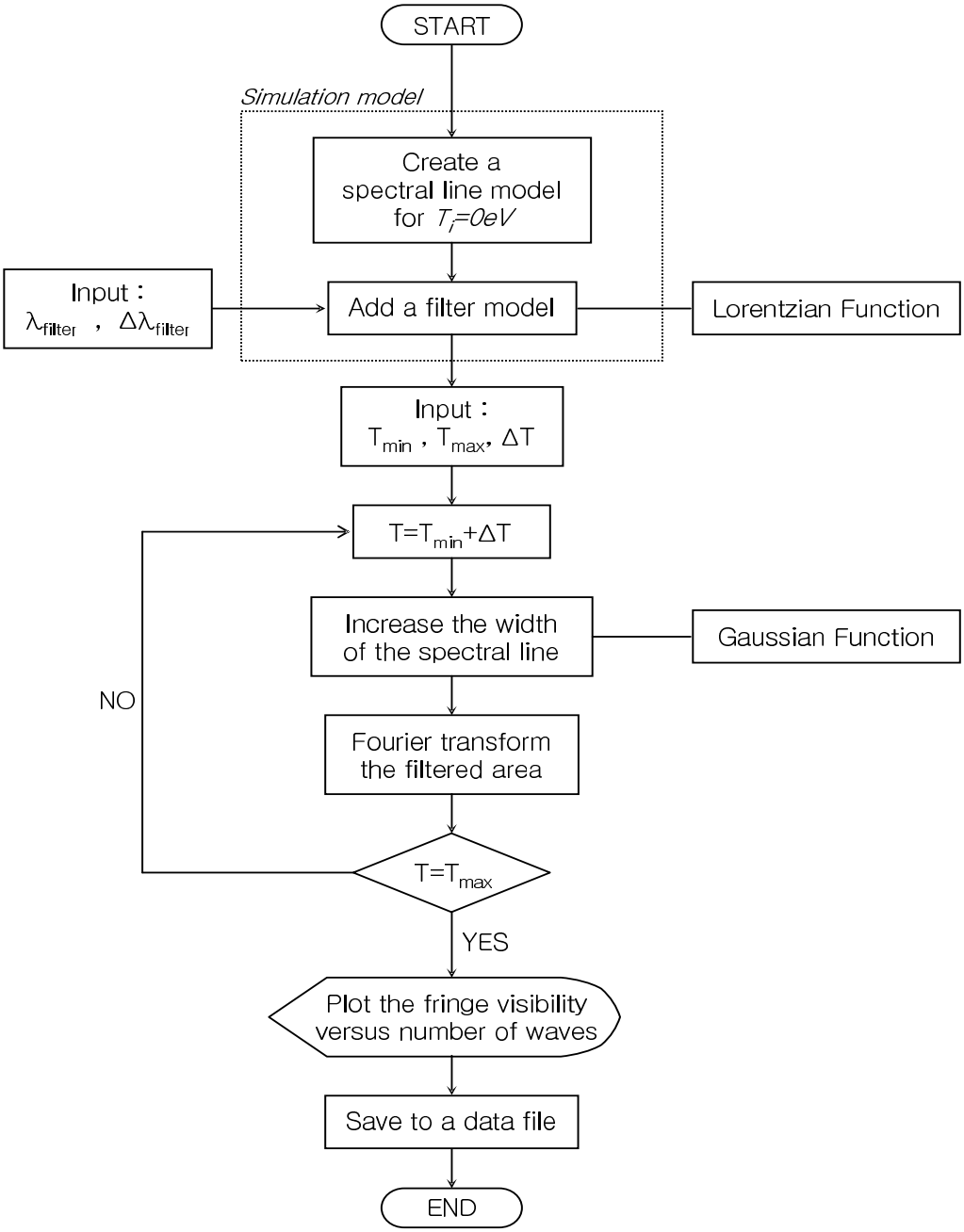

Figure 3.15: Flow chart describing the algorithm of the simulation code.

interval of 0.05 nm, and the C III line at 464.9 nm is a widely separated (0.4 nm) triplet. The simulation model for no magnetic field was created as introduced in Figure 3.6. For non-zero magnetic field, the line model for the Zeeman splitting as shown in Figure 3.13 can be applied to the simulation model. The results from these models are discussed in this section.

3.5.1 C III versus He II in no magnetic field

To investigate whether it is possible to isolate one of the candidate lines with a suitably chosen interference filter, a filter model was applied in the simulation model as shown in Figure 3.6. Although the filter model has a narrow enough bandwidth (10 Å FWHM) to isolate a candidate line, its tail still partially lets the light of neighboring lines pass. The filter model is approximated to a real optical interference filter which has a Lorentzian transmission profile. Figure 3.16 shows the results of the field free simulation model in various temperature ranges. The three graphs on the left are the He II filtered and the three on the right are the C III filtered case in the temperature ranges of $0.1 - 1.0\,\mathrm{eV}$, $1 - 10\,\mathrm{eV}$, and $10 - 100\,\mathrm{eV}$. The rapid beat patterns on the fringe visibility curves are due to the long tail of the filter model. This is closer to the reality. For the He II filtered case, the fringe visibility (or envelope of a coherence, see Figure 3.2) simply decreases in time delay as the temperature is increased. This is a typical behaviour of any MOSS spectrometer. In contrast, widely separated multiplet lines in the C III filtered case compared with He II lines, lead to a complicated fringe visibility in the time delay. This is why we mainly discussed the He II line in the previous sections. However, the high number of waves, for instance $N = 5000$ in the temperature range of $10 - 100\,\mathrm{eV}$ for the C III filtered case, causes the rapid beats to almost disappear and could allow a MOSS spectrometer to be constructed which makes use of the C III line at 464.9 nm. Despite the simulation result being quite complicated, using the C III line will be useful since many researchers are more interested in the C III than He II, for example, in divertor and edge physics. Carbon lines are an intrinsic impurity in machines with Carbon divertors. Consequently, these results show that temperature can be measured, even with a complex multiplet or with many individual lines. Since a MOSS spectrometer was constructed for the He II line, only the He II will be discussed in the following sections and chapters.

3.5.2 He II in a weak (0.1 T) magnetic field

The regime of the Zeeman splitting for the He II line was discussed in Section 3.3.2 in which it was shown that the splitting of the He II line in $B \leq 0.1\,\mathrm{T}$ can be described by the anomalous Zeeman effect. The line model for the He II in $B = 0.1\,\mathrm{T}$ was introduced in Figure 3.13(a). Although the model consists of tens

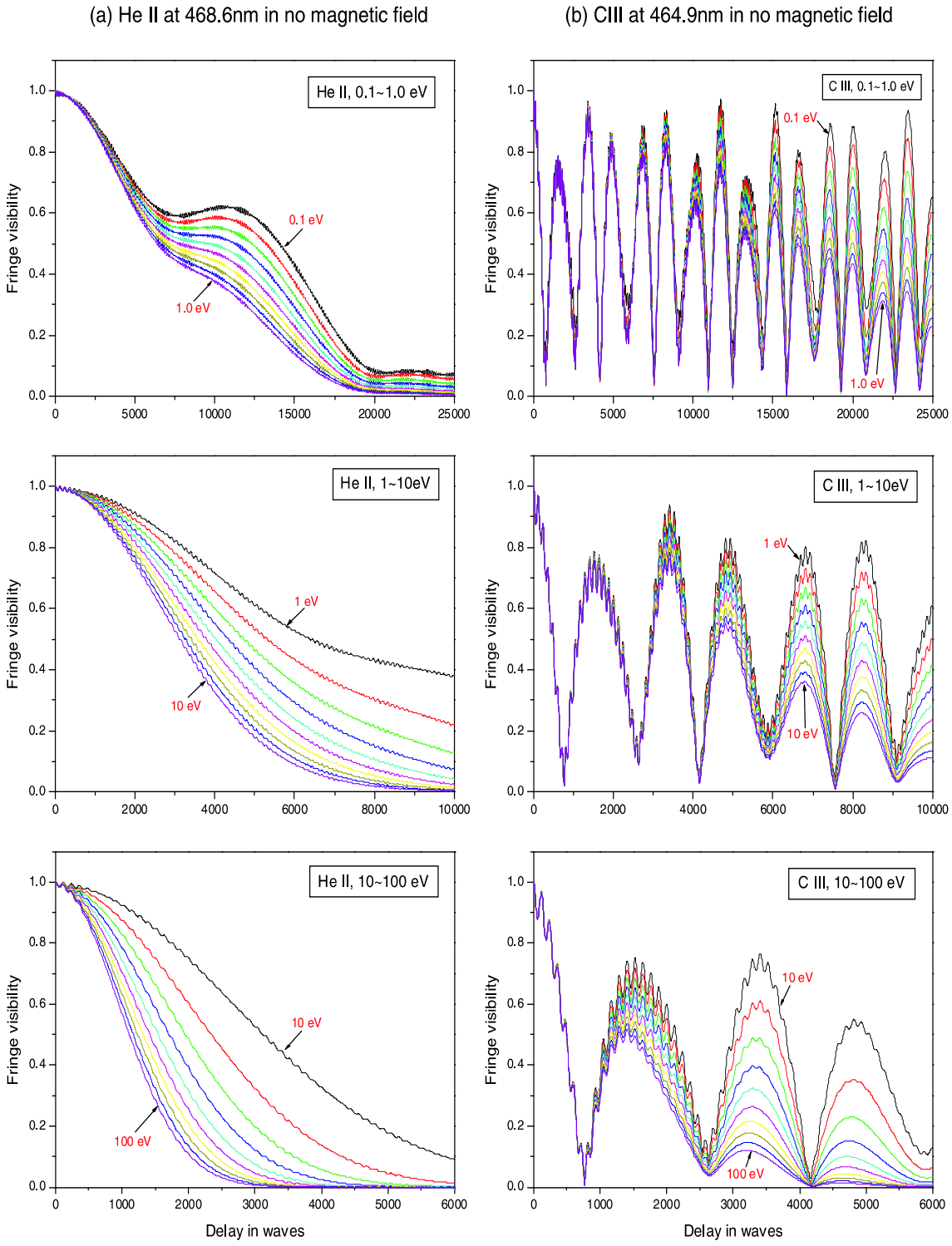

Figure 3.16: Simulation results for no magnetic field. (a) He II line filtered case showing a simple fringe visibility damping in the time delay, (b) C III line filtered case showing a complicated fringe visibility damping in the time delay from the widely separated triplet.

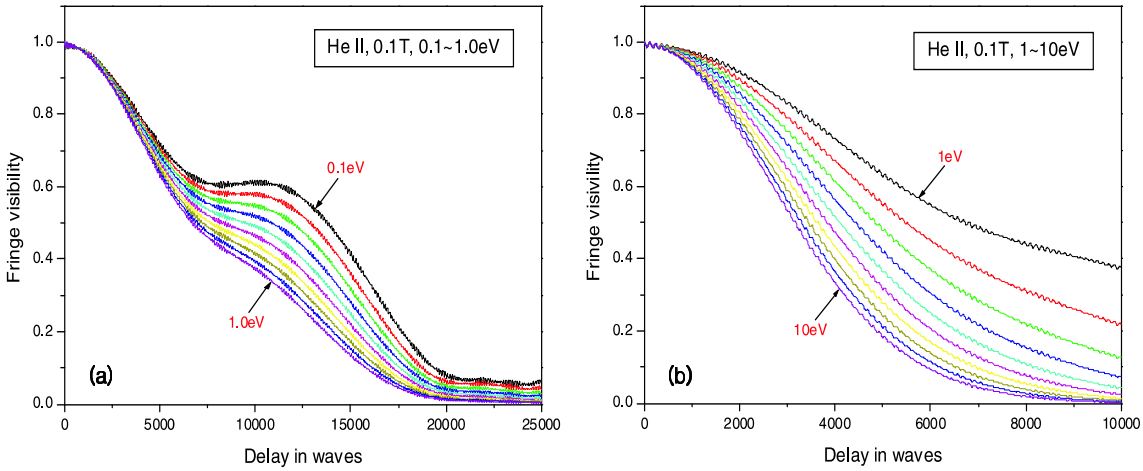

Figure 3.17: Simulation result for the He II line in a weak magnetic field, $B = 0.1\,\mathrm{T}$. (a) Temperature range of $0.1 - 1.0\,\mathrm{eV}$ and (b) $1 - 10\,\mathrm{eV}$.

of Zeeman components, there is little difference from the field free model shown in Figure 3.10(a) because of the small energy shift due to the weak magnetic field strength. Figure 3.17 shows the result of the model for a magnetic field strength of $B = 0.1\,\mathrm{T}$ where the left graph covers the temperature range of $0.1 - 1.0\,\mathrm{eV}$, and the right one is in the range of $1 - 10\,\mathrm{eV}$. As expected from Figure 3.14, the result of the simulation for $B = 0.1\,\mathrm{T}$ is very similar to the one without magnetic field shown in Figure 3.16. However, the results are not the same since the fringe visibility in a fixed delay is different. The MOSS spectrometer monitors the variation of the fringe visibility in a fixed delay. This simulation result explains the situation in the WEGA stellarator.

3.5.3 He II in a strong (2.5 T) magnetic field

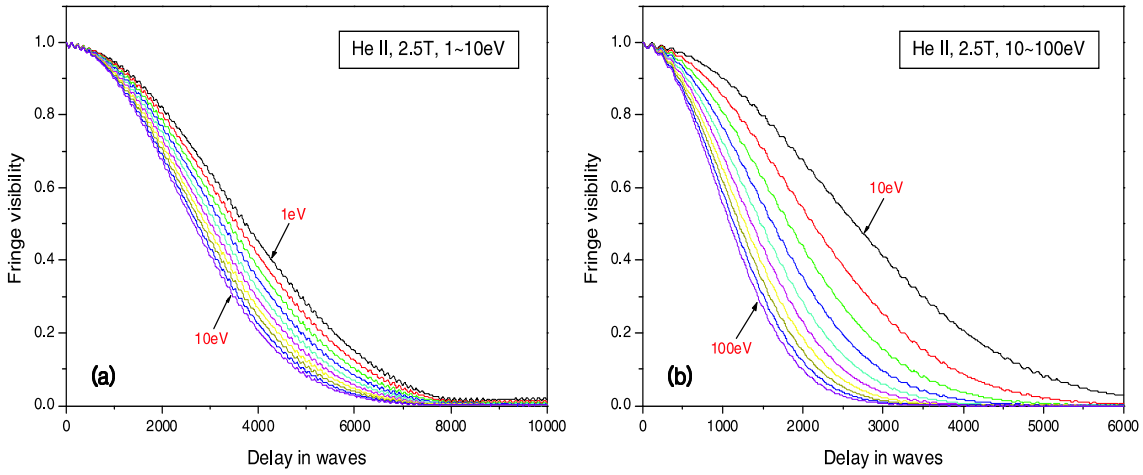

Figure 3.18: Simulation result for the He II line in a strong magnetic field, $B = 2.5\,\mathrm{T}$. (a) Temperature range of $1 - 10\,\mathrm{eV}$ and (b) $10 - 100\,\mathrm{eV}$.

In section 3.3.2, it was shown that the Zeeman splitting of the He II line in the

magnetic field strength of 2.5 T is in the Paschen-Back regime. The He II model for $B = 2.5\,\mathrm{T}$ is shown in Figure 3.10(b). Because of the strong magnetic field, the Zeeman components are strongly shifted. Figure 3.18 shows the result of the line model for the temperature range of $1 - 10\,\mathrm{eV}$ and $10 - 100\,\mathrm{eV}$. For the temperature range of $1 - 10\,\mathrm{eV}$, the fringe visibility decreases rapidly in wave delay compared to the other simulation results, but in the higher temperature range of $10 - 100\,\mathrm{eV}$, the difference becomes smaller, and finally the effect of the Zeeman splitting becomes almost negligible at 100 eV. This result is also expected from Figure 3.14, and it shows that if the temperature is less than 100 eV at $B = 2.5\,\mathrm{T}$, the Zeeman splitting must be considered. This simulation result was for the W7-AS stellarator.

4

The MOSS Spectrometer

The Modulated Optical Solid-State (MOSS) spectrometer measures the quantities related to the low order spectral moments of line emission from optically thin radiant media such as plasmas [33]. The MOSS spectrometer is essentially a Fourier-transform spectrometer about a fixed delay. It is designed to function in the optical region of the spectrum, and at the heart of the device are electro-optic birefringence crystals that modulate the wave delay. For a plasma in local thermodynamic equilibrium, the zeroth moment (brightness) is the average signal level, the first moment (phase shift) is the interferometric phase which represents the flow speed, and the second moment (contrast) is the fringe visibility which yields the ion temperature. A CCD camera with suitable imaging optics is used in the MOSS spectrometer so that the system can measure 2-dimensional ion temperature and the flow speed distributions. In this chapter the principles of this spectrometer are introduced and its performance is discussed.

4.1 Fourier transform spectrometer

Fourier transform spectroscopy is a measurement technique whereby spectra are collected based on the response from a pulse of electromagnetic radiation. The advantage of this Fourier transform spectrometer is that it can be used for very weak light sources by means of its efficient utilization of the available light.
The Fourier transform spectrometer can be explained starting from the concept of a Michelson interferometer with a movable mirror as shown in Figure 4.1. In the figure, a light ray is divided into two mutually coherent beams, and these rays are reunited after traveling different optical paths. If the light is not monochromatic but has a spectral composition given by the function $G(\omega)$, then the intensity at the detector varies in a manner that depends on the particular spectrum. By recording the intensity as a function of the path difference, the power spectrum $G(\omega)$ can be deduced. This method of obtaining a spectrum is called Fourier transform spectroscopy.
The intensity I of non-monochromatic light at the detector in terms of wave number

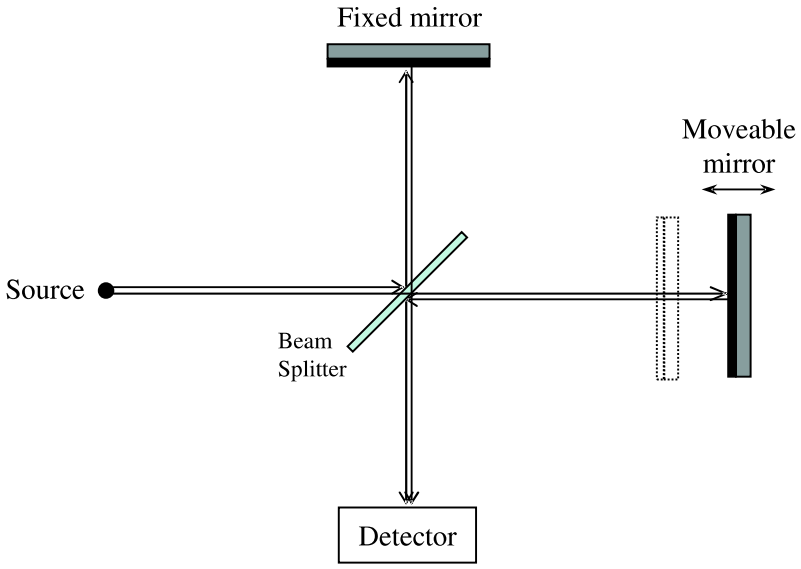

Figure 4.1: The Michelson interferometer uses a moveable mirror, which is an arrangement also used in Fourier transform spectroscopy.

k $(= \omega/c)$ is given by a summation over the complete spectrum [38],

$$\begin{aligned} I &= \int_0^\infty (1 + \cos kx) G(k) dk \\ &= \int_0^\infty G(k) dk + \int_0^\infty G(k) \frac{e^{ikx} + e^{-ikx}}{2} dk \\ &= \frac{1}{2} \left[I(0) + \int_{-\infty}^\infty e^{ikx} G(k) dk \right] \end{aligned} \tag{4.1}$$

or

$$W(x) = 2I(x) - I(0) = \int_{-\infty}^\infty e^{ikx} G(k) dk \tag{4.2}$$

where $I(0)$ is the intensity for zero path difference, and $W(x)$ and $G(k)$ constitute a Fourier transform pair. Accordingly,

$$G(k) = \frac{1}{\sqrt{2\pi}} \int_{-\infty}^\infty W(x) e^{ikx} dx. \tag{4.3}$$

That is, the power spectrum $G(k)$ is the Fourier transform of intensity function $W(x) = 2I(x) - I(0)$.

In the case of the MOSS spectrometer, when a light ray passes through a birefringence crystal the incident light is separated into two rays, ordinary and extraordinary, which travel in different directions. An electro-optic crystal plays an important role in the MOSS spectrometer, much like the moveable mirror in the Fourier transform spectrometer. The MOSS spectrometer is also very effective for weak light emissions. A more detailed theory of the MOSS spectrometer is discussed in the following sections.

4.2 Doppler spectroscopy

Doppler spectroscopy is a technique for measuring the ion temperature and velocity behavior from the light emission of an optically thin plasma. The line shape is determined by the Doppler shift of individual particles. When the velocity distribution is in local thermal equilibrium, it can be characterized by three spatially varying parameters, namely, the emission brightness, the drift velocity, and the species temperature. The Radon transform (introduced in Appendix A.2) of the brightness-weighted bulk drift and the temperature of the ion velocity distribution function can be obtained from the low order spectral moments of the line-integrated emission [35].

Plasma particles in thermal equilibrium have a Maxwell-Boltzmann velocity distribution. The Doppler spectrum is of Gaussian shape with a width proportional to the velocity of the particles. If a particle emits a characteristic radiation at a frequency ν_0 and is moving in the laboratory frame with a velocity $\mathbf{V}$ it will radiate light at a shifted frequency ν. The magnitude of the Doppler shift is related to the component of the particle's velocity along the propagation axis of the light.

Let us consider an inhomogeneous drifting isotropic velocity function

$$f(\mathbf{r}, \mathbf{v} - \mathbf{v}_D) \equiv f_0(\mathbf{r}, v) \tag{4.4}$$

where $\mathbf{v} = \mathbf{V}/c$ is a normalized velocity coordinate, $v = |\mathbf{v}|$, and $\mathbf{v}_D$ is the local first-moment drift velocity. If we write a normalized optical frequency coordinate

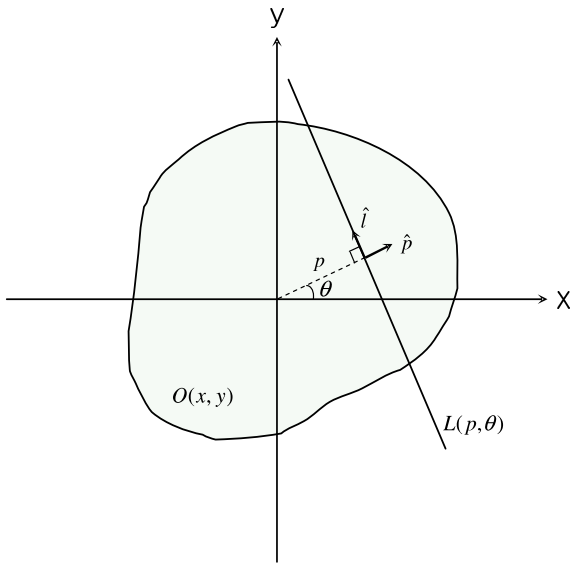

Figure 4.2: A viewing line $L(p, \theta)$ through an object $O(x, y)$. $\hat{\mathbf{l}}$ and $\hat{\mathbf{p}}$ are unit vectors of the coordinate rotated by the angle θ from the $x - y$ axes.

$\xi \equiv (\nu - \nu_0)/\nu_0 = \Delta\nu/\nu_0$, then the emissivity at frequency ξ and position $r = (x, y)$ in the plasma in the direction of view $\hat{\mathbf{l}}$ is given by a velocity-space line integral over

the velocity function f [32]

$$I(\mathbf{r}, \xi; \hat{\mathbf{l}}) = I_0(\mathbf{r}) \cdot g(\mathbf{r}, \xi; \hat{\mathbf{l}}) \tag{4.5}$$

where

$$g(\mathbf{r}, \xi; \hat{\mathbf{l}}) = \int f(\mathbf{r}, \mathbf{v} - \mathbf{v}_D)\delta(\xi - \mathbf{v} \cdot \hat{\mathbf{l}})d\mathbf{v} \tag{4.6}$$

is the local emission spectrum [34], and

$$I_0(\mathbf{r}) = \int g(\mathbf{r}, \xi; \hat{\mathbf{l}})d\xi \tag{4.7}$$

is the local emission spectrum with spectrally integrated isotropic intensity. In equation (4.6), the Delta function selects the velocity distribution of f of the viewing line L that contributes through the Doppler effect to the optical intensity at normalized frequency ξ.
Here by using the two-dimensional Radon transform (see Chapter A.2) the integral of the emission over the viewing line $L(p, \theta)$ is given by

$$\begin{aligned} g(p, \theta; \xi) &= \int I(\mathbf{r}, \xi; \hat{\mathbf{l}})\delta(p - \mathbf{r} \cdot \hat{\mathbf{p}})d\mathbf{r} \\ &\equiv \int_L I(\mathbf{r}, \xi; \hat{\mathbf{l}})dl \end{aligned} \tag{4.8}$$

where $d\mathbf{r} = dxdy$, θ is the angle of the viewing line L, and $p = x\cos\theta + y\sin\theta$ is the smallest distance to the origin of the coordinate system as illustrated in Figure 4.2. According to equation (4.8), $g(p, \theta; \xi)$ is proportional to $g(\mathbf{r}, \xi; \hat{\mathbf{l}})$, so that the Fourier transform of equation (4.6) over the normalized frequency coordinate separates the contributions from the drift and the body of the distributions. With $\mathbf{u} \equiv \mathbf{v} - \mathbf{v}_D$ and $du = d\mathbf{v}$, the Fourier transform of equation (4.6) can be written as

$$\begin{aligned} G(\mathbf{r}, \phi\hat{\mathbf{l}}) &\equiv \int e^{-i\phi\xi} g(\mathbf{r}, \xi; \hat{\mathbf{l}})d\xi \\ &= \int\int f(\mathbf{r}, \mathbf{u})dldu \int e^{-i\phi\xi}\delta(\xi - \mathbf{v}_D \cdot \hat{\mathbf{l}} - \mathbf{u} \cdot \hat{\mathbf{l}})d\xi \\ &= \int e^{i\phi\mathbf{v}_D \cdot \hat{\mathbf{l}}}dl \int f(\mathbf{r}, \mathbf{u})e^{i\phi\mathbf{u} \cdot \hat{\mathbf{l}}}du \\ &= e^{i\phi\mathbf{v}_D \cdot \hat{\mathbf{l}}} G_0(\mathbf{r}, \phi) \end{aligned} \tag{4.9}$$

where $G_0(\mathbf{r}, \phi)$ is a central slice of the Fourier transform of the spherically symmetric distribution $f_0(\mathbf{r}, v)$ [35]. The intensity signal obtained using an ideal Fourier transform spectrometer can be expressed as

$$S_{\pm}(\phi) = \frac{\mu_0}{2}\{1 \pm \mathcal{R}[\gamma(\phi; \hat{\mathbf{l}}) \exp(i\phi)]\} \tag{4.10}$$

where the total interferometer phase delay is $\phi = 2\pi\nu_0\tau$ with τ being the interferometer time delay, and the optical coherence (or fringe visibility) in the local thermodynamic equilibrium is given by [35]

$$|\gamma(\phi;\hat{\mathbf{l}})| = \frac{1}{\mu_0}\int_L G_0(\mathbf{r},\phi)dl \tag{4.11}$$

$$= \frac{1}{\mu_0}\int_L I_0(\mathbf{r})\exp[-T_S(\mathbf{r})/T_C]dl \tag{4.12}$$

Here $T_S(\mathbf{r})$ is the ideal species temperature, and the characteristic temperature T_C (in K) is given by

$$T_C = \frac{2m_s c^2}{k_B\phi^2} \tag{4.13}$$

since

$$k_B T_C = \frac{1}{2}m_s v_c^2 \tag{4.14}$$

where the characteristic velocity $v_c = 2c/\phi$, k_B is the Boltzmann constant, and c is the speed of light. Also the change in the interferometer phase due to the Doppler shift is given by [34]

$$\frac{\delta\phi}{\phi} = \frac{1}{\mu_0|\gamma|}\int_L G_0(\mathbf{r},\phi)\mathbf{v}\cdot\hat{\mathbf{l}}dl \tag{4.15}$$

This equation is a vector field line integral whose inverse gives the velocity of the field $G_0\mathbf{v}_D$.

4.3 Modulated Optical Solid-State Spectrometer

The MOSS spectrometer monitors the temporal coherence of an isolated line by polarization interferometric techniques. When the emission line is broadened, i.e. with increasing temperature, the fringe visibility decreases. This is the quantity measured by the MOSS spectrometer. It is therefore necessary to modulate the phase delay in order to resolve the maxima and minima of fringes. This modulation is achieved by electro-optic phase modulation. Electro-optic phase modulation by applying a time varying high voltage which satisfies a suitable modulation and demodulation algorithm. The total phase retardation in the system can be expressed as

$$\phi = \phi_0 + \phi_1 \sin\Omega t. \tag{4.16}$$

Here substituting ϕ into Equation (4.10), obtain

$$S_\pm(\phi) = \frac{\mu_0}{2}\{1 \pm |\gamma(\phi;\hat{\mathbf{l}})|\cos(\phi_0 + \phi_1\sin\Omega t)\} \tag{4.17}$$

where μ_0, $|\gamma(\phi;\hat{\mathbf{l}})|$, and ϕ_0 are directly related to the unknown velocity distribution parameters: the source intensity I_0, the emitting species temperature T_S, and the

Doppler shift $\mathbf{v}_D$.
Writing $k_0 = 2\pi\nu_0/c$, a birefringence crystal plate of thickness L introduces a phase delay between the orthogonally polarized ordinary and extraordinary characteristic waves,

$$\phi_0 = k_0 BL = 2\pi\mu_0\tau_0 \equiv 2\pi N \tag{4.18}$$

where B is the birefringence of the crystal plate, and N is the order of interference. If we write $|\gamma(\phi;\hat{\mathbf{I}})| \equiv \zeta$, the contrast (or total fringe visibility) $\zeta = \zeta_I\zeta_S$ includes an instrument component

$$\zeta_I = \exp(-T_I/T_C) \tag{4.19}$$

and a plasma component

$$\zeta_S = \exp(-T_S/T_C) \tag{4.20}$$

where T_I is the instrument component temperature and T_C is the characteristic temperature set by the instrument delay. The instrument fringe contrast is determined by the collected light solid angle and optical imperfections. This is very similar to the slit function of the grating spectrometer [35] and will be discussed in detail in Section 4.6.

4.4 Optical layout of a MOSS spectrometer

Figure 4.3 illustrates the optical layout of a MOSS spectrometer for the example of He II line. Behind the collimation lens, the unpolarized parallel light rays pass through an interference filter. We use here a filter centered at $\lambda_0 = 468.9\,\text{nm}$ with 1.0 nm FWHM bandwidth that isolates the He II line emission of the $n - n^{'} = 4 - 3$ transitions at 468.6 nm. This filtered beam traverses the first sheet polarizer that transmits the horizontally polarized component. The polarized light then passes through two crossed birefringent lithium niobate ($LiNbO_3$) plate modules which are located on either side of a half wave plate. The optical axis (or z-axis) of the lithium niobate plates is oriented at 45° to the plane of polarization. When the light passes through the crossed modulation plates it separates into two characteristic waves; extraordinary and ordinary. But since the high voltage is applied to the second plate with reversed polarity, the no net time delay is generated. The half wave plate between two crossed modulation plates compensates the hyperbolic fringe pattern and thereby allows us to operate the system at a larger Field of View (FOV)[36]. The interference images are created by passing the light through a lithium niobate birefringence delay plate and a second sheet polarizer. Finally, a camera lens focuses the modulated and interferenced light onto a 2D CCD chip. The details of each optical element and the properties of light at each point are discussed in the following sections.

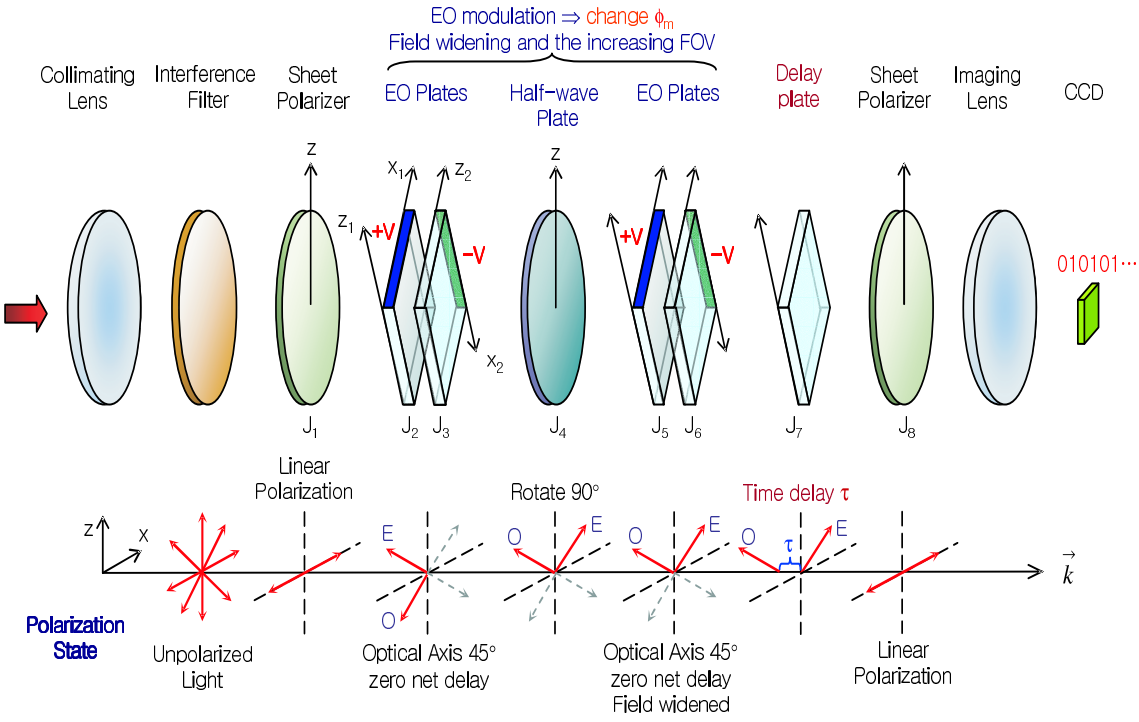

Figure 4.3: Optical layout of a MOSS spectrometer. The different orientations of the z-axes indicate the orientation of the optical axis of each individual birefringent optical element.

4.4.1 Interference filter for an imaging system

The interference filter is used for the wavelength selection in a narrow bandpass. Interference filters are made by depositing alternating layers of dielectric materials on a glass or quartz window. The thickness of the layer is such that most waves will be reflected, but the light at some frequencies is transmitted through the filter. Since the transmitted light shows negligible distortion from the interference coating, the filters can be used in an imaging system. An interference filter at 468.9 nm with 1.0 nm FWHM bandpass is used for the He II line isolation.

4.4.2 Anisotropic Retarder and Birefringence

Birefringence is the change in refractive index with the polarization of light. A birefringent crystal divides incident light into two oppositely polarized ordinary and extraordinary components. Many crystalline materials exhibit birefringence naturally, and there are also a number of crystals that need application of a voltage to induce birefringence. This phenomenon is called the electro-optic effect. The lithium niobate crystal which is used as a delay plate and the electro-optic crystals which are used in the MOSS spectrometer are both birefringent and electro-optic. The effect of optical materials such as birefringent crystals is characterized by n_o and n_e which are the refractive indices for the ordinary and extraordinary components.

The Jones matrix for a birefringent material of thickness L is given by

$$\mathbf{J_B} = \begin{pmatrix} e^{-i2\pi n_e L/\lambda} & 0 \\ 0 & e^{-i2\pi n_o L/\lambda} \end{pmatrix} = e^{-i2\pi n_e L/\lambda} \begin{pmatrix} 1 & 0 \\ 0 & e^{i2\pi BL/\lambda} \end{pmatrix} \tag{4.21}$$

where

$$B = n_e - n_o \tag{4.22}$$

is the linear birefringence in the plane perpendicular to the propagation of the light. The factor $e^{-i2\pi n_e L/\lambda}$ is omitted in the Jones matrix since it does not contribute to the calculation of the light intensity. The matrix can be rewritten as

$$\mathbf{J_B} = \begin{pmatrix} 1 & 0 \\ 0 & e^{i\phi} \end{pmatrix}. \tag{4.23}$$

Here

$$\phi = \frac{2\pi BL}{\lambda} \tag{4.24}$$

is the phase difference (or retardation). For $\phi = \pi$, the matrix (4.23) describes the half wave plate. The Jones matrix for the half wave plate is

$$\mathbf{J_{\lambda/2}} = \begin{pmatrix} 1 & 0 \\ 0 & -1 \end{pmatrix}. \tag{4.25}$$

The half wave plate can be used to rotate the plane of polarized light by 90°. In the MOSS spectrometer a half wave plate is used for widening the FOV.

4.4.3 Electro-optic modulator

When certain kinds of birefringent crystals are placed in an electric field their indices of refraction are altered by the presence of the field. This effect is known as the *Pockels electro-optic effect* [38]. It is found to be directly proportional to an applied field strength. The phase retardation for a given applied field strength may be increased simply by making the crystal thicker. The electro-optic modulators using this effect are called Pockels cells. In the electro-optic modulator, a crystal is placed between two polarizers, and metal electrodes are placed on the sides of the crystal where the voltage is perpendicular to the light propagation. Figure 4.4 shows a setup for using a Pockels cell light modulator. Lithium niobate is a good electro-optic material since it has a larger electro-optic effect but a smaller voltage is needed to induce an electric field. In the MOSS spectrometer, as shown in Figure 4.3, an electro-optic modulator is a principle part of the optical system. Looking closer at the system, two horizontal linear polarizers, J_1 and J_8, are placed as a polarizer and

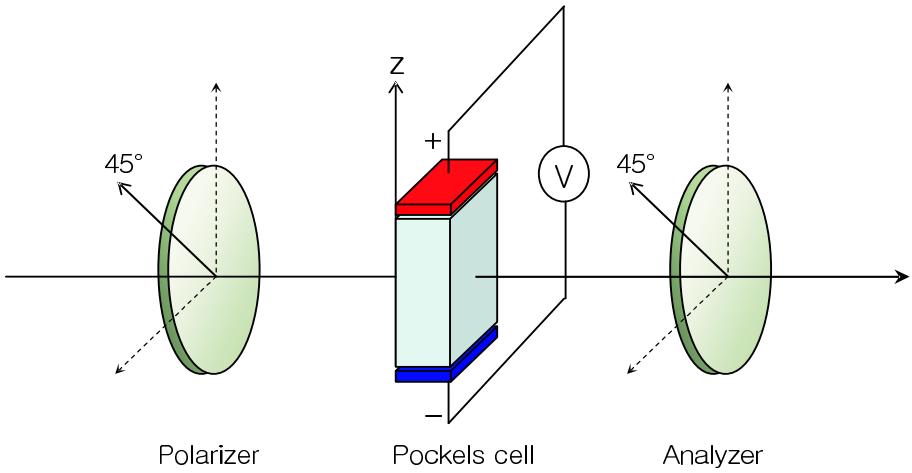

Figure 4.4: Schematic of a electro-optic modulator.

analyzer respectively. The Jones matrix of the horizontal linear polarizer is

$$\mathbf{J_{P_H}} = \begin{pmatrix} 1 & 0 \\ 0 & 0 \end{pmatrix} \tag{4.26}$$

In order to increase the electro-optic effect and absolute maximum field of view, two pairs of crossed crystals, J_2, J_3 and J_5, J_6, are placed either side of a half wave plate, J_4, at 45° to the z-axis. An additional crystal, J_7, is used as a delay plate since there is no net delay at the crossed plates.

4.4.4 Light intensity at the detector

The light intensity at the detector can be expressed by Jones calculus since the properties of light at each optical element of the MOSS spectrometer can be represented by Jones matrices. When incident light with electric vector $\mathbf{E}_0$ is transmitted through an optical element, the light will exit with electric field vector

$$\mathbf{E}_1 = \mathbf{J} \cdot \mathbf{E}_0 \tag{4.27}$$

where the Jones matrix $\mathbf{J}$ acts as a linear transformation since the Maxwell and constitutive equations are linear. The MOSS spectrometer consists of a cascade of optical elements such as polarizer, half wave plate, birefringent crystal, etc. The effect of each element is described by its Jones matrix, and the electrical field vector for light emerging from a cascade of n elements is given by

$$\mathbf{E}_n = \mathbf{J}_n \cdot \mathbf{J}_{n-1} \cdot \ldots \cdot \mathbf{J}_2 \cdot \mathbf{J}_1 \cdot \mathbf{E}_0. \tag{4.28}$$

The intrinsic z-axis of some of the optical elements of the MOSS spectrometer is rotated by the angle θ relative to the z-axis of the lab frame which is defined by the

z-axis of the first polarizer J_1 . In the lab frame, the rotated matrix $\mathbf{J}$ is given by

$$\mathbf{J} = \mathbf{R}_{-\theta} \cdot \mathbf{J}^{'} \cdot \mathbf{R}_{\theta} \tag{4.29}$$

where the rotational transform is given by

$$\mathbf{R}_{\theta} = \begin{pmatrix} \cos\theta & \sin\theta \\ -\sin\theta & \cos\theta \end{pmatrix} \tag{4.30}$$

Optical components which contribute to the electro-optic modulation are labelled as $\mathbf{J_1}$ to $\mathbf{J_8}$ in Figure 4.3. For a cascade of 8 optical elements each rotated with respect to the z-axis by some angle θ, the Jones matrix at the detector is

$$\begin{aligned} \mathbf{J_M} &= \mathbf{J_8} \cdot \mathbf{R_{(-45)}} \cdot \mathbf{J_7} \cdot \mathbf{R_{(45+45)}} \cdot \mathbf{J_6} \cdot \mathbf{R_{(-45-45)}} \cdot \mathbf{J_5} \\ &\quad \cdot \mathbf{R_{(45)}} \cdot \mathbf{J_4} \cdot \mathbf{R_{(45)}} \cdot \mathbf{J_3} \cdot \mathbf{R_{(-45-45)}} \cdot \mathbf{J_2} \cdot \mathbf{R_{(45)}} \cdot \mathbf{J_1} \\ &= \mathbf{J_{P_H}} \cdot \mathbf{R_{(-45)}} \cdot \mathbf{J_B} \cdot \mathbf{R_{(90)}} \cdot \mathbf{J_{B'}} \cdot \mathbf{R_{(-90)}} \cdot \mathbf{J_{B'}} \\ &\quad \cdot \mathbf{R_{(45)}} \cdot \mathbf{J_{\lambda/2}} \cdot \mathbf{R_{(45)}} \cdot \mathbf{J_{B'}} \cdot \mathbf{R_{(-90)}} \cdot \mathbf{J_{B'}} \cdot \mathbf{R_{(45)}} \cdot \mathbf{J_1} \end{aligned} \tag{4.31}$$

where the Jones matrices $\mathbf{J_B}$, $\mathbf{J_{\lambda/2}}$, and $\mathbf{J_{P_H}}$ are given in equations (4.23), (4.25), and (4.26) respectively. $\mathbf{J_{B'}}$ represents the crystals which may have different retardation with the delay plate, J_7. The electrical vector at the detector is then

$$\begin{aligned} \mathbf{E} &= \mathbf{J_M} \cdot \mathbf{E_0} = \begin{pmatrix} \frac{1}{2} + \frac{e^{i\phi}}{2} & 0 \\ 0 & 0 \end{pmatrix} \cdot \begin{pmatrix} \mathbf{E_x} \\ \mathbf{E_y} \end{pmatrix} \\ &= \frac{1}{2}(1 + e^{i\phi})\mathrm{E}_0 \end{aligned} \tag{4.32}$$

where the phase difference ϕ in a function of wavelength λ can also be written as a function of frequency ν by the simple relation of light, $\lambda\nu = c$, and since the birefringent phase delay also changes on the frequency, then equation 4.24 is

$$\phi = \frac{2\pi\nu LB(\nu)}{c}\kappa \tag{4.33}$$

where

$$\kappa = 1 + \frac{\nu_0}{B_0}\frac{\partial B}{\partial \nu} \tag{4.34}$$

accounts for the optical frequency dependence of the birefringence [35]. The intensity I at the detector can be expressed accordingly as

$$I = \langle E \cdot E^* \rangle = \frac{I_0}{2}(1 + \zeta\cos\phi) \tag{4.35}$$

where I_0 is the source intensity, and ζ is the fringe visibility or contrast. The above equation is a typical one for two-beam interferometers. In the equation, I

can be greater than or less then I_0, depending on the values of ϕ. The interference term $\zeta \cos\phi$ produces interference fringes since the ordinary and extraordinary rays combined at J_8 in Figure 4.3 are coherent.

4.5 Electro-optic crystals

In certain types of crystals, the application of an electric field results in a change in both the dimensions and the orientation of the index ellipsoid. This is called the electro-optic effect, and the crystals are called electro-optic crystals. Lithium niobate ($LiNbO_3$) and lithium tantalate ($LiTaO_3$) are the best materials for electro-optic applications due to their large electro-optic effects. These crystals are used as an electro-optic and as a delay plate in the MOSS spectrometer. In this section the light propagation in electro-optic crystals and the electro-optic effect in lithium niobate and lithium tantalate will be discussed making use of the concept of index ellipsoids and the linear electro-optic tensor r_{ijk}.

4.5.1 Light propagation in a uniaxial crystal

Most electro-optic crystals, including lithium niobate and lithium tantalate, are uniaxial. To explain the refractive indices in crystals, the index ellipsoid is used for the laboratory coordinates x, y, and z. Making use of the properties of the index ellipsoid, the refractive indices of the uniaxial crystal can be described as

$$\frac{x^2}{n_x^2} + \frac{y^2}{n_y^2} + \frac{z^2}{n_z^2} = 1 \tag{4.36}$$

where the refractive indices are

$$n_z = n_e \tag{4.37}$$

$$n_x = n_y = n_o \tag{4.38}$$

Figure 4.5 shows the index ellipsoid for a uniaxial crystal. The direction of propagation is along **s**. The intersection that is normal to **s** is an ellipse whose plane is shown in the figure. The refractive index of the ordinary ray, n_o, is equal to the length of OA. The length of OB is equal to the refractive index of the extraordinary ray, $n_e(\psi)$, which according to Figure 4.5 is given by [39]

$$\frac{1}{n_e^2(\psi)} = \frac{cos^2\psi}{n_o^2} + \frac{sin^2\psi}{n_e^2} \tag{4.39}$$

The refractive index varies from $n_e(\psi) = n_o$ for $\psi = 0°$ to $n_e(\psi) = n_e$ for $\psi = 90°$. Here ψ is the angle between the incident ray and the optical axis of the uniaxial crystal (z-axis in Figure 4.5). In a field widened imaging MOSS system of course

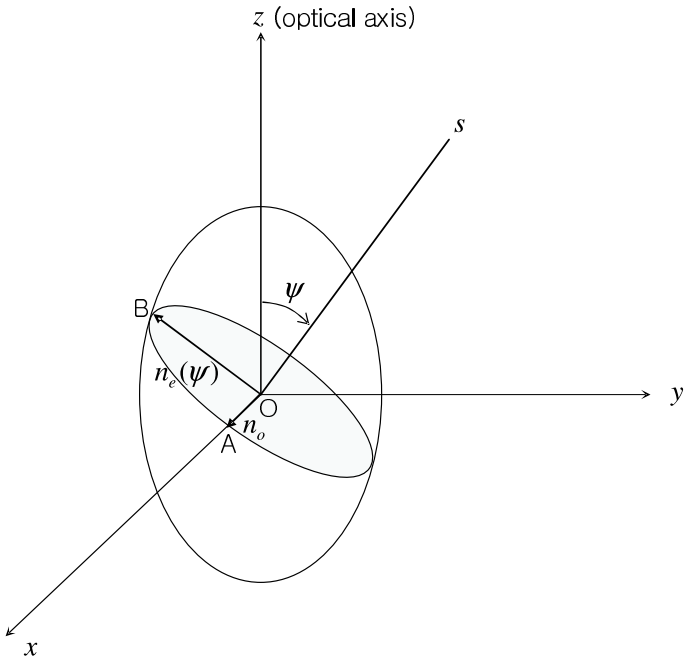

Figure 4.5: Normal modes determined from the index ellipsoid for a uniaxial crystal with $n_x = n_y = n_o$, $n_z = n_e$.

a wide range of ψ angles is covered. The propagation of light in a uniaxial crystal consists of an ordinary and an extraordinary ray. The electric field vector of the ordinary ray is always perpendicular to the direction of propagation **s**, but the field vector of the extraordinary ray is not.

4.5.2 Lithium Niobate ($LiNbO_3$) crystal

Lithium niobate or LN is a man-made dielectric material commonly used for optical applications such as optical modulators, Q-switches, beam deflectors, dielectric waveguides, and others. It is widely used in optical modulators because of its large electro-optic effect and its excellent transparency over a wide spectral range of 450 nm to 4μm. Lithium niobate is used not only for an electro-optic crystal but also as a delay plate in the MOSS spectrometer since it exhibits a sufficiently large birefringence naturally. See Figure 4.3.
Birefringence is the change in refractive index with the polarization light. The relationship between the change of refractive index and the applied electric field is given by [47]

$$\Delta\left(\frac{1}{n^2}\right)_{ij} = \sum_k r_{ijk} E_k \tag{4.40}$$

Where E_k is the k-th component of the electric field, r_{ijk} is the linear electro-optic coefficient tensor, and i, j, k corresponds to the crystal axes, x, y, z. Since the refractive index of the electro-optic crystal depends on the direction of light propagation, the crystal orientation and the direction of external electric field, 27 (=

3^3) components of r_{ijk} are required to describe the refractive index in the interaction with light. By using the symmetry in Equation (4.38), however, Equation (4.40) can be reduced to

$$\Delta\left(\frac{1}{n^2}\right)_i = \sum_k r_{ik}E_k \tag{4.41}$$

for $i = 1, 2, \cdots, 6$ and $k = 1, 2, 3$. Here the reduced notation of the linear electro-optic coefficient tensor for Lithium niobate which has trigonal $3m$ symmetry is [48]

$$r_{ik} = \begin{bmatrix} 0 & -r_{22} & r_{13} \\ 0 & r_{22} & r_{13} \\ 0 & 0 & r_{33} \\ 0 & r_{51} & 0 \\ r_{51} & 0 & 0 \\ -r_{22} & 0 & 0 \end{bmatrix} \tag{4.42}$$

where the four independent elements describing the electro-optic effect have numerical values of [47]

$$\begin{aligned} r_{13} &= 7.7 \times 10^{-12}\text{m/V}, \quad r_{33} = 28.8 \times 10^{-12}\text{m/V} \\ r_{22} &= 3.4 \times 10^{-12}\text{m/V}, \quad r_{51} = 18.2 \times 10^{-12}\text{m/V} \end{aligned} \tag{4.43}$$

When an electric field is applied to the crystal the index ellipsoid becomes distorted. The distortion of the index ellipsoid is given by

$$a_{xx}x^2 + a_{yy}y^2 + a_{zz}z^2 + 2a_{yz}yz + 2a_{xz}xz + 2a_{xy}xy = 1 \tag{4.44}$$

where the new coefficients a_{lm} in electric field $\mathrm{E} = (E_x, E_y, E_z)$ are

$$\begin{bmatrix} a_{xx} \\ a_{yy} \\ a_{zz} \\ a_{yz} \\ a_{xz} \\ a_{xy} \end{bmatrix} = \begin{bmatrix} 1/n_x^2 \\ 1/n_y^2 \\ 1/n_z^2 \\ 0 \\ 0 \\ 0 \end{bmatrix} + \begin{bmatrix} 0 & -r_{22} & r_{13} \\ 0 & r_{22} & r_{13} \\ 0 & 0 & r_{33} \\ 0 & r_{51} & 0 \\ r_{51} & 0 & 0 \\ -r_{22} & 0 & 0 \end{bmatrix} \cdot \begin{bmatrix} E_x \\ E_y \\ E_z \end{bmatrix} \tag{4.45}$$

There are two orientations which can be used for lithium niobate electro-optic applications. The first one uses a z-cut crystal. In this case the optical axis of the crystal is parallel to the direction of optical propagation, so there is no birefringence. The second one uses a y-cut crystal. For this case light propagates through the y-axis, and the electric field is applied in the z direction. In the MOSS spectrometer, y-cut crystals are used. The index ellipsoid for the Lithium niobate crystal due to an

applied electric field E_z ($E_x = E_y = 0$) to the device may written as

$$\frac{x^2}{n_0^2} + r_{13}E_z + \frac{y^2}{n_0^2} + r_{13}E_z + \frac{z^2}{n_e^2} + r_{33}E_z = 1 \tag{4.46}$$

Therefore two elements, r_{13} and r_{33}, of the coefficient tensor can describe the electro-optic effect of lithium niobate crystals used in the MOSS spectrometer.
The phase retardation resulting from the applied field $E_z = V/d$ is given by [39]

$$\Gamma = \frac{2\pi}{\lambda}(n_e - n_o)L - \frac{\pi}{\lambda}(n_e^3 r_{33} - n_o^3 r_{13})\frac{V}{d}L \tag{4.47}$$

where V is the applied voltage and d is the separation between the electrodes. In the above equation, the first term is the natural birefringence of the crystal, and the second term represents the phase change induced by the applied electric field. If the light is linearly polarized along the z-axis, the second term is reduced to

$$\Delta\phi = \frac{\pi}{\lambda}n_e^3 r_{33}\frac{V}{d}L. \tag{4.48}$$

The voltage required to change the phase by π is called the half-wave voltage for the modulation, and is given by

$$V_\pi = \frac{\lambda_0 d}{L\delta} \tag{4.49}$$

where $\delta = n_e^3 r_{33} - n_o^3 r_{13}$, and the refractive indices for the lithium niobate are $n_e = 2.2664$ and $n_o = 2.3697$ at 465.8 nm [47]. According to Equation (4.49), a thicker crystal which provides a larger interaction region needs a smaller half-wave voltage.
If the applied voltage is sinusoidal in time, the phase retardation can be written

$$\Gamma = \Gamma_0 + \Gamma_m \sin\omega_m t \tag{4.50}$$

where Γ_0 is the total phase retardation in the absence of applied voltage, and the modulation depth is

$$\Gamma_m = \frac{\pi V}{V_\pi} = \frac{\pi L V \delta}{\lambda_0 d}. \tag{4.51}$$

Note that if the modulator uses a pair of crystals whose z-axes are mutually perpendicular, Γ_0 is negligible since the natural birefringence term in Equation (4.47) cancels out.

4.5.3 Lithium Tantalate ($LiTaO_3$) crystal

Lithium tantalate or LT is also a widely used electro-optic material. Its optical properties are similar to those of lithium niobate crystals. Lithium tantalate has a trigonal 3m symmetry as does Lithium niobate, so that all the equations introduced

in the previous section also apply to Lithium tantalate. The birefringence of Lithium tantalate ($\simeq 0.004$) is much lower than that of lithium niobate ($\simeq -0.1$), but it has a similar electro-optic effect when the electric field is applied along the z-axis. The refractive indices of the Lithium tantalate are $n_e = 2.180$ and $n_o = 2.176$ at 633.0 nm. At the same wavelength, the electro-optic coefficients are given by [39]

$$\begin{aligned} r_{13} &= 8.4 \times 10^{-12}\text{m/V}, \quad r_{33} = 30.5 \times 10^{-12}\text{m/V} \\ r_{22} &= -0.2 \times 10^{-12}\text{m/V}, \quad r_{51} = 20.0 \times 10^{-12}\text{m/V} \end{aligned} \tag{4.52}$$

As shown in the above values, lithium tantalate does not have a useful r_{22} electro-optic coefficient. It is therefore not used in an optic axis propagation mode. As for the lithium niobate, y-cut crystals can be used in the MOSS spectrometer where a combination of the r_{13} and r_{33} electro-optic coefficients determines the electro-optic effect from Equation (4.47). There are several advantages in using lithium tantalate over lithium niobate in this mode. The Lithium niobate is limited for some high frequency applications, but no such limitations occur in Lithium tantalate until very high frequencies are encountered. Also, the optical transmission range of Lithium tantalate is similar to Lithium niobate, but it does not suffer the short wavelength optical damage effects. Due to the relatively small value of birefringence, Lithium tantalate is very stable with respect to variations in temperature. Because of these advantages, Lithium tantalate is used as an electro-optic modulator in the latest version of the MOSS system. The half-wave voltage and the modulation depth are in Equations (4.49) and (4.51), respectively. When the electric field is applied along the z-axis, the discussion in the previous section is valid for lithium tantalate as well.

4.6 Instrument function

The instrument function due to the instrument itself also causes a broadening of the spectral lines. The instrument function therefore must be determined so that the measurements can be corrected appropriately. In the case of the MOSS spectrometer, the interference pattern produced by the crystal plates (instrument phase), the contrast caused by the spatial coherence of an extended light source (instrument contrast), and the non-linearities of the detector may be the important instrument functions. In this section, the instrument phase and contrast will be discussed.

4.6.1 Instrument phase: Interference pattern with crystal plates

In a uniaxial crystal such as Lithium niobate the phase velocities correspond to a wave-normal direction that makes an angle ψ with respect to the optical axis. It

is because of the angle ψ that the interference pattern of a crystal plate can be observed. The interference pattern must be corrected for the 2D optical imaging. This correction process is called field widening or improving FOV (field-of-view) [36]. This is a very important technique for optical imaging. In this section, we will discuss how field widening works after deriving the equation for the phase difference between the ordinary and extraordinary rays in a function of ψ.

When an analyzing polarizer is placed behind the crystal plate (J_8 in Figure 4.3), the ordinary and extraordinary ray components are singled out and may be brought to interference in the focal plane. This is the principle of measuring the interferogram at the detector by modulating the refractive indices of the two components, n_e and n_o. However, since the electric field vector of the extraordinary ray is not perpendicular to the incident light ray as shown in Equation (4.39), each point in the light source will give rise to an intensity distribution in the conjugate point independently of all the other source points. This phenomenon makes the interference pattern on the crystal plate. Figure 4.7(a) shows the interference pattern produced by Lithium niobate crystals. It must be corrected for the 2D imaging.

To investigate the interference pattern of the crystal plate, we begin with the phase difference, $\phi(\theta)$, which depends on the angle of the incident light ray. Let θ, θ_o, and θ_e be the angles of incidence and two angles of refraction respectively as shown in Figure 4.6.

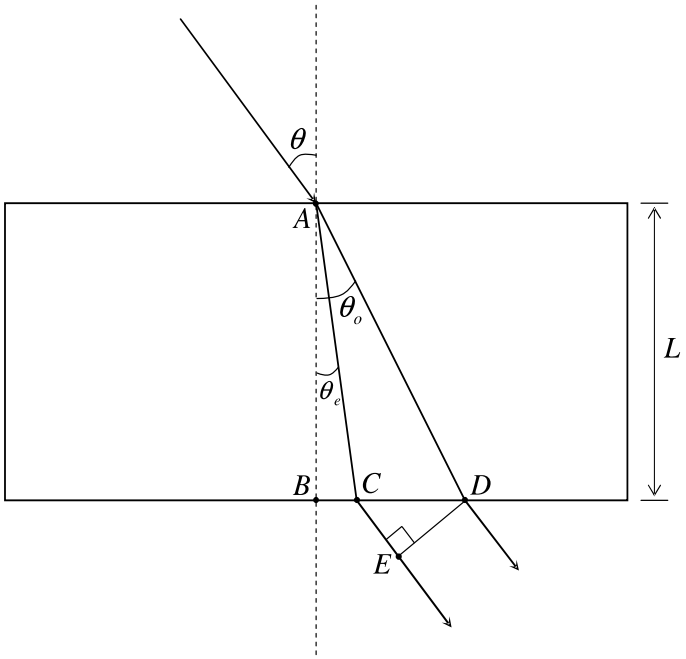

Figure 4.6: Determination of the phase difference between two waves transmitted in a crystal plate of thickness L.

The phase difference between the ordinary and the extraordinary rays is

$$\phi(\theta) = 2\pi \left(\frac{AC}{\lambda_e} + \frac{CE}{\lambda} - \frac{AD}{\lambda_o} \right) \tag{4.53}$$

where λ is the wavelength in air, $\lambda_o = \lambda/n_o$ and $\lambda_e = \lambda/n_e$ are the wavelengthes of the two refracted waves,

$$AD = \frac{L}{\cos\theta_o} \tag{4.54}$$

$$AC = \frac{L}{\cos\theta_e} \tag{4.55}$$

and

$$CE = CD\sin\theta = \cos\theta(\tan\theta_o - \tan\theta_e). \tag{4.56}$$

Substituting from (4.54), (4.55), and (4.56) into (4.53), we obtain

$$\phi(\theta) = 2\pi L\left[\frac{1}{\cos\theta_e}\left(\frac{1}{\lambda_e} - \frac{\sin\theta\sin\theta_e}{\lambda}\right) - \frac{1}{\cos\theta_o}\left(\frac{1}{\lambda_o} - \frac{\sin\theta\sin\theta_o}{\lambda}\right)\right] \tag{4.57}$$

Making use of the law of refraction we can replace $\sin\theta/\lambda$ by $\sin\theta_e/\lambda_e$ and by $\sin\theta_o/\lambda_o$, giving [40]

$$\begin{aligned}\phi(\theta) &= 2\pi L\left(\frac{\cos\theta_e}{\lambda_e} - \frac{\cos\theta_o}{\lambda_o}\right)\\ &= \frac{2\pi L}{\lambda}(n_e\cos\theta_e - n_o\cos\theta_o)\end{aligned} \tag{4.58}$$

By using Equation (4.39) and Snell's law, Equation (4.58) can be expressed in terms of θ and ψ as [39]

$$\phi(\theta,\psi) = \frac{2\pi L}{\lambda}\left(n_e\sqrt{1 - \frac{\sin^2\theta\cos^2\psi}{n_o^2} - \frac{\sin^2\theta\sin^2\psi}{n_e^2}} - n_o\sqrt{1 - \frac{\sin^2\theta}{n_o^2}}\right). \tag{4.59}$$

For small θ, $\sin^2\theta$ is much smaller than n_o^2 and n_e^2, therefore Equation (4.59) can be approximated as [45]

$$\phi(\theta,\psi) \approx \frac{2\pi BL}{\lambda}\left[1 - \frac{\theta^2}{2n_o}\left(\frac{\cos^2\psi}{n_o} - \frac{\sin^2\psi}{n_e}\right)\right] \tag{4.60}$$

This equation describes the hyperbolic interference pattern in a uniaxial crystal plate as shown in Figure 4.7(a). The detailed derivation of Equations (4.59) and (4.60) from Equation (4.58) is given in Appendix A.3. According to Equation (4.60) and Figure 4.7, since the phase shift $\phi(\theta,\psi)$ increases along the z-axis, the interference pattern can be compensated (field widening) by adding an additional plate whose z-axis is rotated by 90°. In Figure 4.3 a half-wave plate (J_4) in between two crossed plates rotates the optical axis by 90°. This is the field widening optical arrangement

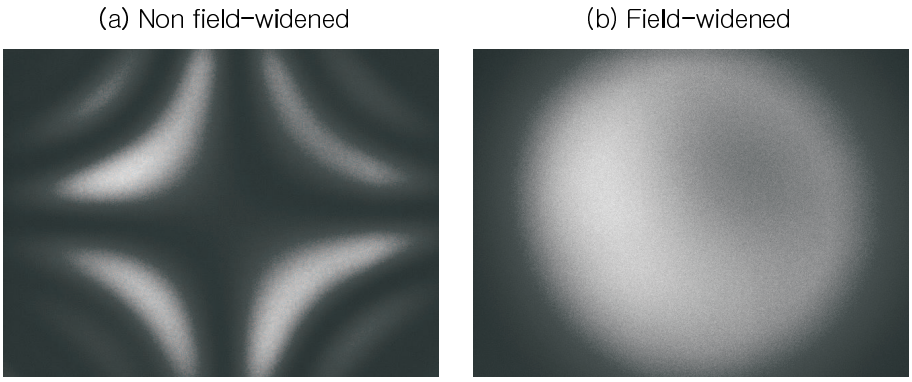

Figure 4.7: Images of an interference pattern with a crossed plate (a) and a field widened image with the optical arrangement described in the text (b). These images were taken by the CCD camera.

for the MOSS spectrometer. The field widened phase shift can be expressed as [36]

$$\begin{aligned} \phi_{wide}(\theta,\psi) &= \phi(\theta,\psi)+\phi(\theta,\psi+90^\circ) \\ &= \frac{2\pi BL}{\lambda}\left[2-\frac{\theta^2}{2n_o}\left(\frac{1}{n_o}-\frac{1}{n_e}\right)\right]. \end{aligned} \tag{4.61}$$

Note that this equation is independent of the angle ψ. Figure 4.7 (b) shows a field widened image by using the optical arrangement for field widening where the hyperbolic interference pattern has disappeared.

4.6.2 Instrument contrast: Spatial coherence

If there are two monochromatic waves whose phase difference is constant from a single point in space, then the two waves and their resulting wave are said to be mutually coherent. However, light from a real physical source is not monochromatic and does not originate from a single point in space. This means that there is always some finite spread of frequency (or line width) centered about some mean frequency and the source may be thought of as a large number of points in space. The line width is one of the quantities that we want to measure with the MOSS spectrometer, but the problem of coherence between two or more waves arriving at the same point on a detector along different optical paths, the so called spatial coherence, must be an instrument function.
For the case of extended sources such as plasmas or discharge lamps, the spatial coherence J can be explained by the Van Cittert-Zernike theorem [37, 45]

$$J(\mathbf{u}_1,\mathbf{u}_2)=\int_{\mathcal{S}} L(\mathbf{x})\frac{\mathbf{e}^{ik(R_2-R_1)}}{R_1R_2}d\mathbf{x} \tag{4.62}$$

where R_1 and R_2 are the travelling distances from an extended source $\mathcal{S}$ to the points P_1 and P_2, and $L(\mathbf{x})$ is the luminosity across the source. The above equation says

that the complex degree of coherence between a fixed point P_1 and a variable point P_2 in a plane illuminated by an extended source is equal to the complex amplitude produced at P_2 by a spherical wave passing through an aperture of the same size and shape as the extended source and converging to P_1. The instrument contrast of the MOSS spectrometer is defined as

$$\zeta_I = |J(\mathbf{u}_1, \mathbf{u}_2)| \tag{4.63}$$

The instrument contrast can be measured using a quasi monochromatic light source having a homogeneous light surface, so that the measured contrast can be used to get absolute temperatures from Equations (4.19) and (4.20), see Section 4.7.1.

4.7 Measurement principle

The MOSS measurement can be classified into three main procedures; modulation, demodulation, and calibration. Firstly, modulation is the process of changing the time-resolved signal in proportion to the information. Secondly, demodulation is the process of extracting the information from the modulated time-resolved signal. Thirdly, calibration is needed to get absolute plasma parameters. This process is shown in Figure 4.8. The source information is hidden in the light emitting from

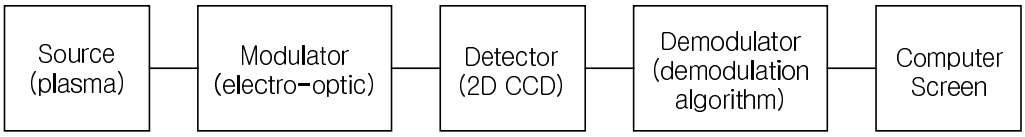

Figure 4.8: MOSS measurement system

the plasma. In the modulator section, the hidden information is modulated by an electro-optic technique. The detector changes an optical signal into a digitized voltage which is saved on a computer. Next, it is demodulated digitally by a demodulation algorithm. Finally, the extracted plasma parameters are displayed on the computer screen. To obtain absolute values of the parameters the calibration must be carried out before or after the measurement. The 4- and 3-frame phase demodulations and their demodulation algorithms are introduced in this section.

4.7.1 Electro-optic phase modulations

Electro-optic phase modulation is achieved by applying a time varying high voltage which satisfies a proper modulation and demodulation algorithm as explained as follows. Writing Equation (4.16) simply as

$$\phi = \phi_0 + \phi_1 \sin \Omega t \equiv \phi_0 + \phi_m. \tag{4.64}$$

Then the measured signal (interferogram) can be written as

$$S = \frac{I_0}{2}[1 + \zeta \cos(\phi_0 + \phi_m)] \tag{4.65}$$

For a drifting plasma in local thermodynamic equilibrium, the zero moment (brightness, I_0) is given by the average signal level, the first moment (phase shift, ϕ_0) by the interferomatric phase which gives the flow speed, and the second moment (contrast, ζ) by the fringe visibility which gives an ion temperature.

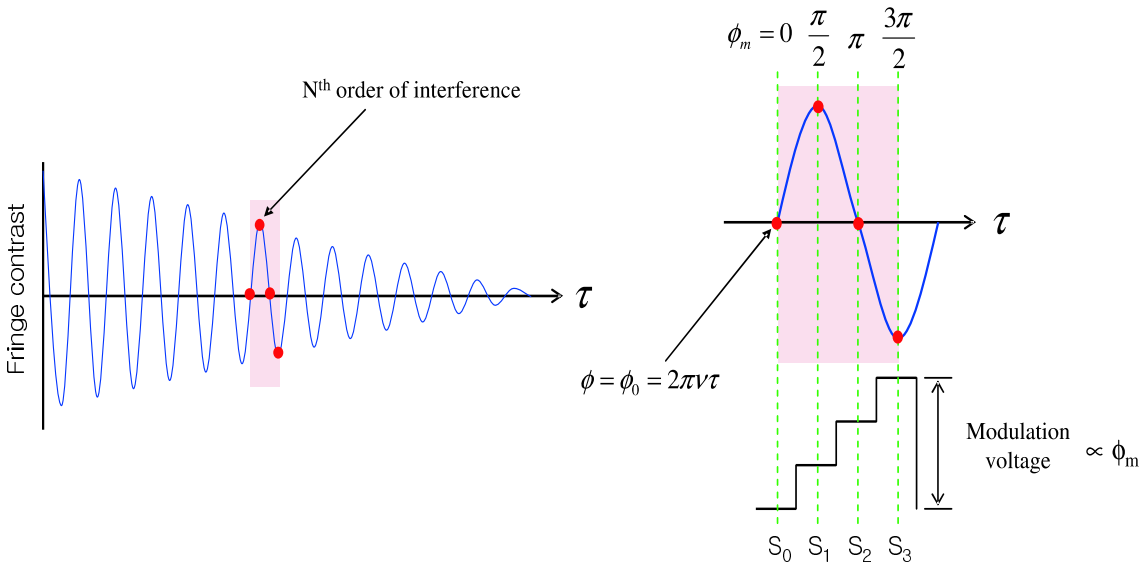

Figure 4.9: The *4-frame* Electro-Optic modulation for the MOSS spectrometer.

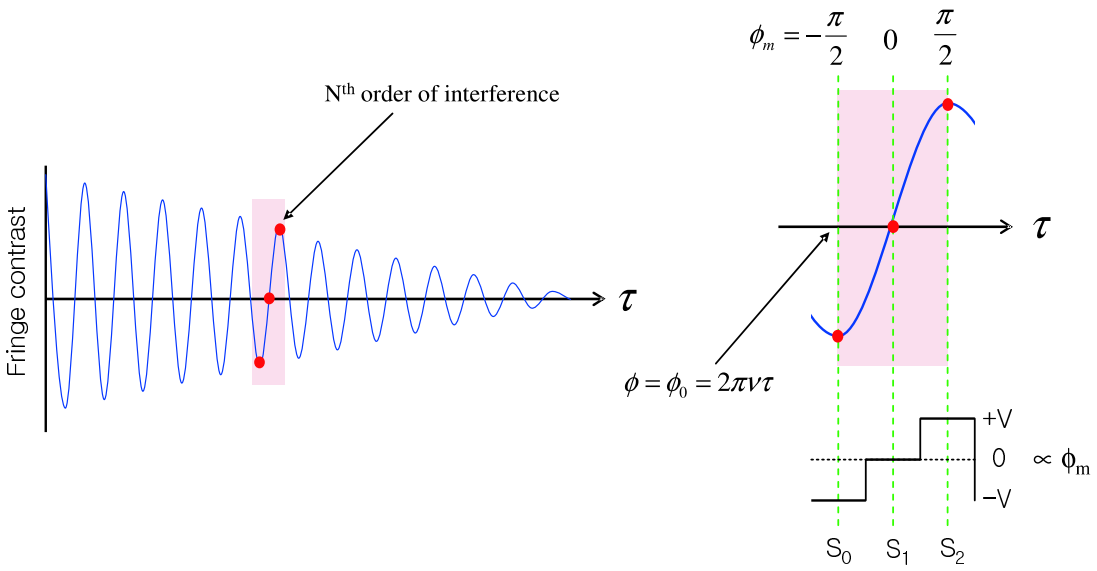

Figure 4.10: The *3-frame* Electro-Optic modulation for the MOSS spectrometer. This modulation improves the system performance by 25% compared to the system using the *4-frame* modulation.

Figure 4.9 explains the *4-frame* ($\phi_m = 0, \pi/2, \pi, 3\pi/2$) electro-optic phase modu-

lation scheme. When there is no modulation voltage ($\phi_m = 0$), then the MOSS signal starts from the N^{th} order of interference that is freely chosen by the thickness of the birefringence (delay) plate. As the modulation voltage is increased in steps proportional to the modulation phase $\phi_m = 0, \pi/2, \pi, 3\pi/2$, the MOSS signals are modulated into S_0, S_1, S_2, and S_3 respectively.
The *3-frame* ($\phi_m = -\pi/2, 0, 3\pi/2$) electro-optic phase modulation scheme is illustrated in Figure 4.10. In this case, as the modulation voltage is increased from -V to +V in steps proportional to the modulation phase, the MOSS signals are modulated into S_0, S_1, and S_2. Since the reduced modulation uses only three frames there is less possibility of electrical errors and it improves the absolute time resolution by 25% compared to the system using the 4-frame modulation.

4.7.2 Demodulation algorithm for the 4-frame phase modulation

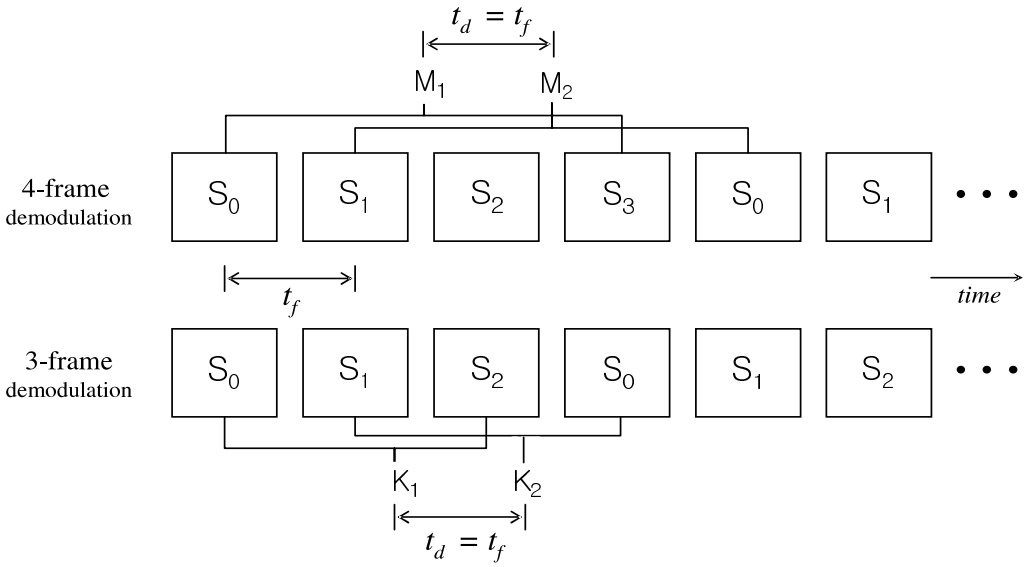

Figure 4.11: Comparison of the 4- and 3-frame demodulation sequences

The process of extracting the information from the modulated signal is called demodulation. The measured signal S is given by equation (4.65) where there are three unknown parameters, I_0, ζ, and ϕ_0. The four signal equations at each modulation phase are shown below:

$$\phi_m = 0,\ S_0 = \tfrac{I_0}{2}(1 + \zeta \cos\phi_0) \tag{4.66}$$

$$\phi_m = \pi/2,\ S_1 = \tfrac{I_0}{2}(1 - \zeta \sin\phi_0) \tag{4.67}$$

$$\phi_m = \pi,\ S_2 = \tfrac{I_0}{2}(1 - \zeta \cos\phi_0) \tag{4.68}$$

$$\phi_m = 3\pi/2,\ S_3 = \tfrac{I_0}{2}(1 + \zeta \sin\phi_0) \tag{4.69}$$

These equations can be reduced to their simplest forms by adding and subtracting them as shown below:

$$S_0 + S_2 = I_0 \equiv I_1 \tag{4.70}$$

$$S_1 + S_3 = I_0 \equiv I_2 \tag{4.71}$$

$$S_0 - S_2 = I_0 \zeta \cos\phi_0 \equiv \zeta_c \tag{4.72}$$

$$S_3 - S_1 = I_0 \zeta \sin\phi_0 \equiv \zeta_s \tag{4.73}$$

Then the three parameters are

$$\frac{I_1 + I_2}{2} = I_0 \tag{4.74}$$

$$\tan^{-1}\left(\frac{\zeta_s}{\zeta_c}\right) = \phi_0 \tag{4.75}$$

and

$$\frac{\sqrt{\zeta_c^2 + \zeta_s^2}}{I_0} = \zeta \tag{4.76}$$

where I_0 is the brightness of the plasma, ϕ_0 is the phase shift, and ζ is the contrast. After calibration of the system the measured contrast ζ is given by multiplying the instrument contrast ζ_I by the plasma contrast ζ_S

$$\zeta = \zeta_I \zeta_S = \exp\left(-\frac{T_S}{T_C}\right). \tag{4.77}$$

This will give the absolute ion temperature of the emitting species. Here T_S is the plasma temperature of the emitting species, and T_C is the characteristic temperature of the system which is determined by the thickness of a delay plate. The plasma temperature can be written as

$$T_S = -T_C \ln\left(\frac{\zeta}{\zeta_I}\right) \tag{4.78}$$

The calibration is done for the entire MOSS measurement (see Figure 4.8) using a spectral lamp instead of a plasma as a source.
Since a 2D CCD is used as a detector, the result is a 2D distribution of the parameters for a viewing area. Figure 4.11 explains the demodulation sequences of 4- and 3-frame modulations in which t_f is the time interval between two frames (a reciprocal of the CCD frame rate in Hz), and t_d is the demodulation time interval. For the 4-frame modulation, the first 4 frames from S_0 are used for the first demodulation, and the next 4 frames from S_1 are used for the second demodulation as shown in the figure. Since the time interval of the demodulation depends on the frame rate of the CCD camera, the maximum time resolution is limited by the frame interval, t_f. If $4 \times t_f$ is shorter than the time scale variation of plasma parameters, or the variation can be ignored in the time interval, then the time resolution of the system is equal to the frame rate of the CCD camera. Although the 3-frame modulation

provides better absolute time resolution, the sequential time resolution (t_d) of the two modulation schemes is the same.

4.7.3 Demodulation algorithm for the 3-frame modulation

The 3-frame demodulation includes a calibration procedure which is carried out by modulating a narrow calibration spectral line with a homogeneous light surface before or after experiments. The measured signal S in Equation (4.65) can therefore be written as

$$S = \frac{I_0}{2}\left[1 + \zeta_I \zeta \cos\left(\phi_I + \phi_0 + \phi_m\right)\right] \tag{4.79}$$

where ζ_I and ϕ_I are the contrast and phase induced by the instrument itself. Possible causes of the instrument function have been discussed in Section 4.6. The modulation phase ϕ_m of the three frames are $-\frac{\pi}{2}$, 0, and $\frac{\pi}{2}$, and the light intensity I_0, contrast ζ, and phase ϕ_0 are parameters which will be evaluated by this demodulation algorithm. Equation (4.79) can be rewritten as

$$\begin{aligned} S &= \frac{I_0}{2}\left[1 + \zeta_I \zeta \cos\phi_0 \cos\left(\phi_I + \phi_m\right) - \zeta_I \zeta \sin\phi_0 \sin\left(\phi_I + \phi_m\right)\right] \\ &= \frac{I_0}{2}\left(1 + \alpha\zeta_c - \beta\zeta_s\right) \end{aligned} \tag{4.80}$$

where $\alpha \equiv \zeta_I \cos(\phi_I + \phi_m)$, $\beta \equiv \zeta_I \sin(\phi_I + \phi_m)$, $\zeta_c \equiv \zeta \cos\phi_0$, and $\zeta_s \equiv \zeta \sin\phi_0$. For the n-th image frame Equation (4.80) can also be written as

$$S_n = \frac{I_0}{2}\left(1 + \alpha_n\zeta_c - \beta_n\zeta_s\right) \tag{4.81}$$

then the three modulated signals at each modulation phase are

$$S_0 = \frac{I_0}{2}\left(1 + \alpha_0\zeta_c - \beta_0\zeta_s\right) \tag{4.82}$$

$$S_1 = \frac{I_0}{2}\left(1 + \alpha_1\zeta_c - \beta_1\zeta_s\right) \tag{4.83}$$

$$S_2 = \frac{I_0}{2}\left(1 + \alpha_2\zeta_c - \beta_2\zeta_s\right) \tag{4.84}$$

where $\alpha_0 = \beta_1 = \alpha_2$ and $\alpha_1 = \beta_2 = -\beta_0$ because of the phase modulation. Now, to solve the unknown parameters, I_0, ϕ_0, and ζ we define

$$\begin{aligned} S_\alpha &\equiv (\alpha_2 - \alpha_1)(S_1 - S_0) - (\alpha_1 - \alpha_0)(S_2 - S_1) \\ &= I_0(\alpha_1\beta_2 + \alpha_2\beta_0)\zeta_s \\ &\equiv I_0\delta\zeta_s \end{aligned} \tag{4.85}$$

and

$$\begin{aligned} S_\beta &\equiv (\beta_2-\beta_1)(S_1-S_0)-(\beta_1-\beta_0)(S_2-S_1) \\ &= I_0(\alpha_1\beta_2+\alpha_2\beta_0)\zeta_c \\ &\equiv I_0\delta\zeta_c \end{aligned} \tag{4.86}$$

where

$$\begin{aligned} \delta &\equiv \frac{1}{2}\left[(\alpha_1-\alpha_0)(\beta_2-\beta_1)-(\alpha_2-\alpha_1)(\beta_1-\beta_0)\right] \\ &= \alpha_1\beta_2+\alpha_2\beta_0. \end{aligned} \tag{4.87}$$

Then the three desired parameters are

$$I_0 = \frac{1}{3}\left(2\cdot\Sigma S_n - \frac{\Sigma\alpha_n\cdot S_\alpha - \Sigma\beta_n\cdot S_\beta}{\delta}\right) \tag{4.88}$$

$$\phi_0 = \tan^{-1}\left(\frac{S_\alpha}{S_\beta}\right) = \tan^{-1}\left(\frac{\zeta_s}{\zeta_c}\right) \tag{4.89}$$

and

$$\zeta = \frac{\sqrt{S_\alpha^2+S_\beta^2}}{\delta\cdot I_0} = \sqrt{\zeta_c+\zeta_s}. \tag{4.90}$$

Here the phase ϕ_0 is in radians, and the ion temperature is in eV for the characteristic temperature T_c of the emitting species and is given by $T_i = -T_c\cdot\ln\zeta$.

4.8 Experimental apparatus

In the previous sections we discussed the principle of the MOSS spectrometer and the function of components of the MOSS optics. In this section the hardware used in the MOSS spectrometer and its complete setup are introduced. A schematic illustrating the hardware and system setup is shown in Figure 4.12. The part enclosed by a dotted line in the top right hand corner of the figure represents the control room, and the part surrounded by a dotted line at the bottom of the figure describes the MOSS spectrometer with its calibration system. The other parts of the figure show the various power and control systems and the arrows mark important data and control signal flow directions. Figure 4.12 shows that the system is started by an external trigger ($+2.5-5$ V DC) pulse which is relayed by the interface board to the PC which controls the CCD camera. The CCD camera is then running at a pre-set frame rate and it also provides the trigger signal for each frame to the interface board which controls the AC power amplifier of the electro-optic components of the MOSS spectrometer. The control board serves as a data acquisition interface, and the control computer as the data storage and data signal processor. The whole

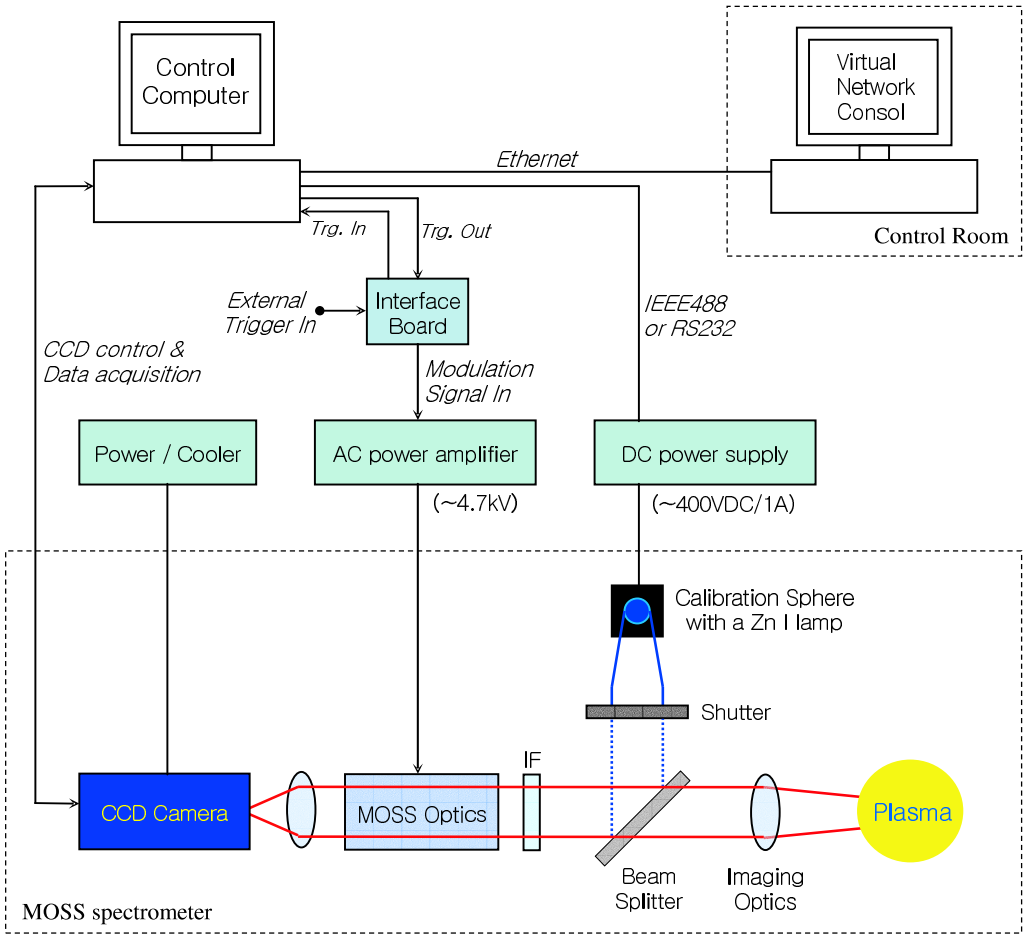

Figure 4.12: Schematic layout of the complete MOSS spectrometer system

system can be controlled through a virtual network console from a remote control area since the console is connected via the local area network (LAN) to the control computer. If the LAN to which the control computer is connected allows internet access to the client then the control room can be anywhere.

4.8.1 CCD camera

A 12-bit high quantum efficiency CCD (Charge Coupled Device) camera is used as a 2D detector array for the MOSS spectrometer. The specifications of the CCD camera are tabulated in Table 4.1. The CCD camera has a 12-bit ADC (Analog to Digital Converter). When the ADC translates the electrical impulses into digital numerical data, the values are stored as a simple binary code. A 12-bit ADC produces a monochrome digital image that contains 4,096 ($=2^{12}$) distinct shades of gray. Having 12 bits of information allows us to accurately measure the signal.
The CCD camera has a quantum efficiency of 65% at 500 nm. The quantum efficiency is the ratio of the number of detected electrons divided by the product of the number of incident photons times the number of electrons that each photon can be expected to generate.

Table 4.1: Specifications of the CCD camera used for the MOSS spectrometer

Model	PCO SensiCam QE
Number of Pixels	1376(H) × 1040(V)
Pixel Size	6.45μm × 6.45μm
Spectral Response	280 nm − 1000 nm
Quantum Efficiency at 500 nm	65%
Binning Horizontal	1, 2, 4, 8
Binning Vertical	1, 2, 4, 8, 16, 32
Frame rate	10 Hz at full frame
	75.33 Hz at binning 8 by 16
A/D converter	12 Bit
A/D conversion factor	$2e^-$/count (Gain High)
	$4e^-$/count (Gain Low)
Camera Dimension	93(W) × 78(H) × 210(L) mm
Optical input	C-Mount

The maximum resolution of the CCD camera is 1376 × 1024 pixels in the full frame mode, and it provides a maximum frame rate of 75.33 Hz in the 8 × 16 binning mode (164 × 64 pixels).

4.8.2 High voltage modulation system

The modulation phase ϕ_m is produced by applying a high voltage to the crystal plates. In order to use the electro-optic modulation schemes, the stair-step high voltage wave is needed as illustrated in Figures 4.9 and 4.10. The high-voltage modulation of the electro-optic plates is achieved with a high voltage power amplifier with a 4- or 3-frame synchronous external clock produced by a PC based control card and its operation software. The external clock is determined by the frame rate of the CCD camera.

4.8.3 Calibration system

The part shown in the dotted line at the bottom of Figure 4.12 shows a schematic of the MOSS spectrometer with a calibration system. The light sources are introduced to the MOSS spectrometer from both the plasma and the calibration light sources. The Zn I line at 468.0 nm is used for the calibration of the system which is designed for measuring the He II line. It illuminates the integrating sphere which thus provides a homogeneous light source (50 mm in diameter). In order to avoid the electric power source fluctuation of 50/60 Hz or its harmonics, the spectral lamp uses a remote controlled DC power supply. The ignition voltage of the Zn I spectral lamp (Osram Zn/10) is around 400 VDC, and the operation power after stabilization

is about 17 W (17 VDC·1 A). The remote control board for the IEEE488 or RS232 interface of the DC power supply is also used to control an electrical light shutter so that the calibration can be repeated between WEGA discharges without having to switch off the spectral lamp.

5

Testing a prototype 2D MOSS spectrometer in W7-AS stellarator

A novel divertor concept called the *Island Divertor*, which has been explored in the Wendelstein 7-AS stellarator (W7-AS), is inherently asymmetrical in the poloidal and toroidal directions. Since the divertor concept in stellarators has a fully 3-dimensional structure (a poloidal cut at one toroidal location is shown in Figure 5.1) the plasma parameters also vary in 3-dimensions. To explore the complicated 3D physics, many 2-dimensional spectroscopy-based diagnostics were installed to observe the W7-AS divertor region [43]. A prototype MOSS spectrometer was one

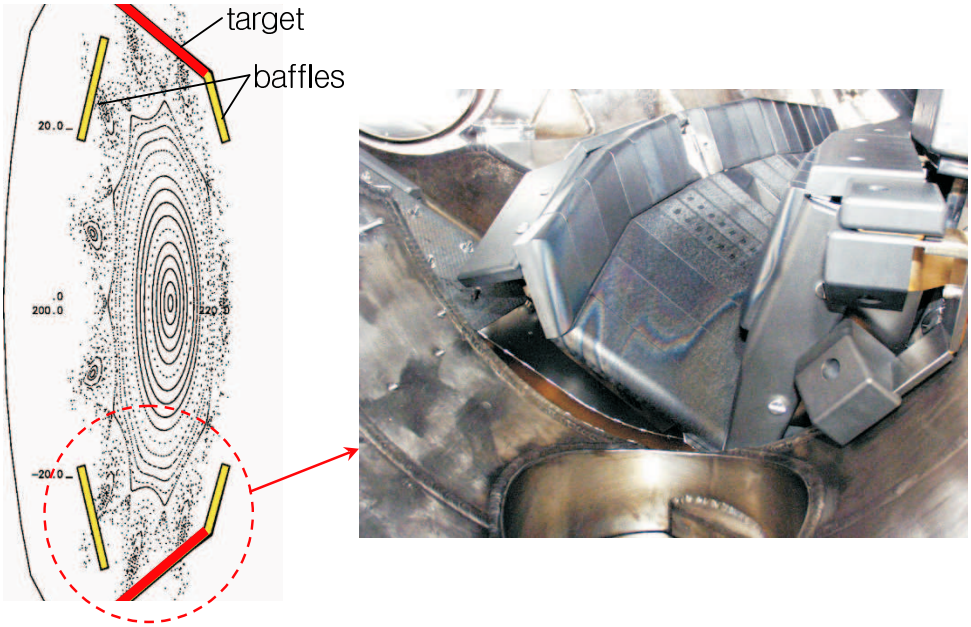

Figure 5.1: The island divertor in W7-AS has a complicated 3D structure.

of those diagnostics. It was also the first 2D imaging MOSS spectrometer. It used a high-resolution 2D CCD camera to study the 468.6 nm He II line emissions from the divertor region in W7-AS. The main issue was to test the suitability of such a system as a possible future W7-X divertor diagnostic. The measurement was performed at the very end of the final W7-AS experimental campaign.

In this chapter the first 2D MOSS spectrometer for W7-AS using a 2D CCD camera is described. It concludes with a summary of the first test measurements.

5.1 The W7-AS Stellarator

The Wendelstein 7-AS stellarator experiment, which was operated at the Max-Planck-Institut für Plasmaphysik (IPP) in Garching from 1988 to 2002, belonged to the generation of *advanced* stellarators. A photograph of the W7-AS stellarator is shown in Figure 5.2.

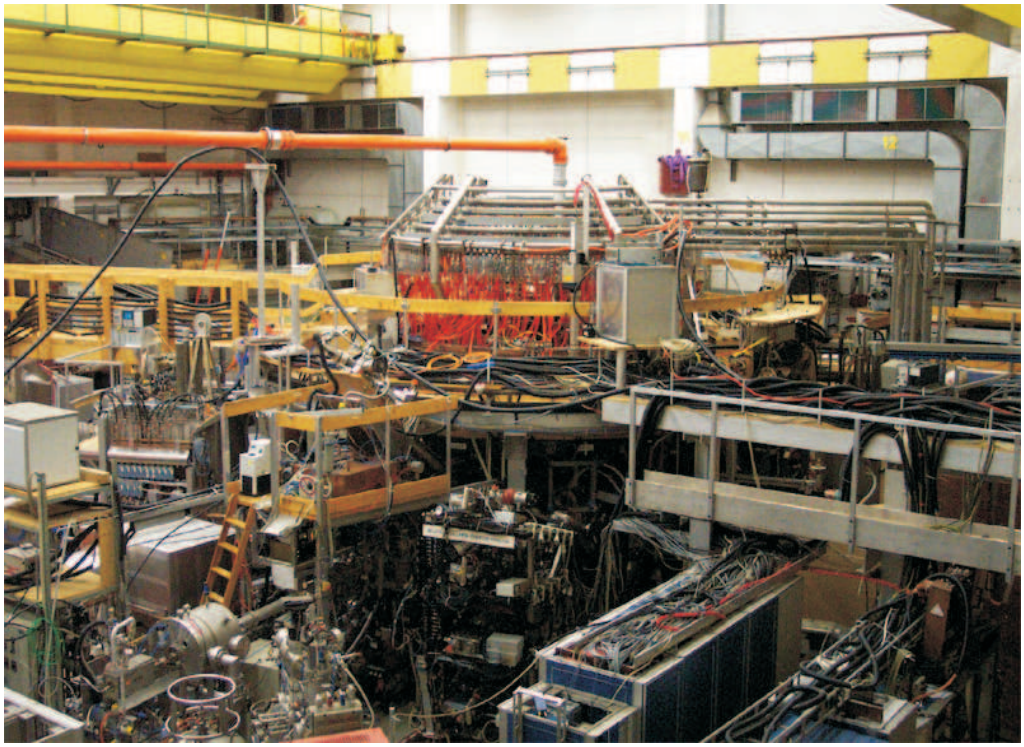

Figure 5.2: Photograph of the W7-AS stellarator.

W7-AS is distinguished from classical stellarators by its physically optimized magnetic field generated by the 3D-shaped modular coils [41]. W7-AS is a modular stellarator with five magnetic field periods and modular field coils. The major and minor radii are $R = 2.0\,\mathrm{m}$ and $r = 0.2\,\mathrm{m}$, respectively. The magnetic field strength on axis is $B \leq 2.5\,\mathrm{T}$. The rotational transform ι can be varied between 0.25 and 0.7 by currents in a set of toroidal field coils. The magnetic field structure varies as a function of the toroidal angle φ. Within each period the plasma cross section varies from triangular ($\varphi = 0°$) to elliptical ($\varphi = 36°$) and back to triangular again. Figure 5.3 illustrates the field structure [42].
W7-AS was the first stellarator to be equipped with an island divertor. The 10 island divertor modules, five at the top and five at the bottom, were installed in summer 2000, and the experimental program started in March 2001.

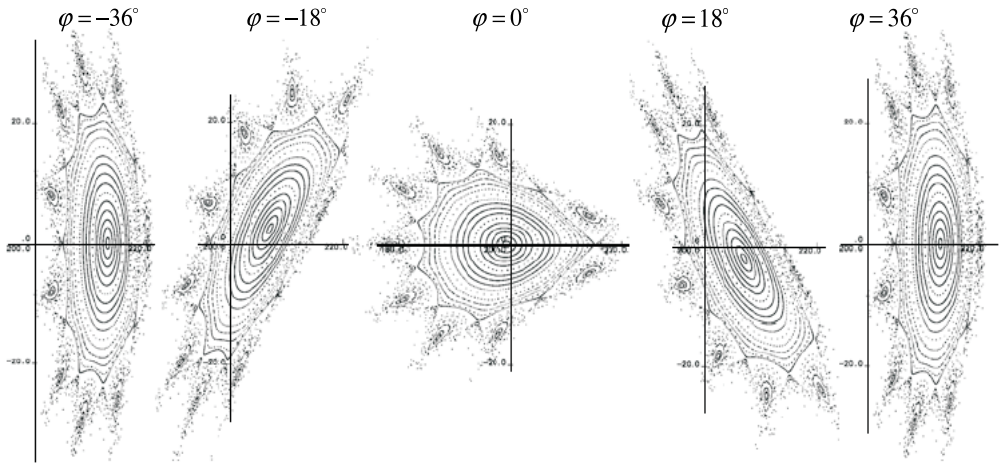

Figure 5.3: Flux surfaces at five toroidal angles showing one of five magnetic field periods. $\varphi = 0°$ is the triangular plane in the center of a module, $\varphi = 18°$ is intermediate and $\varphi = 36°$ is where two modules meet. The corresponding negative angle flux surfaces are obtained by horizontal mirroring.

In W7-AS there are three kinds of heating systems; 2.4 MW electron cyclotron resonance heating (ECRH) and 2.8 MW neutral beam injection (NBI) as well as 1.0 MW ion cyclotron resonance heating (ICRH).

5.2 The MOSS spectrometer in W7-AS

As mentioned in the beginning of this chapter, many 2D spectroscopy-based diagnostics were installed in the W7-AS divertor region to study the complicated 3D island divertor physics. A newly constructed MOSS spectrometer was also one of those diagnostics. We have used a high-resolution 2D CCD camera as a MOSS detector array. This is the first 2D imaging MOSS spectrometer. The CCD camera is very sensitive to weak light and easy to focus using a commercial camera lens. If the plasma pulse is sufficiently long and stable, then using the 2D CCD camera is potentially one of the most powerful ways to study the complicated structures in island divertor physics.

Figure 5.4 illustrates the optical layout of the MOSS spectrometer on W7-AS, in which a 50 mm C-mount lens was used as a collimation lens. An interference filter at 468.9 nm with 1.0 nm bandwidth transmits the He II line emission at 468.6 nm. The delay plate is a Lithium niobate crystal of 7.5 mm thickness, corresponding to a characteristic temperature of $T_C = 30\,\text{eV}$. Figure 5.5 illustrates the schematic layout of the MOSS spectrometer on the W7-AS stellarator, and the photograph in Figure 5.6 shows the MOSS spectrometer installed in the H-α box looking at an entire upper divertor module. The light from the divertor plasma is transmitted by a coherent fiber bundle to the different camera system in the box. The MOSS spectrometer gets 50% of the light from the plasma via the first beam splitter. The

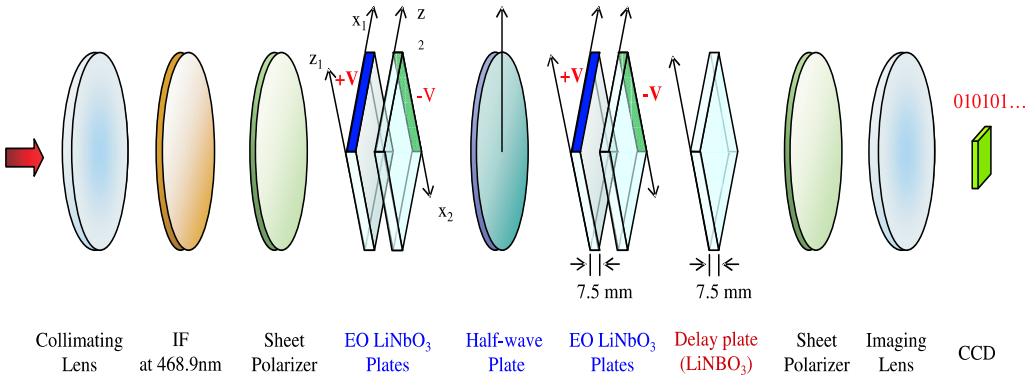

Figure 5.4: Optical layout of the MOSS spectrometer in W7-AS. The interference filter must be placed before the first sheet polarizer.

modulation frequency can be freely chosen, but the maximum frequency is limited to 75.33 Hz by the CCD camera maximum frame rate at 164 by 64 pixels binning mode. The 4-frame modulation was used for the experiment on W7-AS.

5.3 Results and discussion

To construct a 2D MOSS spectrometer for the 3-dimensional divertor plasma, a MOSS coherence numerical simulation code was created as discussed in Chapter 3. For two spectral lines (He II line at 468.6 nm and C III line at 468.9 nm shown in Figure 3.4) which are typically emitted in the W7-AS divertor, a simulation model was developed under the assumption that Doppler broadening is the dominant broadening mechanism. This assumption was experimentally verified for the case of the He II line at 468.6 nm. Doppler broadening was found to be significantly higher than the other broadening mechanisms such as Stark broadening and Zeeman splitting for the experimental conditions of the W7-AS divertor plasmas.
The first 2D MOSS spectrometer was constructed to study the 468.6 nm He II line emissions from the divertor region in W7-AS. To test the suitability of such a system as a possible W7-X divertor diagnostic, the first measurements were undertaken on W7-AS at the very end of its last experimental campaign. Since the MOSS spectrometer was under development the experiment focused on testing the spectrometer rather than plasma physics investigations. From the experiments two important problems were identified and these were subsequently settled during experiments on the WEGA stellarator.
Figure 5.7 shows the first results from the 4-frame demodulation code. The modulated image changes brightness because we are looking at different points on the interferogram as illustrated in the 4-frame modulation scheme in Figure 4.9. However, its demodulated images show unexpected results.
Firstly, only the light intensity is acceptable among the three demodulated parameters. This is due to an incorrect optical arrangement. Since the heart of the system

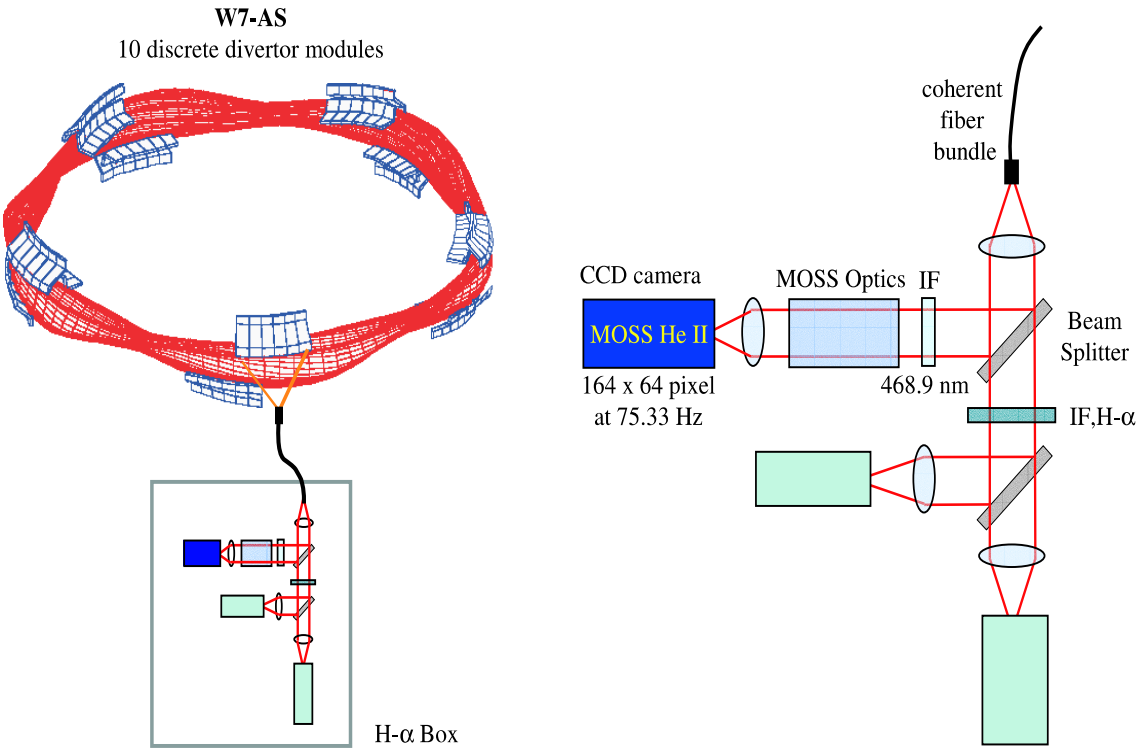

Figure 5.5: Schematic layout of the MOSS spectrometer in W7-AS. The spectrometer is contained in an H-α box which is connected to one divertor module.

is the electro-optic modulator and delay plate, it was assumed that the interference filter does not contribute to any polarization state. The interference filter was therefore placed next to the second sheet polarizer to protect the fragile polished filter surface, but this assumption was incorrect regarding the *isolated* line modulation. This situation can be explained in the following way: The phase and contrast at the designed interference number ($N = 2424$ for a Lithium niobate delay plate of 7.5 mm thickness) of the He II line at 468.6 nm cannot be resolved any further because all of the emitting spectrum was modulated and interfered together before filtering the He II line. This is a similar situation to where many spectra having a different frequency or wavelength have Fourier transformed together and mixed into a single waveform in the time domain. In principle, this can be filtered for a desired band-pass but the modification, by means of the harmonics or aliasing, cannot be recovered easily. Also, the optical filter for the frequency domain cannot be used for the time domain. This is why the image shows incorrect results, even though the incoming light was properly modulated and demodulated.

Secondly, the images are blurred compared to the well focused H-α images taken with the other cameras in the H-α box (Figure 5.8) which share the same coherent fiber bundle as shown in Figure 5.5. The reason that the images are blurred is mainly a focusing problem. After shutting down W7-AS, the focusing was improved by shining a white light inside the vessel. Figure 5.9 shows the images of our target divertor module before and after the improvement.

Although the results are not satisfactory, most of the theoretical study discussed

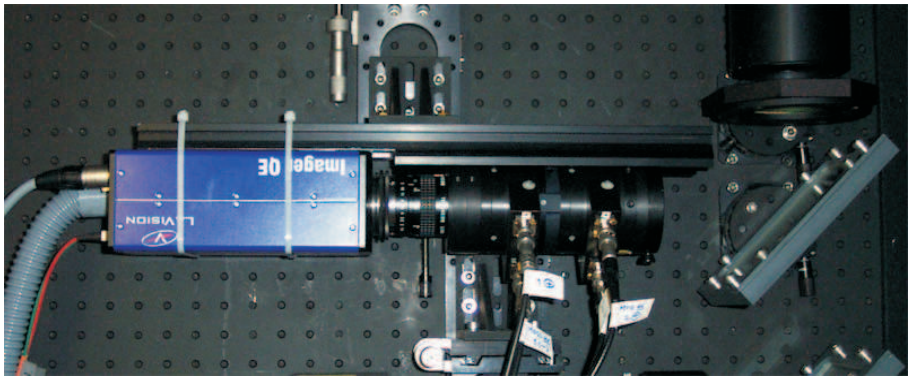

Figure 5.6: First 2D MOSS spectrometer installed in the H-α box looking at an entire upper divertor module.

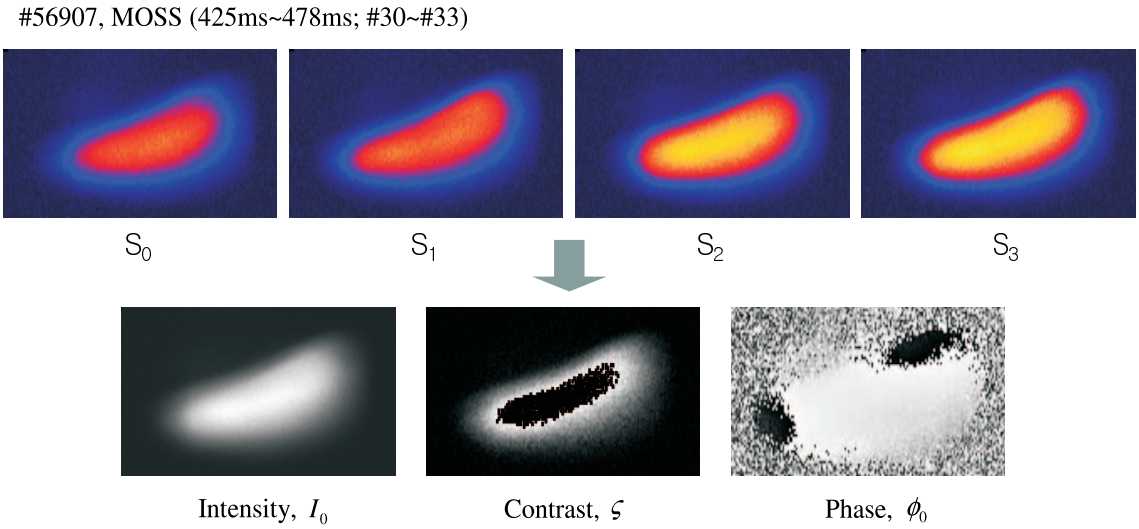

Figure 5.7: First results from the 4-frame demodulation code. Modulated images, S_0, S_1, S_2, and S_3, change brightness because of the phase modulation.

in the previous chapters was carried out during the construction of the prototype MOSS spectrometer in W7-AS, and the problems and solutions found during the first experiments provided important experience to finish the development. The improved MOSS spectrometer using a Lithium tantalite electro-optic modulator with a 3-frame demodulation algorithm including the absolute calibration procedure was installed on the WEGA stellarator. Plasma physics investigations using the MOSS spectrometer in WEGA are discussed in the next chapter.

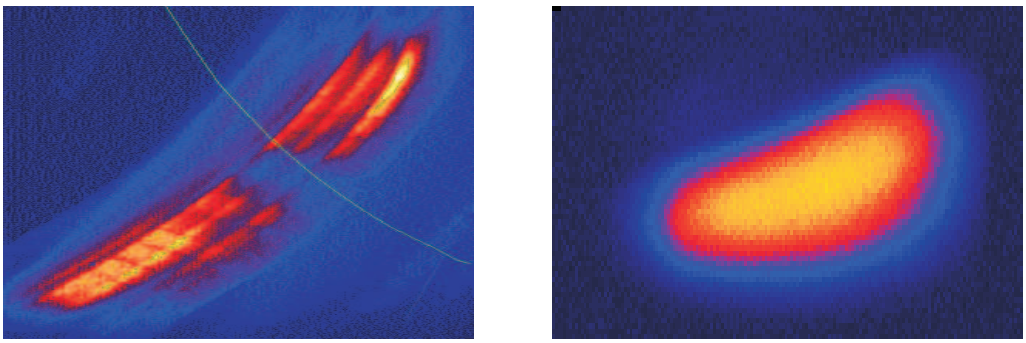

Figure 5.8: 2D images of Hα (left) recorded by a CCD camera and He II (right) recorded by the MOSS at 560 ms of W7-AS discharge number 56907. The reason for the blurring of the He II image was a focusing problem.

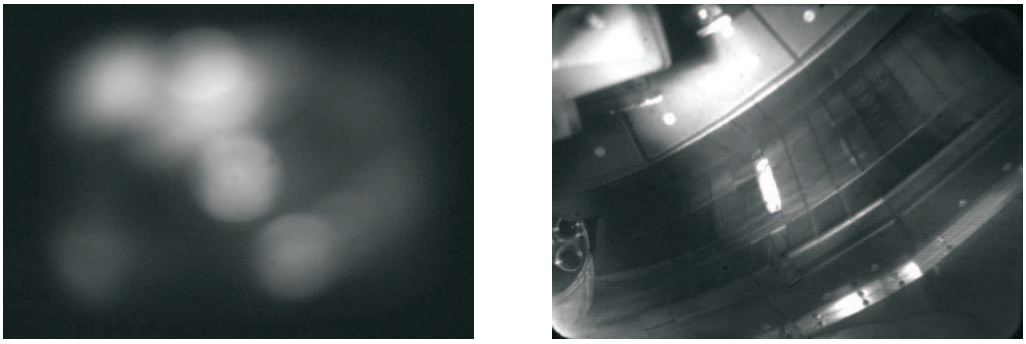

Figure 5.9: Images of a target divertor module before (left) and after (right) improving the focusing and viewing area.

6

Experimental setup in WEGA

A prototype 2D MOSS spectrometer was tested during the end of the W7-AS experimental campaign and was discussed in the previous chapter. After the experimental campaign, the MOSS spectrometer was greatly improved. Firstly, a calibration system for 2D imaging was constructed which provided absolute values of temperature with the 3-frame modulation including the calibration procedure. Secondly, to reduce the instrument effect induced by natural birefringence of the electro-optic modulator, the Lithium niobate modulator was replaced by a Lithium tantalate crystal. Its natural birefringence is about 10% of the Lithium niobate. Finally, an optical housing for the MOSS system having good flexibility, called a MOSS box, was constructed. The MOSS box includes the calibration system and it relays the incoming light source to the other diagnostic. The desired imaging area can be achieved by replacing the imaging modules in front of the box.
The improved MOSS spectrometer was installed in the WEGA stellarator to study a relatively low temperature ($T_i < 3\,\mathrm{eV}$) plasma. Although the MOSS system is intended for high temperature plasma measurements, experiments in the WEGA stellarator provided an excellent opportunity to prove the system performance for the diagnostic development since very high resolution and efficiency are required to study low temperature plasmas. The results were crosschecked with an Echelle grating spectrometer installed together with the MOSS system. It was the first ion temperature study in the WEGA stellarator.

6.1 The WEGA Stellarator

The WEGA (Wendelstein Experiment in Greifswald zur Ausbildung) is an ECR heated classical stellarator located at IPP-Greifswald which is used for educational training and new diagnostic developments for W7-X. A photograph of the WEGA stellarator is shown in Figure 6.1. The stellarator was originally built by IPP Garching and the Commissariat à l'Energie Atomique in Grenoble (France). The device was used as an ohmically heated tokamak in the 1970s. It was finally moved from the Institut für Plasmaforschung, Stuttgart to Greifswald in the year 2000 and

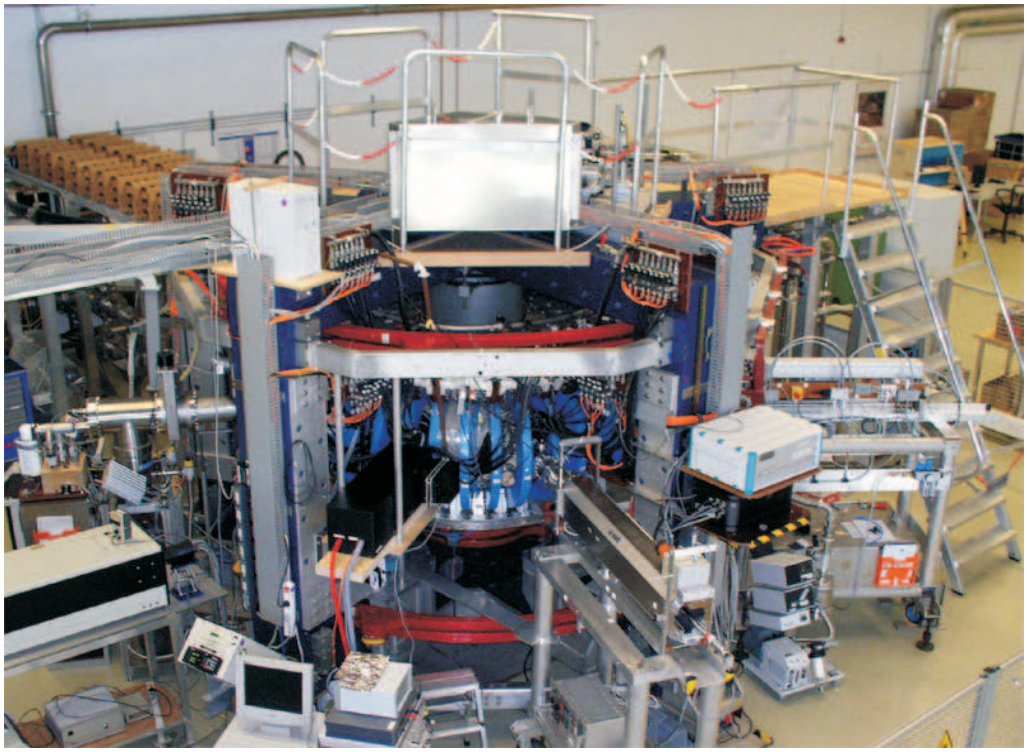

Figure 6.1: Photograph of the WEGA stellarator.

the first stellarator plasma was created in 2001. The coil geometry is illustrated in Figure 6.2. There are 40 toroidal field coils, and 4 helical packages (14 conductors on each package) are mounted with period $l = 2$ and $m = 5$ on the vacuum vessel which has a major radius of 0.72 m and a minor radius of 0.19 m. The helical conductors of the 4 winding packages are connected in a series circuit and the currents in adjacent helical windings flow in opposite directions to avoid inducing a vertical magnetic field. Additionally, WEGA has vertical field coils in a Helmholtz configuration which are used to shift the plasma radially for configurational flexibility. Figure 6.3 shows the rotational transform and shear of a magnetic configuration with and

Table 6.1: Machine parameters of the WEGA stellarator

Parameter	Value
Major radius	$R = 0.72\,\mathrm{m}$
Minor radius	$r = 0.19\,\mathrm{m}$
Plasma radius	$a \sim 10\,\mathrm{cm}$
Magnetic field coils	40 toroidal and 4 helical coils
Magnetic field	$B = 87.5\,\mathrm{mT}$, $B_0^{max} = 340\,\mathrm{mT}$
ECR power	$P_{mw} = 6\,\mathrm{kW} + 20\,\mathrm{kW}$ at $2.45\,\mathrm{GHz}$
Electron density	$10^8 - 10^9\,\mathrm{m}^{-3}$
Electron temperature	$5 - 10\,\mathrm{eV}$
Working gases	H_2, He, Ar

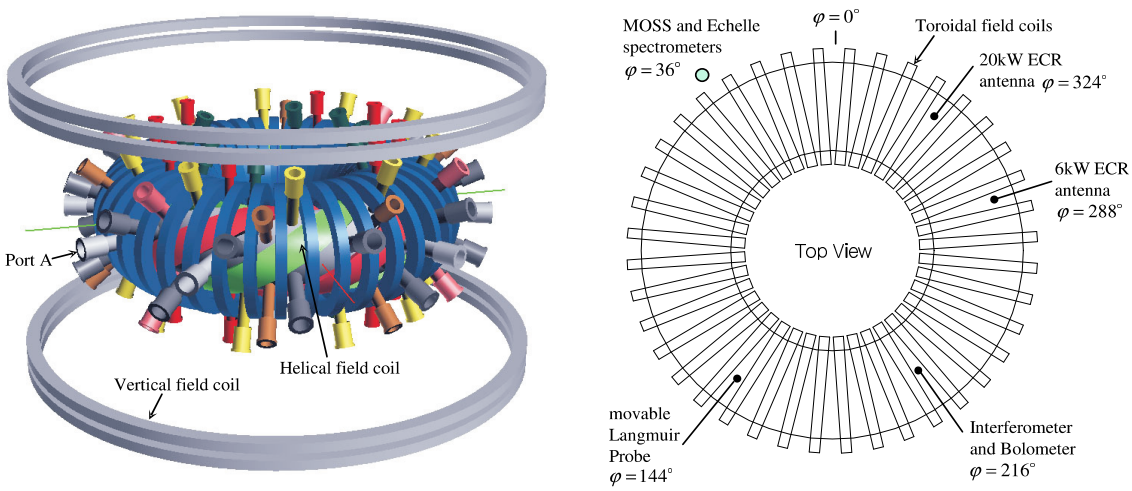

Figure 6.2: Illustrations of the magnetic field coils and port configurations. A top view image on the right shows the positions of ECR antenna and diagnostics. The MOSS spectrometer is installed on a port A at $\varphi = 36°$.

without a vertical field [49]. By increasing the vertical field the rotational transform is increased while the shear is lowered. With the help of the vertical field coils it is now possible to operate WEGA in magnetic configurations which avoid low order rational resonances. The toroidal magnetic field B_{Tor} and rotational transform ι for WEGA are given by [44]

$$B_{Tor} = 0.114 \cdot I_{Tor} \tag{6.1}$$

$$\iota \approx 0.0972(I_{HX}/I_{Tor})^2 \tag{6.2}$$

where I_{Tor} is the toroidal current and I_{HX} is the helical current in kA. The vertical field coils can shift the magnetic axis as much as 2 cm and change the plasma radius or rotational transform. The rotational transform can be varied between 0.1 and 1.0 by changing the coil currents flowing in these coils. The stellarator can produce a steady state plasma for up to 30 minutes using a 6 kW and a 20 kW microwave magnetron at 2.45 GHz. The overall parameters of the stellarator are shown in Table 6.1.

6.2 Experimental setup

In this section, the specifications and features of the MOSS spectrometer and Echelle grating spectrometer in WEGA are described. The viewing port of WEGA is very restricted for 2D imaging because of the coil arrangement but this was overcome by means of a special imaging optic. The MOSS spectrometer observes a 25 cm × 25 cm image plane and the viewing area covers a toroidal section of $\varphi = 20°$. The poloidal coverage is dependent on the value of the rotational transform, ι. The Echelle grating spectrometer uses a 1D fiber array to observe a slice of the viewing area of the MOSS spectrometer. The details are discussed in the following sections.

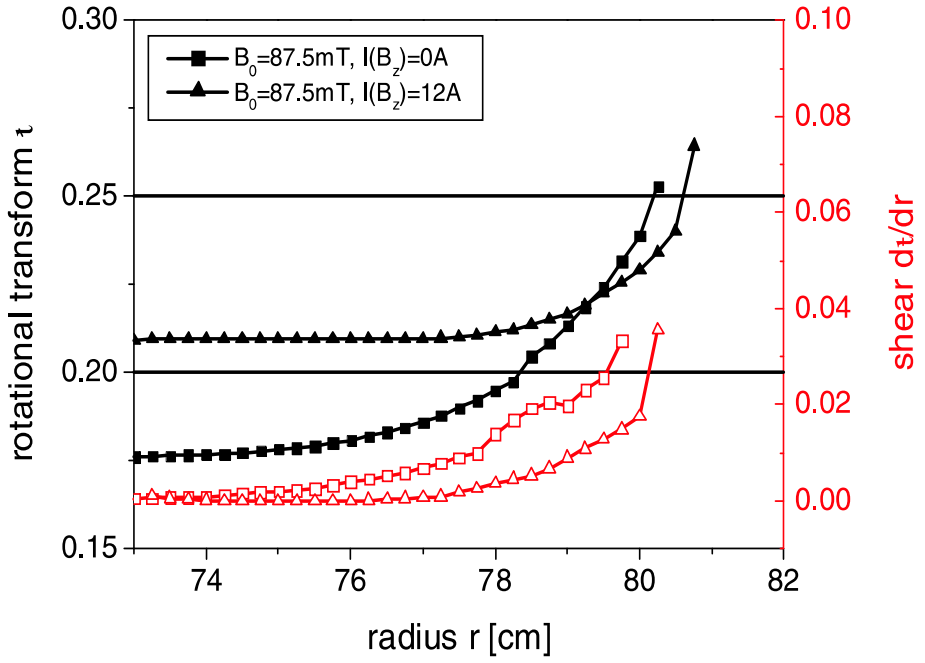

Figure 6.3: Rotational transform and shear of a magnetic configuration with and without vertical field.

6.2.1 MOSS spectrometer

A greatly improved MOSS spectrometer was installed in the WEGA stellarator. As briefly introduced in the beginning of this chapter, this version of the MOSS spectrometer uses two y-cut Lithium tantalate crystals, each of 10 mm thickness, as a modulator. The half-wave voltage V_π (see Equation 4.49) of the modulator is 4.13 kV. Figure 6.4 illustrates the optical layout of the MOSS setup on WEGA.

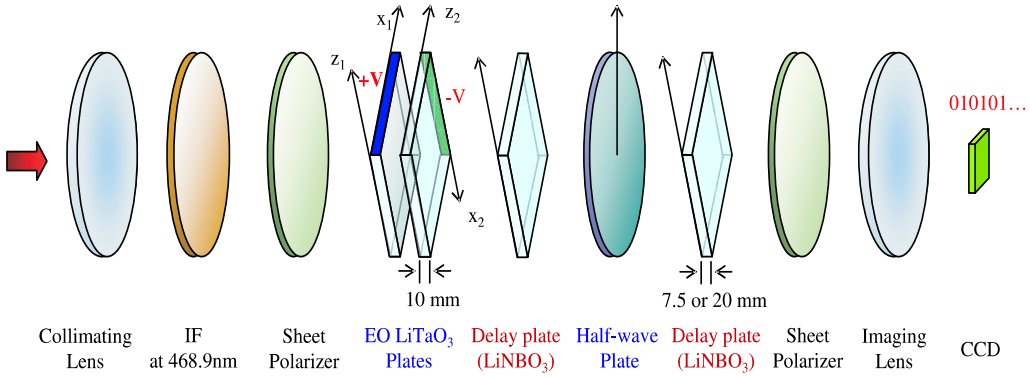

Figure 6.4: Optical layout of the MOSS spectrometer on the WEGA.

In order to adapt the system to low temperature plasmas in WEGA thicker delay plates are used. We had the flexibility to realize further delay configurations with two 7.5 mm plates and a 20.0 mm plate and by using any combination of the 3 plates. The half wave plate in between the delay plates improves the instrument contrast as discussed in Section 4.6. A 105 mm C-mount zoom lens was used as a collimation lens for flexible imaging and an interference filter at 468.9 nm with

1.0 nm bandwidth was used to transmit the He II line emission at 468.6 nm (same line as for the MOSS spectrometer on W7-AS). Figure 6.5 shows a spectrum of a Helium plasma in WEGA. The MOSS box was designed and constructed to include

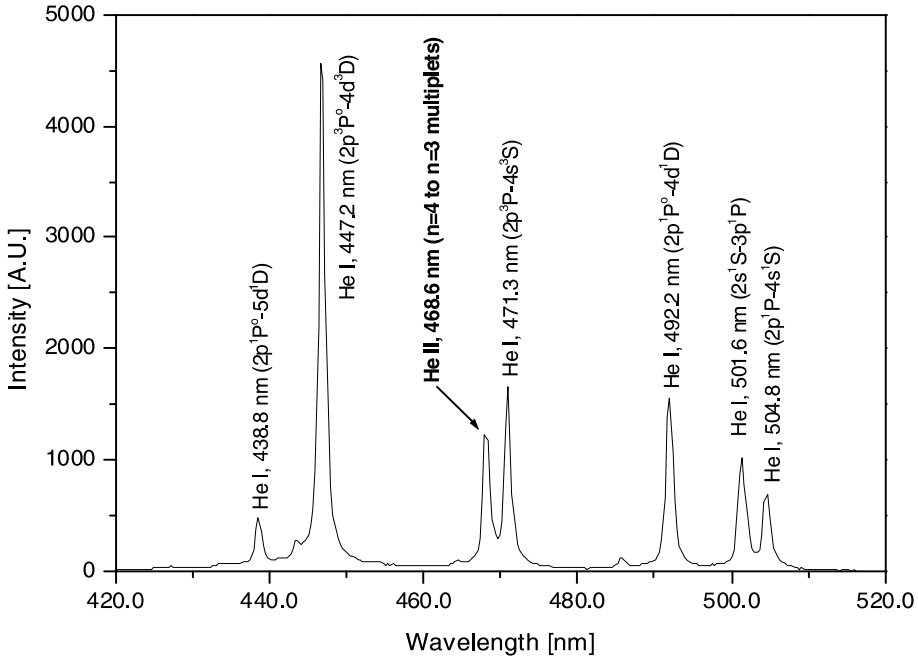

Figure 6.5: Spectrum of Helium plasmas in WEGA. The He II line at 468.6 nm is located in the center of the spectrum.

the calibration system. The schematic layout of the system inside the box was introduced in Section 4.8 where the beam splitter relays part of the incoming light emission to a 1D fiber array. The fiber array focuses the light on to the entrance slit of the Echelle grating spectrometer which is about 15 m away from the MOSS box. The photographs in Figure 6.6 show the structure of the MOSS box. A replaceable imaging lens module is mounted in front of the MOSS box. It allows us to adapt the size of the imaging planes for the MOSS spectrometer and other devices using the extension port on the box to the needs of the experiment. The lens module contains a single convex lens that forms a small viewing area. This simple lens configuration was used to look at a small region in the plasma center during the debugging of the system. It was useful for initial studies of the instrument function of the system because in this case we only measure homogeneous light and temperature surfaces. The simple lens module was later replaced by a module which consisted of a 75 mm camera lens combined with a concave lens with a focal length of −75 mm. The optical layout of the system with the resulting viewing area is shown in Figure 6.7. The focal length of the imaging module is 27 cm. Since the viewing angle is limited by the inner diameter of the viewing port, the full cross-section of the plasma at $\iota = 0.2$ is achieved only near the toroidal angle $\varphi = 36°$ as shown in Figure 6.7. Figure 6.8 shows the comparison of the viewing area demonstration in the laboratory and a snapshot of the He II line at $\iota = 0.2$ in WEGA. The handwritten numbers and dots on the vertical line in the middle of the left image represent the focusing area of

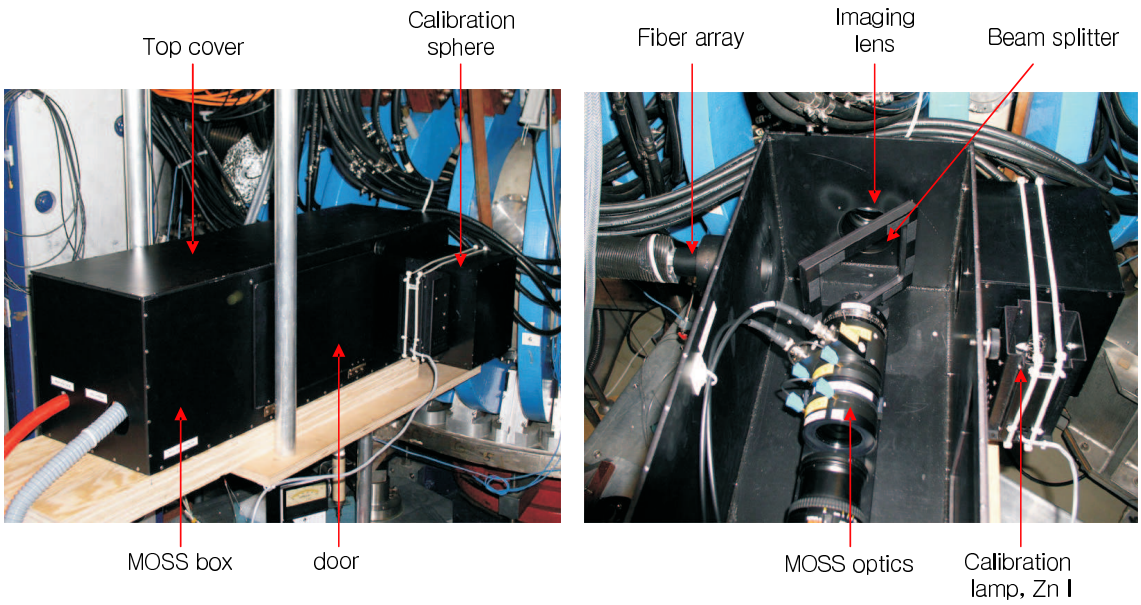

Figure 6.6: The MOSS spectrometer in WEGA.

each fiber of the Echelle grating spectrometer. The fibers look at the same region of the plasma. By rotating the fiber array 90 degrees it is also possible to observe the center of the plasma toroidally. Details of the specification and installation of the Echelle grating spectrometer are given in the following section. The right hand image of Figure 6.8 shows a mesh installed between the port window and the lens to protect the system from stray microwave radiation. The viewing area of the image covers 20 degrees toroidally. The center of the image is at $\varphi = 36°$. The position of the MOSS box on WEGA was illustrated in Figure 6.2.

6.2.2 Echelle grating spectrometer with a fiber array

For more reliable plasma diagnostics it is necessary to crosscheck the results with other diagnostics. To do this for the MOSS spectrometer, a high resolution spectrometer having an Echelle grating is used. An Echelle grating differs from a conventional grating in many ways [50]. The Echelle grating is used at high diffraction orders. The virtue of the Echelle grating is its high efficiency and low polarization effect over a large range of spectral intervals. This is achieved by tilting the individual reflective elements of the grating structure by an angle θ as shown in Figure 6.9. The Echelle grating also differs from the Echelette grating. For an Echelette grating, the longer groove facet (of length t in the figure) would face toward the incident and diffracted light. For an Echelle, the shorter steeper groove facet (of length s) is facing toward the light. The Echelle grating spectrometer provides a sufficiently high resolution to study WEGA plasmas.
The layout of an Echelle grating spectrometer installed in WEGA is shown in Figure 6.10, and its specifications are listed in Table 6.2. An important limitation

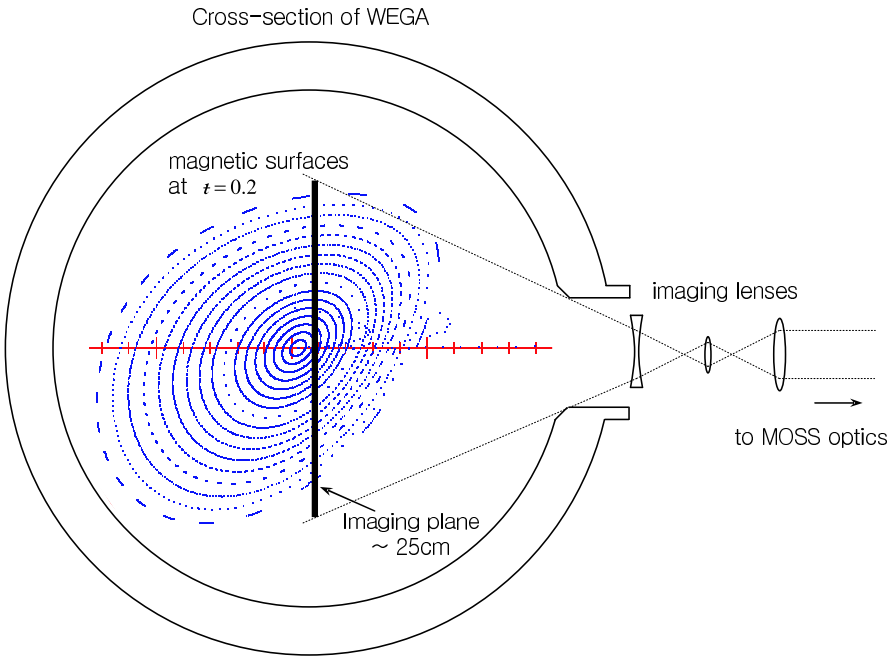

Figure 6.7: Scale drawing of the viewing area of the MOSS and Echelle grating spectrometer showing the magnetic surfaces with a rotational transform of 0.2 at $\varphi = 36°$, and also the imaging plane and a lens configuration.

of Echelle gratings is that the orders overlap unless separated optically. To overcome this limitation, a premonochromator is used as shown in Figure 6.10. Figure 6.11 shows the calculated and measured dispersion of the spectrometer, where the dispersion for the He II line at 468.6 nm is 1.11×10^{-3} nm/pixel. The Zn I line at 468.0 nm and the He-Ne laser line at 632.8 nm measured with the spectrometer are shown in Figure 6.12. The Zn I line is used for calibrating the MOSS spectrometer, and the He-Ne laser lines are used for the Echelle grating spectrometer. They are sufficiently narrow to calibrate the spectrometers.
The MOSS system is also designed to relay the incoming light emission to other optical diagnostics via a beam splitter as already shown in Figure 6.6. By using a 1D fiber array and suitable imaging optics for this configuration, the Echelle grating

Table 6.2: Specification of the Echelle grating spectrometer in WEGA.

Spectrometer	UHRS 1150 (SOPRA)
Focal length	1150 ±1 mm
Echelle grating	316 grooves/mm
Spectral range	200 – 800 nm
Dispersion	$6.0 \times 10^{-4} - 2.5 \times 10^{-3}$ nm/pixel
CCD camera	Roper Micro Max
number of pixels	512×512 pixels
pixel size	13×13 μm
Operation temperature	−40 °C (CCD chip)

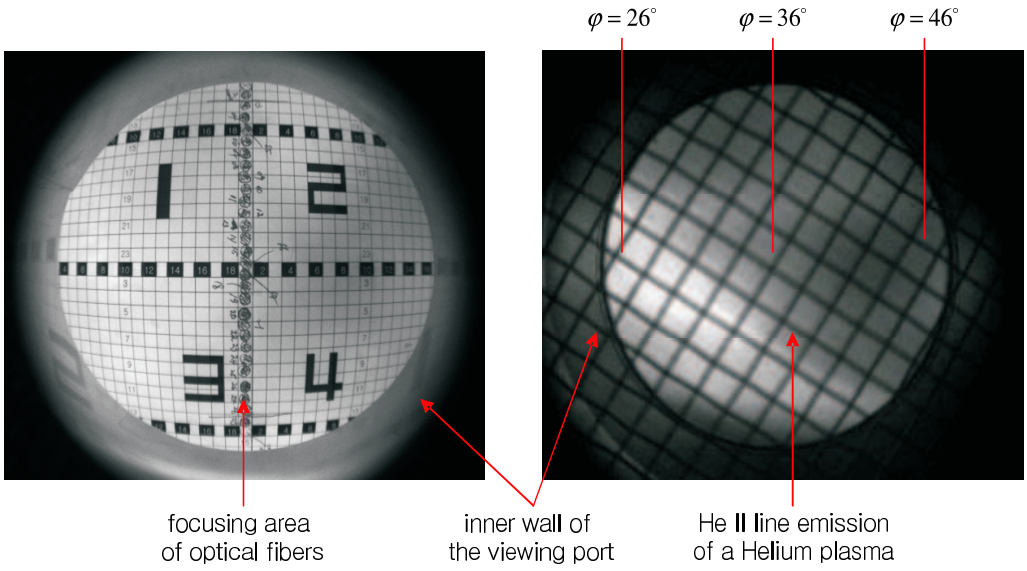

Figure 6.8: Comparison of the viewing area test in the laboratory (left) and in the WEGA stellarator with a Helium plasma at rotational transform of 0.2 (right). The viewing area covers 25 cm of the focal plane and 20 degrees toroidally.

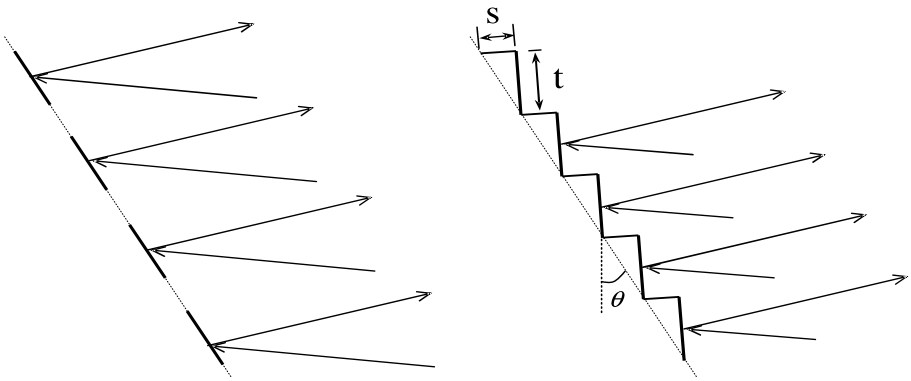

Figure 6.9: Comparison of the conventional grating (left) and Echelle grating (right).

spectrometer looks at the same position as the MOSS spectrometer.
The optical fiber bundle consists of 80 fibers which are arranged in a 1D array with a length of 18.0 mm. However, only 30 fibers in the middle of array are used because of a structural limitation of the system configuration. The fibers are made of fused silica each with a diameter of 200μm. A schematic of the optical layout of the fiber array is shown in Figure 6.13.

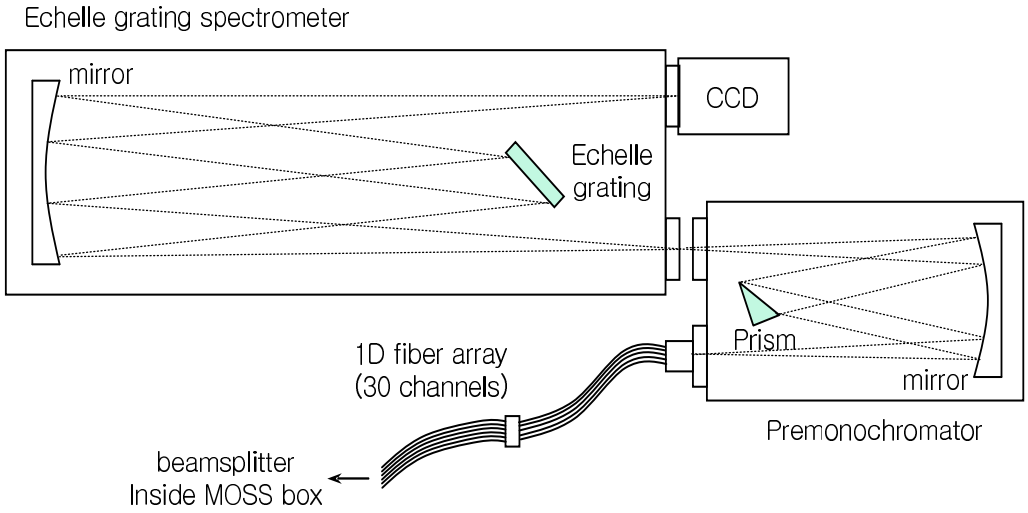

Figure 6.10: Schematic layout of the Echelle grating spectrometer installed on WEGA. One end of a 1D fiber array forms the curved entrance slit.

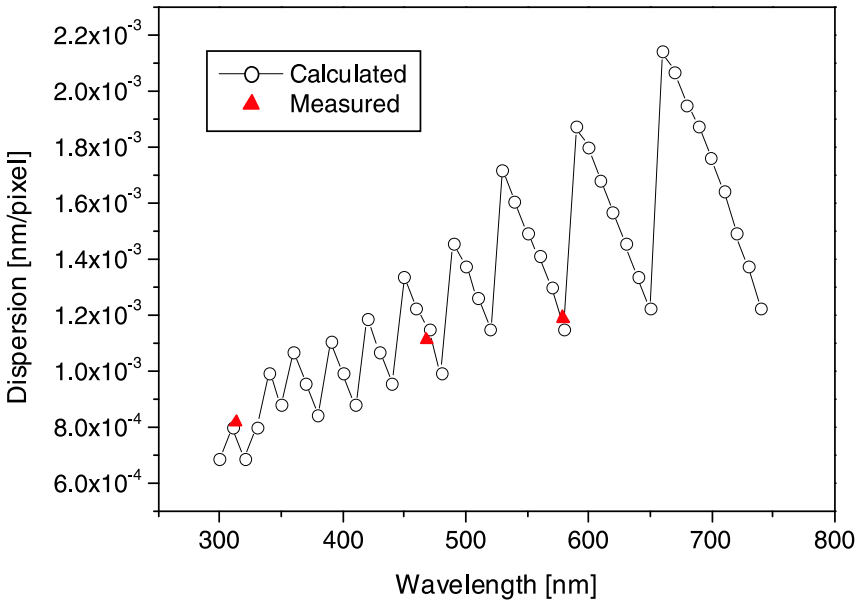

Figure 6.11: Comparison of the calculated and measured dispersion of the spectrometer. Measured points satisfy the calculated dispersion. Hg I at 313.15 nm and 313.18 nm, Cd I at 467.82 nm and Zn I at 468.01 nm, and Hg I at 578.97 nm and 579.07 nm lines are used for the measurement.

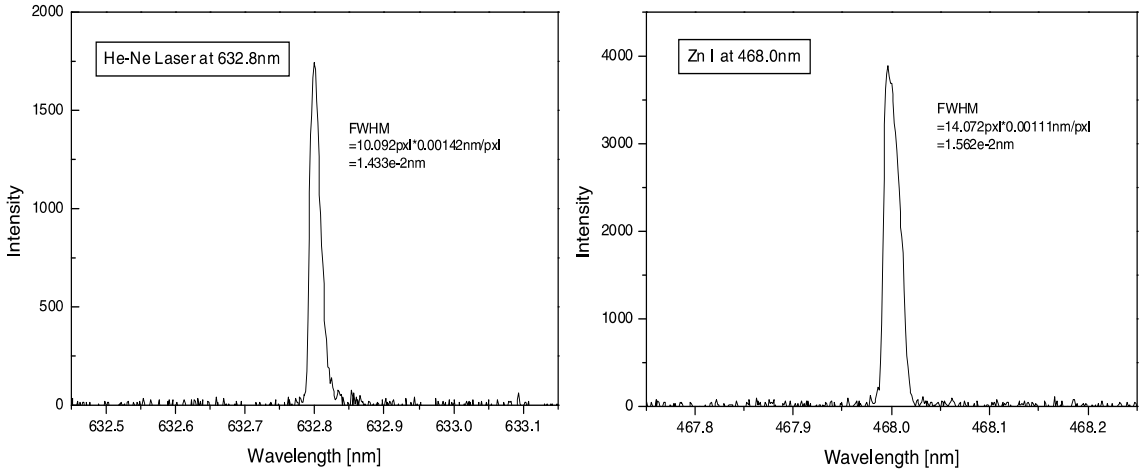

Figure 6.12: Zn I line at 468.0 nm and He-Ne laser line at 632.8 nm measured by the Echelle grating spectrometer on WEGA. These lines were used to determine the instrument function of the Echelle grating spectrometer and to calibrate the MOSS spectrometer.

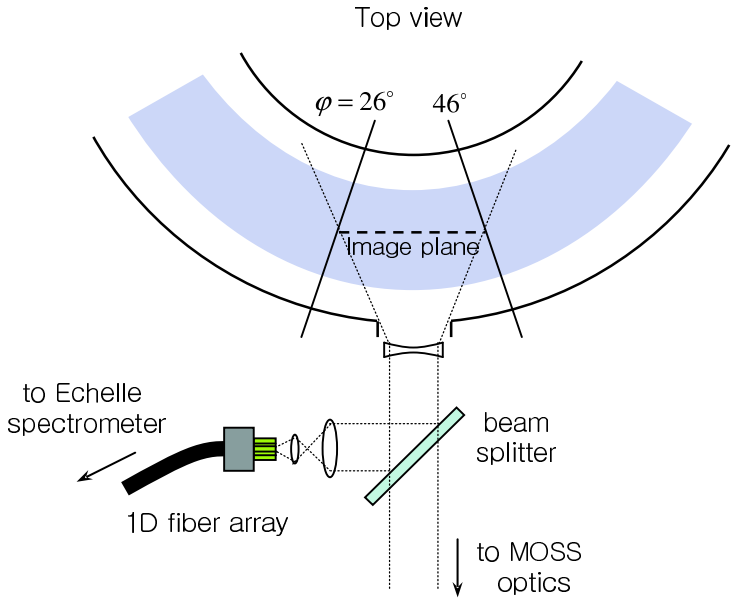

Figure 6.13: Schematic of the optical layout of the 1D fiber array for the Echelle grating spectrometer.

7

Results

This chapter contains experimental results from ECR heated Helium plasmas in the WEGA stellarator. The investigations were carried out with changing primary machine control parameters, e.g. ECR heating power and neutral gas pressure. For better understanding of the results, a coherence simulation result for the He II line (468.6 nm) and the nearest neighboring neutral Helium line, He I (471.3 nm), is presented at the beginning of this chapter before showing the experimental results. It is shown that the simulation result explains the experimental results satisfactorily. Magnetic field and rotational transform scans were also carried out to study ion temperature profiles and poloidal rotation in WEGA plasmas. The ion temperature and the poloidal flow as obtained from the Echelle grating spectrometer are also given to crosscheck the result from the MOSS spectrometer. Other base-line diagnostics such as a movable fast Langmuir probe and an interferometer were used to monitor the plasma.

7.1 Coherence simulation for a neighboring neutral Helium line

The method of coherence simulation and some of the results for the MOSS spectrometer construction were discussed in Chapter 3. All possible major broadening mechanisms for the complicated He II line at 468.6 nm which we observe in the WEGA stellarator are also covered in Chapter 3. However, since the simulation model created in Chapter 3 was based on the spectrum from the W7-AS stellarator which produces a much hotter plasma than WEGA, the neutral line was not considered.

The nearest neutral line to the He II is the He I line at 471.3 nm. A measured spectrum is shown in Figure 7.1(a). The He I line is about 10 times stronger than the He II line at full ECR power in WEGA. Although the interference filter at 468.9 nm has a narrow passband of 1.0 nm FWHM, the He I line must be considered since the passband profile of the filter is Lorentzian with a long tail. We have already seen in

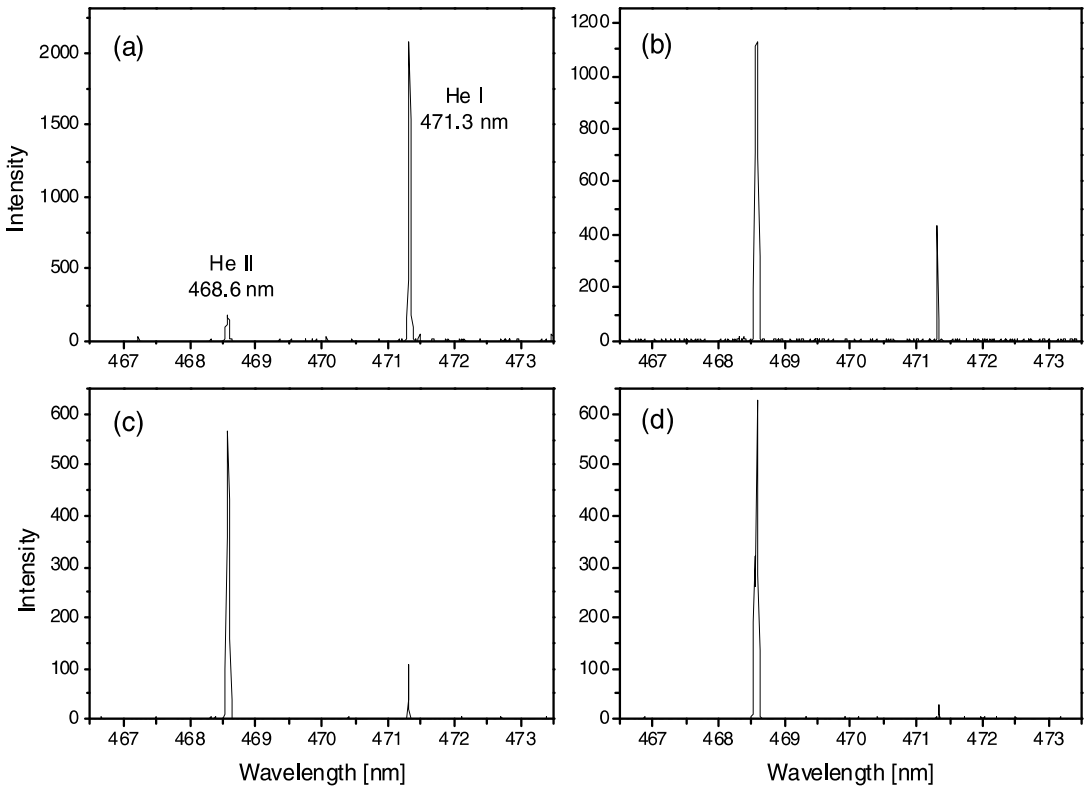

Figure 7.1: Measured spectral intensities of the He II line at $\lambda_0 = 468.6$ nm and He I line at $\lambda_1 = 471.3$ nm (a) without filter, (b) with a single interference filter tilted at 7.5 degrees, (c) with two combined interference filters (at $\lambda_f = 468.9$ nm), and (d) with two combined filters tilted at 7.5 degrees (corresponds to $\lambda_f = \lambda_0$). The He I line is about 10 times stronger than the He II line at full ECR power in WEGA, but it is almost gone when a tilted combined interference filter is used.

Section 3.5 that the even more separated C III line at 464.9 nm causes a fast beat pattern on the envelope of the He II filtered coherence.

A measured spectrum with the interference filter is shown in Figure 7.1(b). This is the case for the filter tilted at 7.5 degrees. By tilting the interference filter we can shift the bandpass to shorter wavelengths. This shift to shorter wavelengths at oblique incidence is very useful for fine tuning bandpass filters [51]. In our case, by tilting the interference filter by 7.5 degrees we moved the wavelength of maximum filter transmission (λ_f) to the center of gravity of the He II lines (λ_0) in order to maximize the measurable line intensity. At the same time the shift of λ_f towards λ_0 moves the disturbing He I line at $\lambda_1 = 471.3$ nm further into the red wing of the filter transmission curve thereby leading to an enhanced suppression of this line. Figure 7.1(b) shows the maximum improvement that can be achieved using this solution, but the He I line is still too strong. Figure 7.2 shows a simulation of this case. Since the filtered line intensity of the He I line is still fairly strong there are big oscillations on the coherence envelope. The smooth lines along the oscillating coherence envelope represent the result of the case shown in figure 7.1(d). When two filters having Lorentzian bandpass profiles are combined, the resulting band-

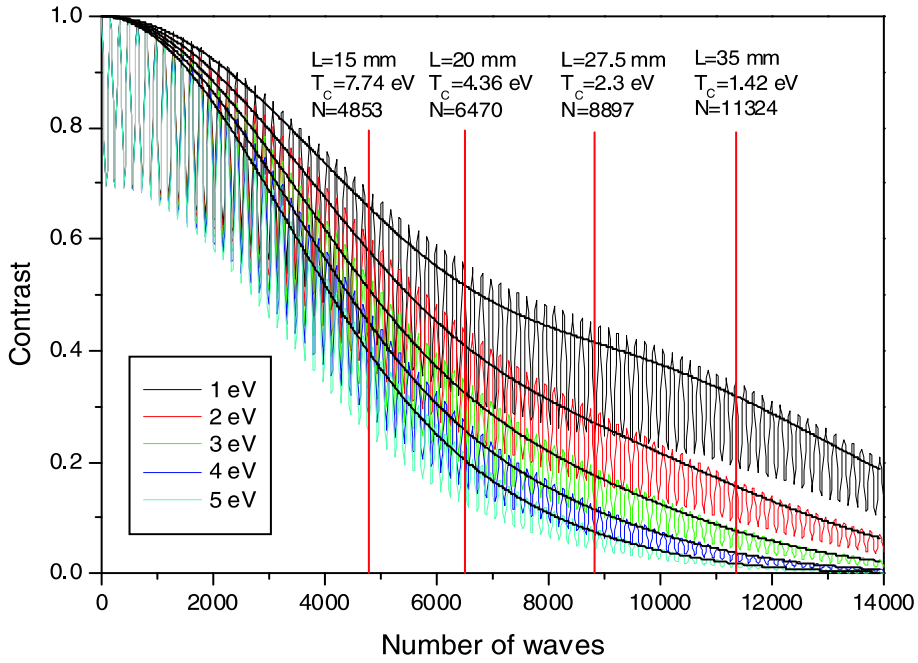

Figure 7.2: Coherence simulation result for $1-5$ eV with a single interference filter tilted by 7.5 degrees ($\lambda_f = \lambda_0$). When the He I line is included, the result is a largely oscillating fast beat pattern. When the He I line was excluded the coherence envelope would be flattened as shown by the smooth black lines. This figure also shows the available delay plate combinations indicated by the vertical lines.

pass profile is given by the multiplication of the two profiles. For the combined filter case since only $15-20$ % of the incident light can be transmitted, it provides a much narrower bandpass. Variations of filtered white light intensity at 468.6 nm and 471.3 nm by tilting a single filter and a combined filter are shown in Figure 7.3. The maximum intensity ratio of the two wavelengths is achieved at 7.5 degrees. A calibration sphere with a halogen bulb, as is used for absolute intensity calibrations, served for the spectrometer calibration and was used for this measurement as a white light source.

According to Figure 7.2, thicker delay plates result in a better dynamic resolution in the ion temperature range $T_i = 1-3$ eV. If only a single interference filter is used, in which case the He I line still strongly affects the results, then for thinner plates and higher temperatures the oscillating coherence patterns (shown in Figure 7.2 in steps of 1 eV) strongly overlap, so that for a given delay plate with its fixed wave number a measured contrast value no longer uniquely belongs to just one of the temperature curves, i.e., the uncertainty of the temperature measurement becomes larger than 1 eV. For the thickest delay plate ($L = 35$ mm) the contrast oscillations in the $T_i = 1-3$ eV range do not overlap and here the accuracy of the temperature measurement is slightly better than 1 eV. If the He I line is further reduced by using the combined filters then the optimum delay plate thickness depends on the expected plasma temperature range only. If the instrument contrast is small then the characteristic temperature T_c gives an optimum thickness. Note

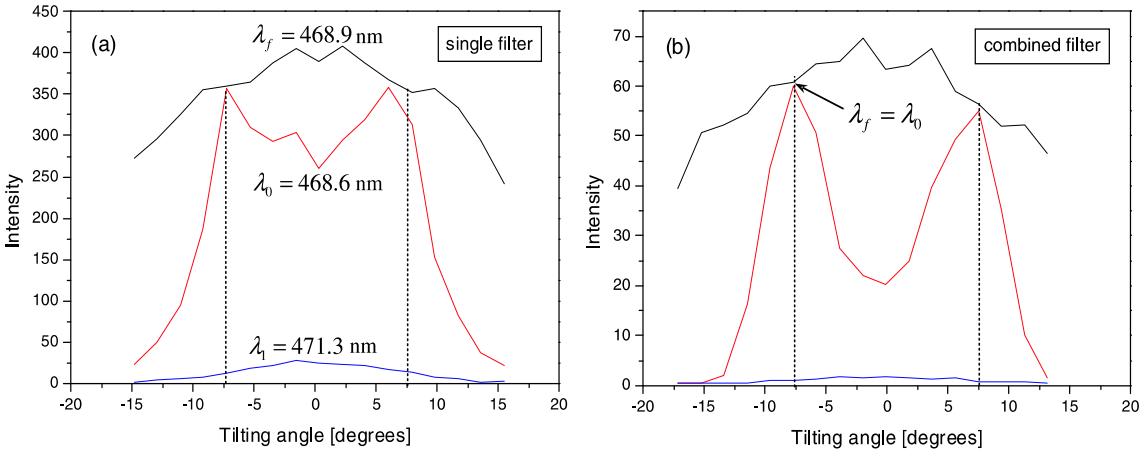

Figure 7.3: Variations of filtered white light intensity at $\lambda_0 = 468.6$ nm (He II) and $\lambda_1 = 471.3$ nm (He I) as a function of the tilting angle for (a) a single filter and (b) a combined filter. At 7.5 degrees the center wavelength of the bandpass profile coincides with the position of the He II line ($\lambda_f = \lambda_0$).

that only when the He I line is fully suppressed, one gets the correct temperature result. Any spurious lines lead to a significant systematic misinterpretation of the contrast measurement and thus to systematic error in the temperature measurement. The four different delay plate combinations (15.0 mm, 20.0 mm, 27.5 mm, and 35.0 mm) were tested for both single and combined filter cases during the ECRH power ramping. This is explained in the following section.

7.2 Power ramp

Power ramp experiments provide a lot of important information for both the MOSS spectrometer and the WEGA stellarator. First of all, from this experiment we measured the first poloidal profiles of the ion temperature and flow velocity on WEGA during ECRH power ramp experiments. These experiments were also used to investigate the dynamic dependency of the MOSS spectrometer on the ECRH power ramping. The measurement was useful for obtaining a better understanding of plasma phenomena within the capabilities of WEGA. The ECRH power was increased in steps from 10 kW to 26 kW. The plasma was produced by the first 6 kW magnetron and additionally heated by the second 20 kW magnetron. A typical power ramp is shown in Figure 7.4(a). The plasma pulse length was 42 s and the time resolution of the MOSS spectrometer was 100 ms. The rotational transform was $\iota = 0.56$ and the gas fill pressure was 0.035 Pa. All the other control parameters were constant during the discharges.

To study the dependence of the MOSS spectrometer response on the delay plate thickness, four different combinations of delay plates were used. Available thicknesses of delay plates were 15.0 mm, 20.0 mm, 27.5 mm, and 35.0 mm. To investigate the effect of the neutral Helium line on the MOSS measurement, a single interference

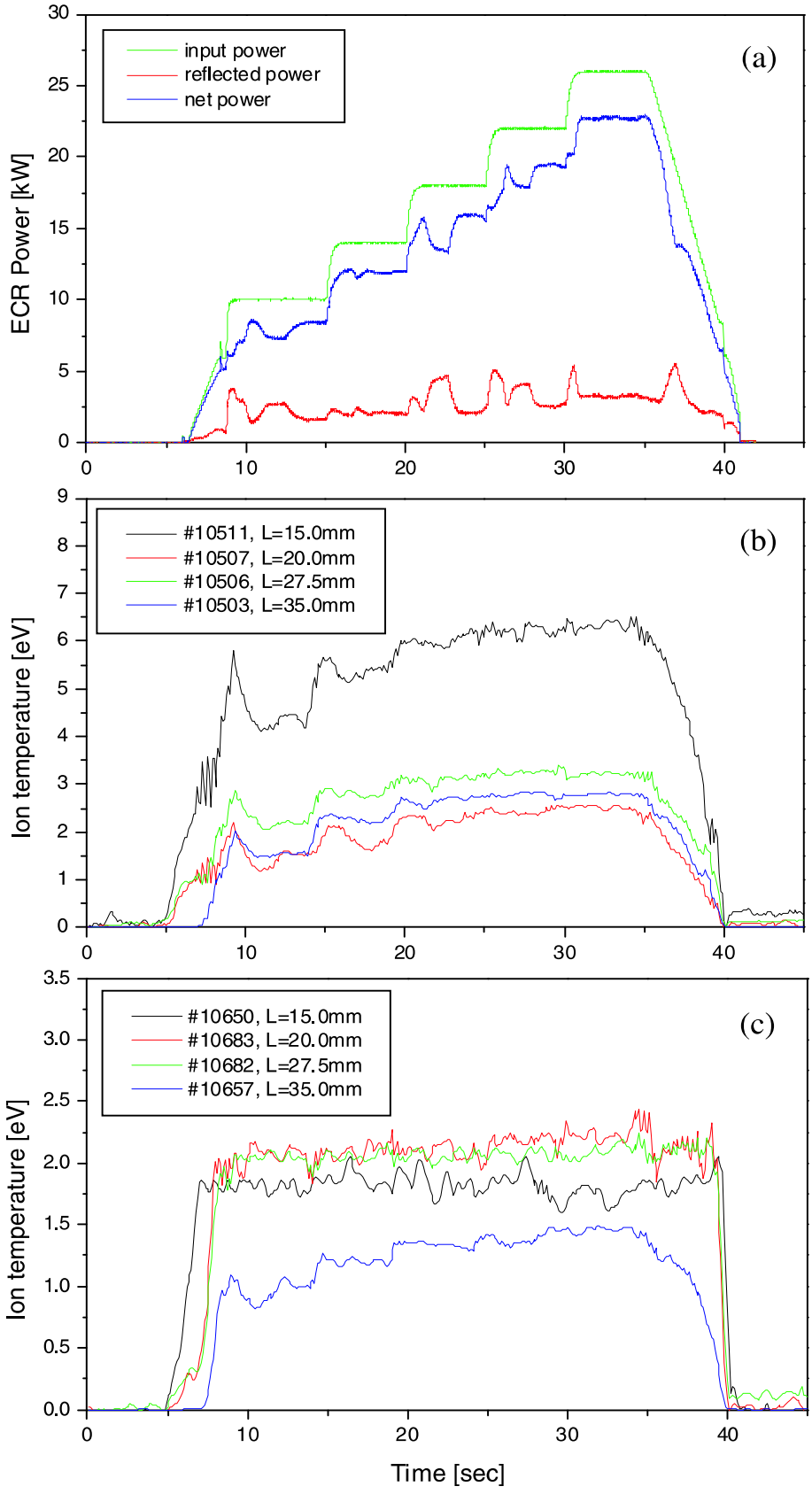

Figure 7.4: Initial ion temperature results using different 4 delay combinations from the power ramping experiment when (b) a single interference filter and (c) two combined interference filters were used. A typical ECRH power ramping for this experiment is shown in (a).

filter and two combined interference filters were used. The bandpass profile of the combined interference filters suppresses the He I line intensity sufficiently to become negligible in the filtered spectrum as already shown in the previous section.
Figure 7.4(b) shows ion temperatures when a single interference filter was used. Four different ion temperature plots in the Figure show different temperature results at each different delay plate combination. Figure 7.4(c) shows the ion temperature result when two combined interference filters were used. The temperature values are a factor of ~ 1.5 lower than in the case of a single interference filter. This difference can be explained by the effect of the He I line.
The simulations have shown that thicker plates result in a higher dynamic for $T_i = 1 - 3$ eV. The results shown in Figure 7.4 show that the 35.0 mm combination is an optimum delay for the present experimental conditions as explained in the following: The 15 mm plate gave much higher temperatures than in measurements with other plate combinations. According to the simulation result, at $N = 5000$ the coherence oscillation due to the He I line is overlapping with higher temperature coherence lines. This is the reason why the 15.0 mm plate yields higher temperatures. For the 20.0 mm plate the coherence oscillations are partially overlapping with higher temperatures. The temperature result is therefore still slightly higher, but this is probably due to the differences in instrument contrast at each thickness. The field widening using the half wave plate improves the instrument contrast as discussed in Section 4.6. This field widening reduces the spatial errors and increases the dynamic range of the MOSS spectrometer. This is very important for 2D imaging but since the field widening works better for similar delay or thickness of combined delay plates, the 35.0 mm combination consisting of two 7.5 mm plates and one 20.0 mm plate should be better than a single 20.0 mm plate or a combination of one 7.5 mm and one 20.0 mm plate. Using two 7.5 mm plates is the best choice here but since the resulting delay is too small or the characteristic temperature is too high, the dynamic range would be small for our experimental conditions. Figure 7.4(c) explains this very well. Although the double 7.5 mm combination gives similar temperatures compared to other combinations, the response which depends on the power increase is poor. Because of poor instrument contrast for the 20.0 mm and 27.5 mm combinations, only the 35.0 mm combination is able to resolve the small variation in the ion temperature. The instrument contrast for the different delay combinations is shown in Figure 7.5. Only the 35.0 mm delay plate combination provides a sufficiently constant instrument contrast across the CCD (Figure 7.5 shows a vertical cut). All subsequent measurements were performed using the 35.0 mm combination.
Figure 7.6 shows a typical result of a MOSS measurement during a power ramp experiment in WEGA. The ion temperature at the plasma center was about 1.5 eV at full ECRH power, and the electron density measured by an interferometer was about 2×10^{18} m^{-3}. Without additional ECRH power from the second 20 kW magnetron, the ion temperature was found to be already around 1.0 eV. The sec-

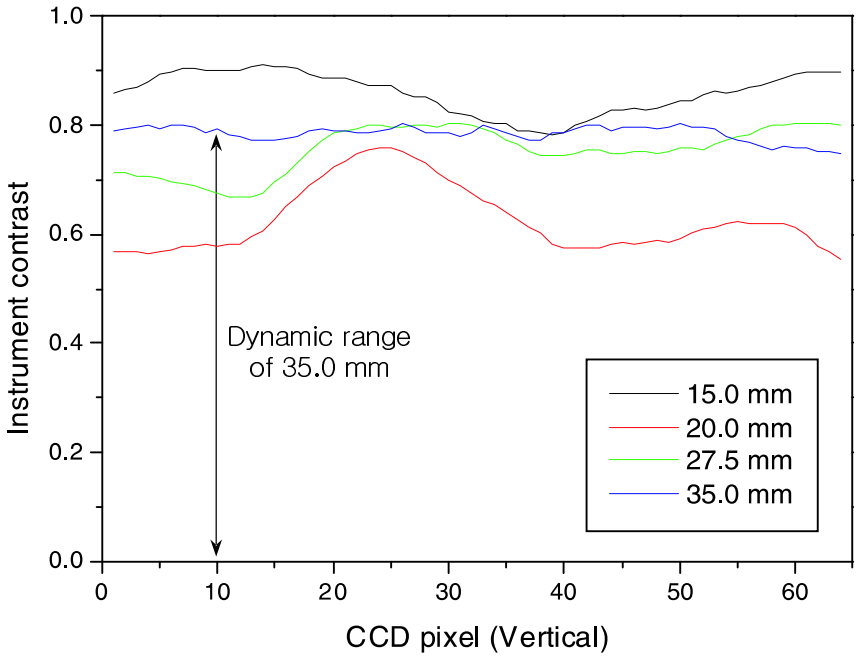

Figure 7.5: Measured instrument contrast of 15.0 mm, 20.0 mm, 27.5 mm, and 35.0 mm delay plate combinations. The 35.0 mm combination has constant instrument contrast along the vertical CCD pixel. The dynamic range of this combination is $0.0 - 0.8$. A calibration sphere served here as the homogeneous light source.

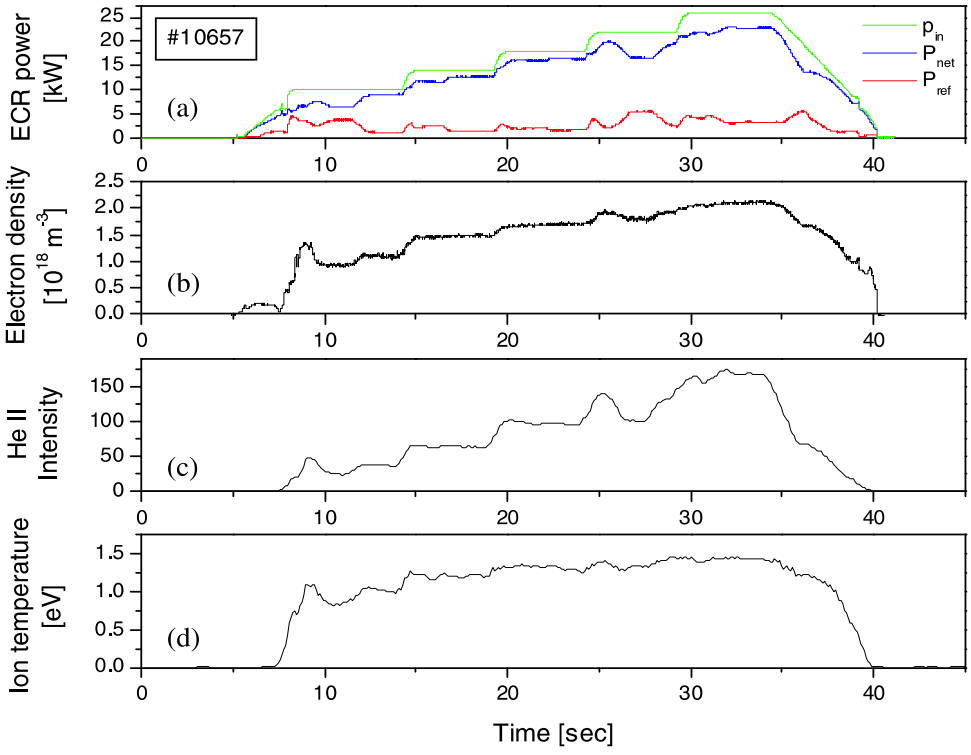

Figure 7.6: A power ramp experiment result showing (a) ECRH power, (b) line density measured by an interferometer, (c) He II emission intensity, and (d) the ion temperature at the plasma center as a function of time.

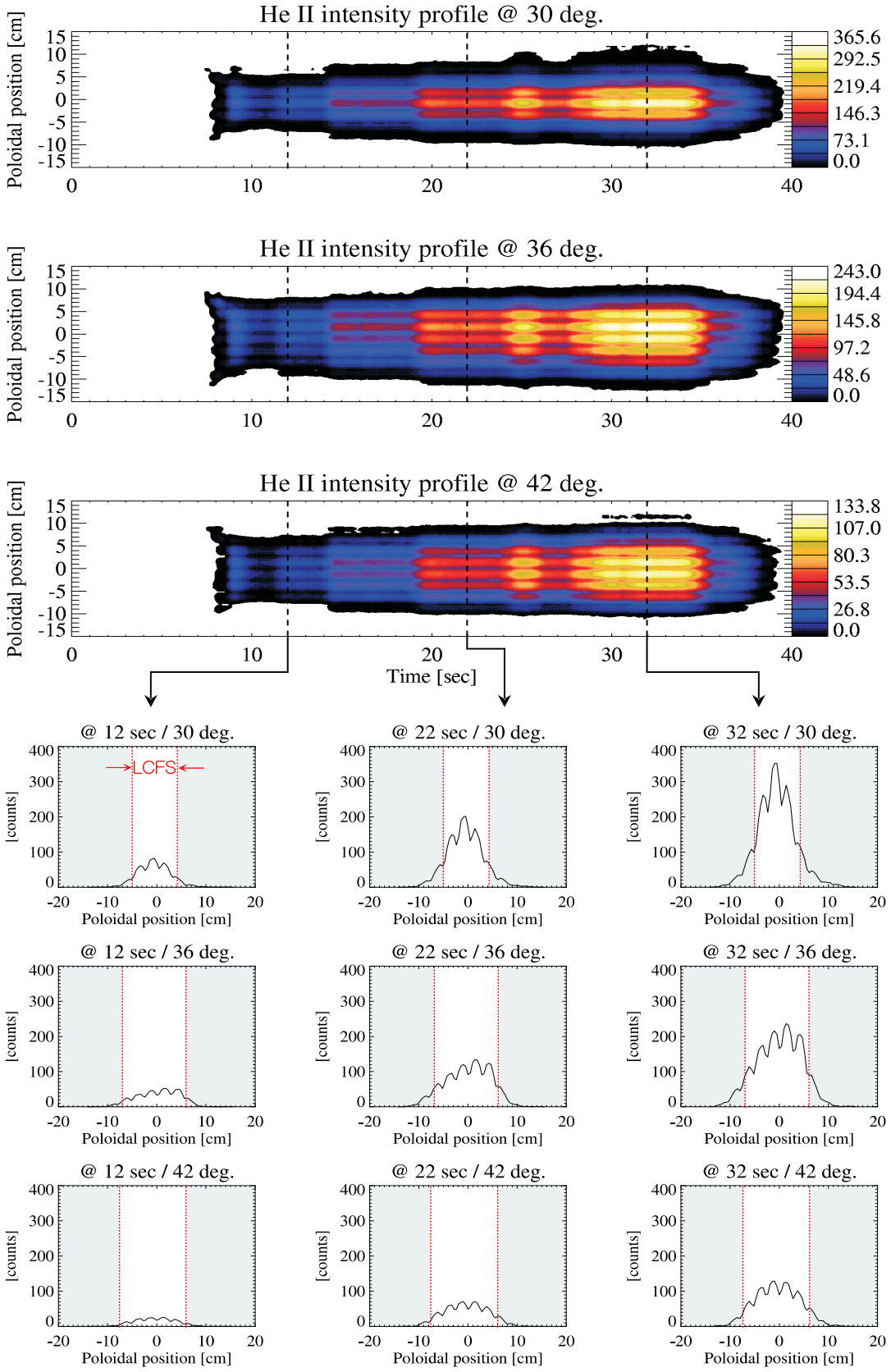

Figure 7.7: Contour plots of the line of sight (l.o.s.) averaged He II emission intensity profile at three different toroidal angles, 30, 36, and 42 degrees as a function of time, and profile plots at 12 s, 22 s, and 32 s (pulse no. 10657).

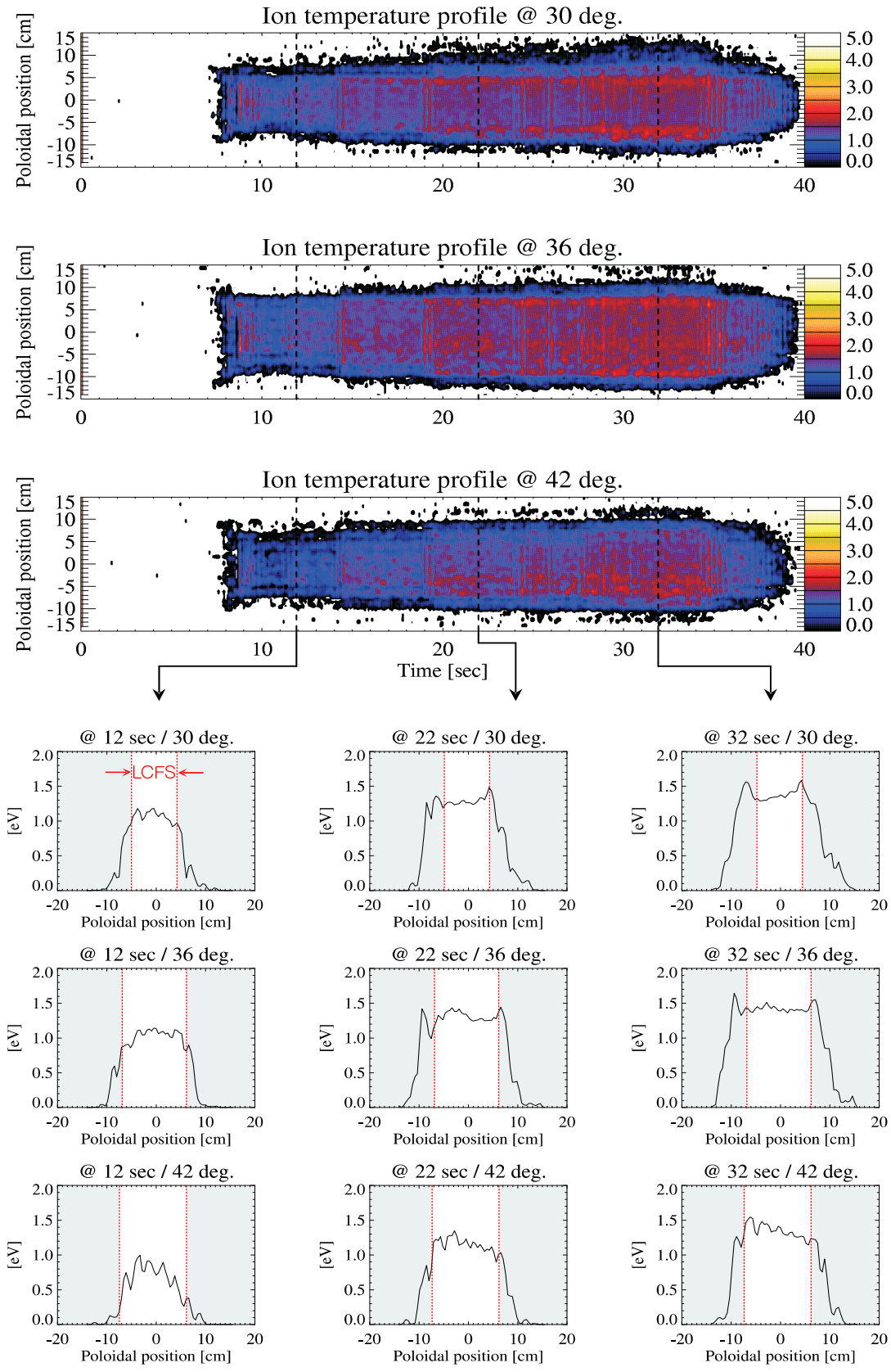

Figure 7.8: Contour plots of the l.o.s. averaged ion temperature profile at three different toroidal angles, 30, 36, and 42 degrees as a function of time, and profile plots at 12 s, 22 s, and 32 s (pulse no. 10657).

ond magnetron increased the ion temperature at the plasma center by about 0.5 eV through electron heating. Although the ion particles were not directly heated by the ECRH power, increasing the power by 400 % increases the ion temperature by only 50 %. This is a much smaller effect than originally expected. A possible reason could be found at the outer region of the plasma as discussed in the following:
Figure 7.7 and 7.8 shows the line of sight averaged He II emission intensity and ion temperature profiles of the power ramping discharge ♯10657 as a function of time at three different toroidal angles (30, 36, and 42 degrees). In Figure 7.7 the He II emission intensity is strongly correlated with the ECRH power. For example, when the net ECRH power was increased by 400 % in the interval of 12 - 32 s, the light intensity also increased by 400 % (Figure 7.7), while the ion temperature increased by about only 50 % over the same interval (Figure 7.8). Figure 7.7 shows that the width of the intensity profile corresponds to the location of the LCFS (last closed flux surface) as derived from vacuum magnetic field calculations. The location of the magnetic flux surfaces for $\iota = 0.56$ at toroidal angles of 30, 36, and 42 degrees are shown in Figure 7.9. The LCFS on the vertical axis at 30, 36, and 42 degrees has diameters of about 8.5, 11.6, and 12.5 cm respectively.
An interesting point can be made about the ion temperature profile (Figure 7.8): At higher ECRH power the ion temperature mainly increases in the vicinity of the LCFS. The ion temperature profile gets broader and flatter as the power is increased. Note that the He II emission intensity and ion temperature profiles behave differently for increasing ECRH power and we could suspect that the second 20 kW magnetron mainly heats the edge region of our plasma.
Figure 7.10 shows the radial profiles of the electron temperature measured by a fast reciprocating Langmuir probe at the ECRH power range of $10 - 26$ kW [52]. The electron temperature at the center of the plasma is $T_e = 5 - 7$ eV and there is no significant increase for the higher ECRH power. Since the probe scans radially at a different position of the toroidal angle, the profile can not directly be compared with the result from the MOSS spectrometer. We also measured the poloidal flow velocity at 36 degrees during the power ramp-up discharge (Figure 7.11). The poloidal flow velocity is around $\pm 500 - 1000$ m/s and it is somewhat faster at higher ECRH power. To verify that the velocity is induced by the plasma the toroidal magnetic field direction was reversed. In addition the line shift was measured using the Echelle grating spectrometer for both the standard and reversed toroidal magnetic field directions. This is discussed in depth in Section 7.6.
To crosscheck the ion temperature result from the MOSS spectrometer, the ion temperature was measured using the Echelle grating spectrometer while viewing the same poloidal plane through a beam splitter in the MOSS system. Since the He II line at 468.6 nm consists of 13 individual lines, the InSPECtor which is based on the fitting code KS4FIT originally developed at JET was used. Figure 7.12(a) shows a measured He II spectral feature and all the fitted individual components. For the fitting the relative wavelength positions as well as the relative intensities

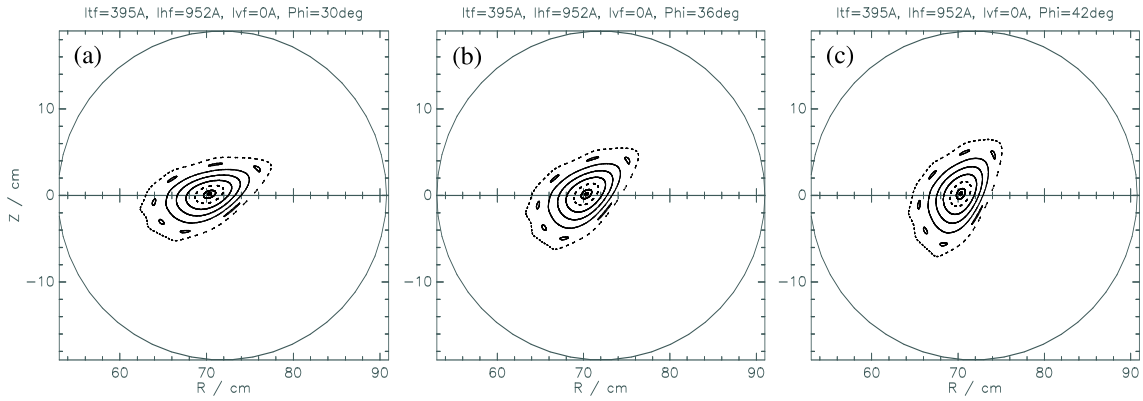

Figure 7.9: Plots of magnetic flux surfaces of the rotational transform 0.56 at (a) 30°, (b) 36°, and (c) 42° toroidal angles. Size and shape of the plasma at each toroidal angle are different. Since the MOSS spectrometer is a 2D imaging system, it provides poloidal profiles for many different toroidal angles at the same time.

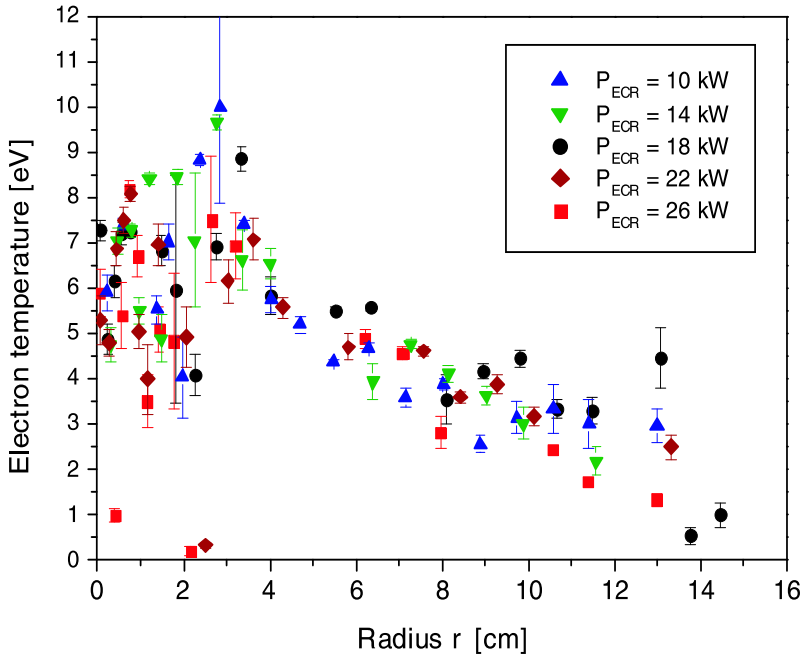

Figure 7.10: Radial profiles of the electron temperature at different ECRH power from $10 - 26$ kW measured by a fast reciprocating Langmuir probe [52].

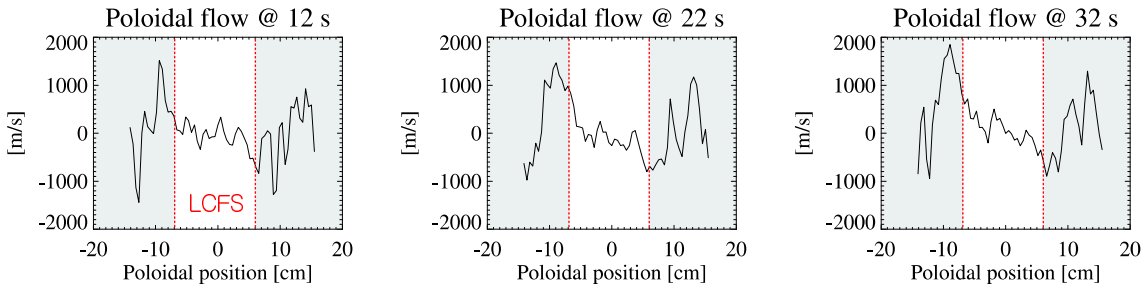

Figure 7.11: Measured poloidal flow at 12, 22 and 32 s. The dotted vertical line shows the LCFS at the top and bottom of the plasma. The flow velocity is around $\pm 500 - 1000$ m/s and it is faster at higher ECRH power.

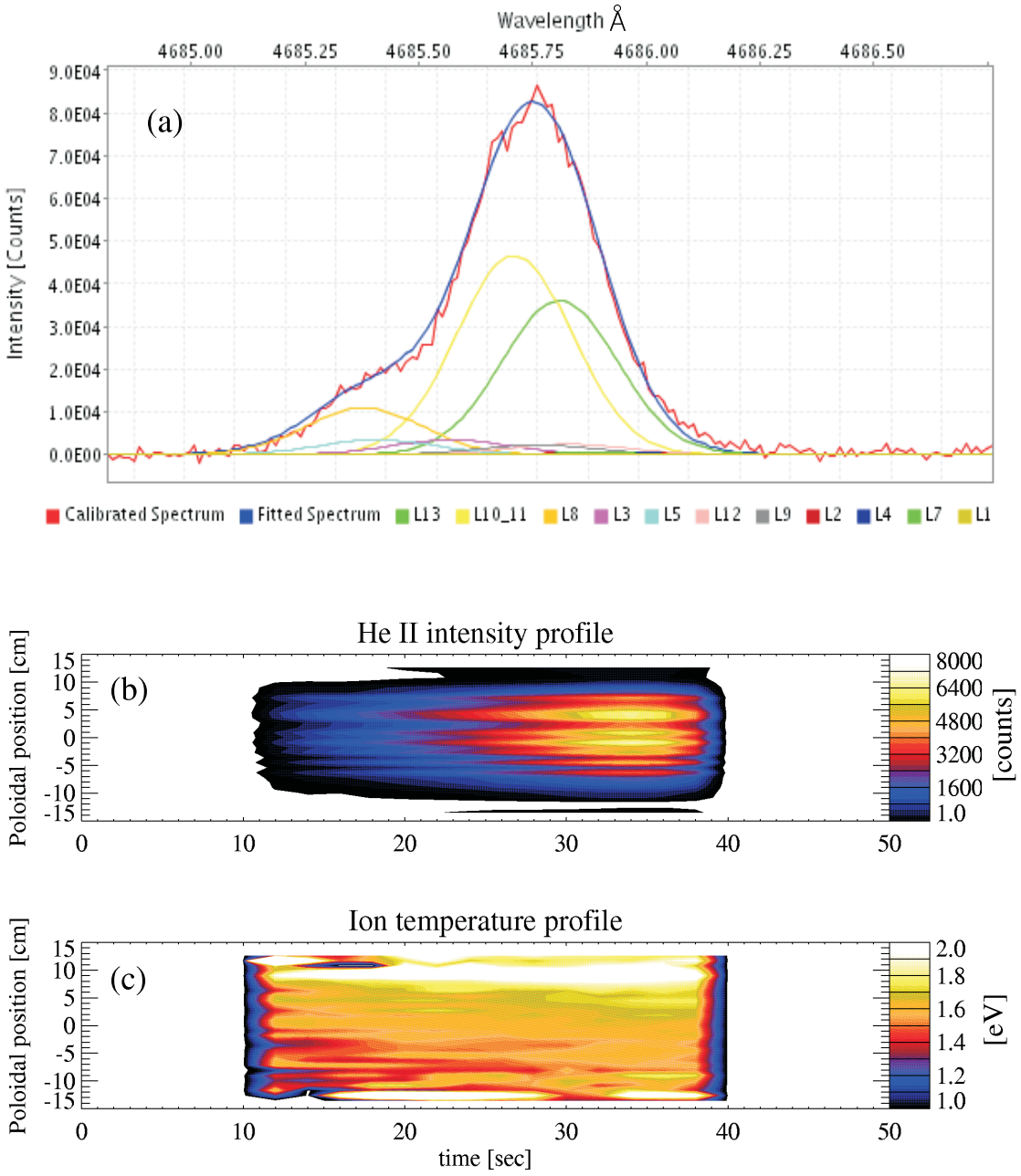

Figure 7.12: Fitted He II line at 468.6 nm using the KS4FIT code (a), and contour plots of the (b) He II intensity and (c) ion temperature profiles as a function of time.

(assuming that the levels were populated according to their statistical weights) of all 13 lines were used as coupling parameters. Therefore, effectively only the three fit parameters corresponding to a single Gaussian were determined. The resulting line shape of the 13 individual lines indicates that the assumptions made are consistent with the overall shape of the observed spectral feature. This is a further justification for the emission profile used for the coherence simulations described in Chapter 3 (e.g. see Figure 3.10(c) for $T_i = 1.0$ eV). Since the Echelle grating spectrometer is equipped with a 1D fiber array it provides a single poloidal profile at one selected toroidal location of the 2D MOSS spectrometer view. Poloidal profiles of the He II intensity and of the resulting ion temperature are shown in Figure 7.12(b) and (c). Since the throughput of the Echelle spectrometer is fairly low, the He II light intensity integration of the system was limited to $\Delta t \geq 2$ s, so that it was not possible to resolve the temperature or intensity changes during the ECRH power ramp. Because the ion temperature is a fitting result, it has an error range of $0.2 - 0.3$ eV at the plasma center. The error range at the edge is $0.5 - 1.0$ eV because of weak light intensity. The ion temperature from the Echelle grating spectrometer is $1.5 - 2.0$ eV at the plasma center. The ion temperature from the MOSS spectrometer is somewhat less but it is within the error range. The ion temperature at the plasma edge is slightly higher than at the center, and the width of the temperature profile is broader than that of the intensity profile. The same result was observed with the MOSS spectrometer. In conclusion, the ion temperature measurement of the MOSS spectrometer is reliable.

7.3 Neutral Gas pressure scan

To study the dependency of the ion temperature and poloidal flow on the neutral gas pressure, the gas flow was decreased in the possible range of the machine during a steady state discharge. The top half of Figure 7.13 shows the preprogrammed parameters (ECRH power and gas fill pressure) and the measured plasma parameters (electron density from an interferometer, He II intensity and ion temperature) from the MOSS spectrometer at the plasma center as a function of time. To stabilize the plasma condition while decreasing the gas pressure, 60 % (16 kW) of the maximum power was used in the experiment.

From $15 - 20$ s the control parameters were kept constant so that the plasma parameters could stabilize. At 20 s the gas pressure was reduced. This led to a decrease of the electron density and to an increase of both the He II intensity and the ion temperature. We tried to find the gas pressure at which the ion temperature reaches a maximum but such a point could not be found. The lower the neutral pressure the higher the ion temperature and the lower the electron density. The lowest density was 1.0×10^{18} m^{-3} at 0.01 Pa. The poloidal profiles of the He II intensity, ion temperature, and poloidal flow at 17, 25, 30, and 34 s are shown at the bottom of

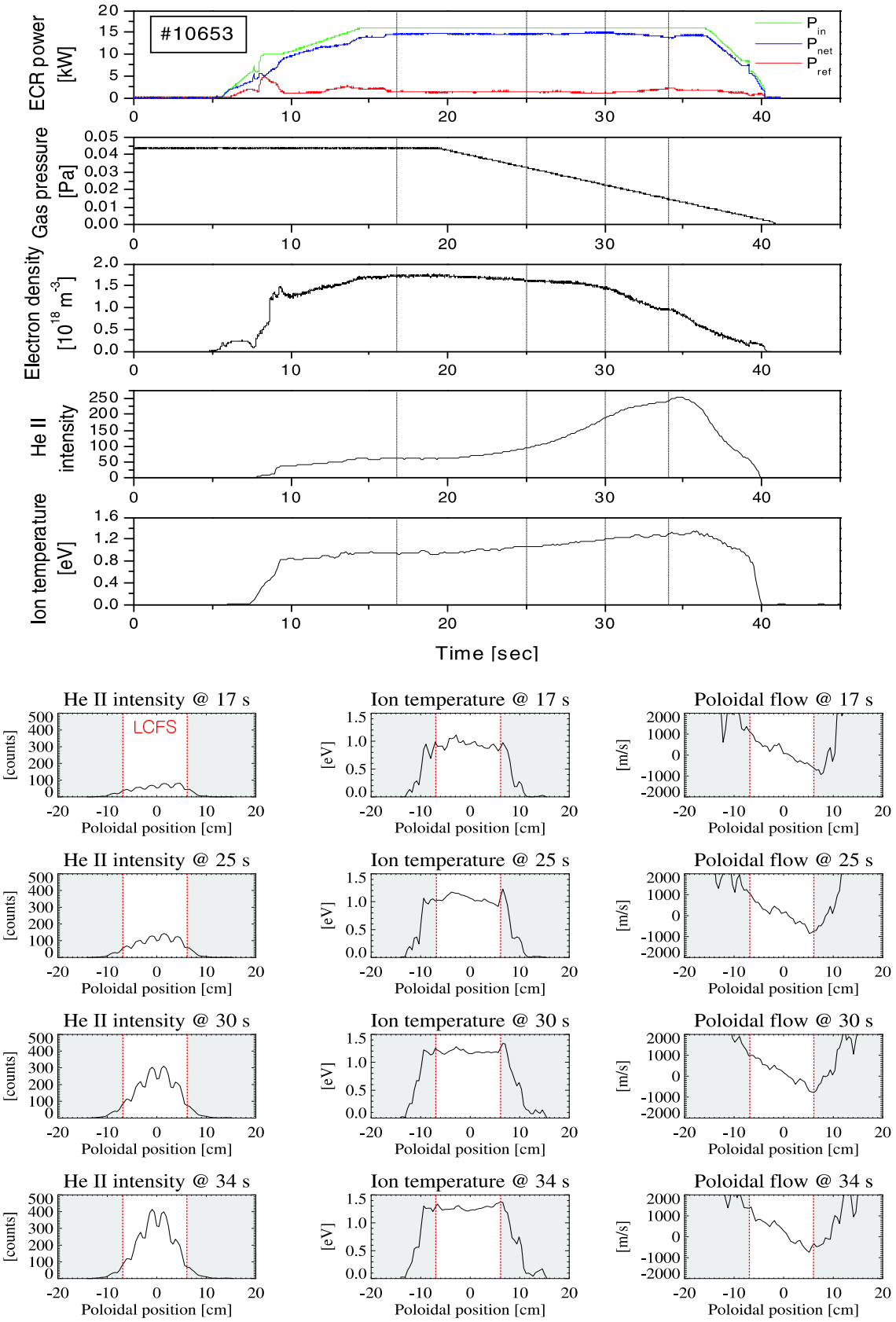

Figure 7.13: Machine and measured plasma parameters at the plasma center as a function of time (top), and the profiles at 17, 25, 30, 34 s from the MOSS spectrometer (bottom).

Figure 7.13. The width of the poloidal He II intensity profile is similar to the LCFS size. The intensity rises with increasing gas pressure. The ion temperature profile becomes flatter at lower gas pressure. The intensity and temperature profiles behave similarly to the ECRH power ramp-up described in the previous section. The flow velocity decreases with gas pressure. This means that the radial electric field is reduced at lower gas pressure, since the poloidal plasma flow is mainly caused by $E \times B$ drift. For comparison, Figure 7.14(a) shows a radial profile of the plasma potential at different neutral gas pressures measured by a fast reciprocating Langmuir probe [52]. Although the potential was measured at somewhat lower ECRH power, it is enough to confirm that the plasma potential is proportional to the gas pressure. The radial electric field near the LCFS position is $E_r = 50 - 70$ V/m, and this is a bit stronger at higher gas pressure as shown in Figure 7.14(b).

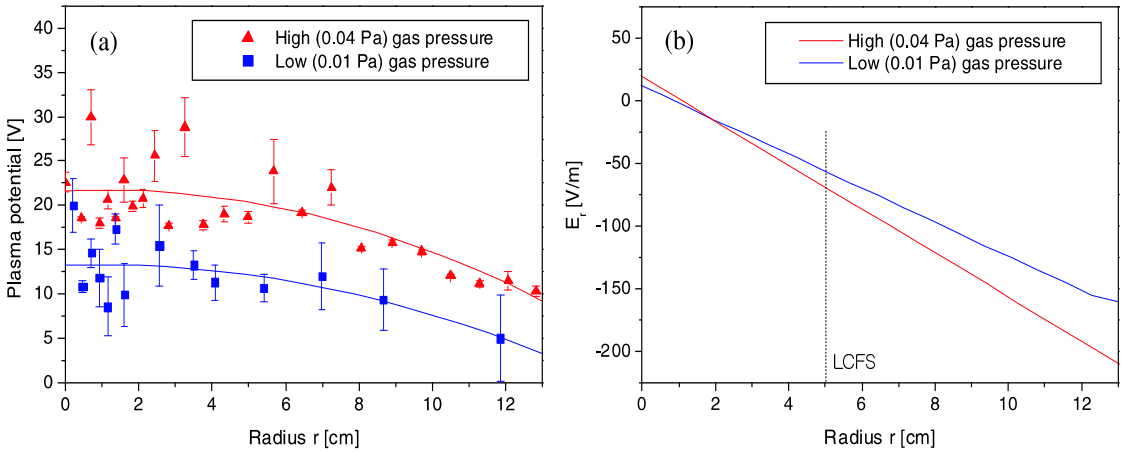

Figure 7.14: (a) Radial profiles of a plasma potential and (b) radial electric field at low (0.01 Pa) and high (0.04 Pa) gas pressures measured by a fast reciprocating Langmuir probe.

7.4 Magnetic field scan

ECR heating is a reliable electron heating method in magnetized plasmas. In the WEGA stellarator two magnetrons (6 kW and 20 kW) at 2.45 GHz are available for ECR heating as already introduced in Section 6.1. In the WEGA stellarator it is interesting to investigate the best field strength within a given machine capacity for the heating. We measured the ion temperature profile while changing the magnetic field strength on a shot by shot basis. The field strength was varied from 0.5 to 1.0 times $B_0 = 87.5$ mT. This field strength was selected in order to fullfill the resonance condition

$$\omega_c = \frac{qB}{2\pi m} \tag{7.1}$$

for the magnetron operating at 2.45 GHz.

As already described above, the additional 20 kW magnetron is not very effective

for the heating as it contributes mainly to the edge plasma heating. For those experiments, $0.65B_0$ was used to make better (higher T_i and n_e with the lowest ECRH power reflection) plasma conditions. From experience it was expected that the ion temperature should be a maximum near this magnetic field strength.

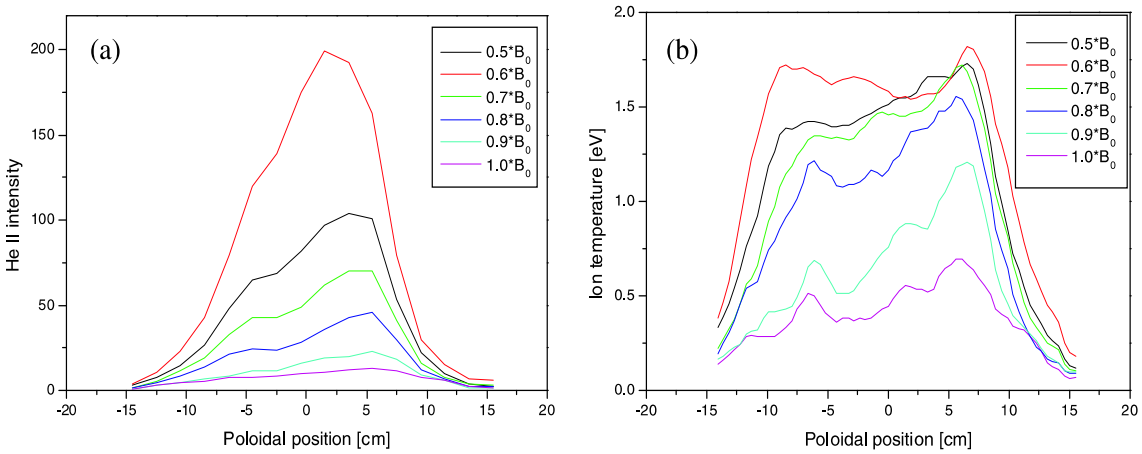

Figure 7.15: He II intensity (a) and ion temperature (b) profiles at various magnetic field strengths.

Figure 7.15 shows the He II intensity and ion temperature profiles for different field strengths at full ECRH power. The He II intensity at $0.6B_0$ is almost twice as high as the second highest intensity at $0.5B_0$. The ion temperature also shows its maximum at $0.6B_0$. The ion temperature at the top of the plasma ($5-10$ cm poloidal position) is similar for $0.5B_0 - 0.7B_0$, but only at $0.6B_0$ is the ion temperature at the bottom of the plasma more or less the same as it is at the top. The profile is a little broader than others at this field strength.
As a first interpretation, Figure 7.16 shows a contour plot of the magnetic field strength for the $0.6B_0$ configuration at $\varphi = 36°$. A contour line of the second harmonic resonance layer at $B = 0.5B_0$ is at the top of the plasma edge. At higher field configurations, the second harmonic layer moves to the right. The higher temperature at $0.6B_0$ and better heating efficiency at the top of the plasma seems to be due to the edge plasma heating at the second harmonic resonance. Since the source frequency at 2.45 GHz is too low to penetrate a plasma with an electron density around $10^{18}m^{-3}$, the ECRH power can only heat up the edge region. This will be discussed in more detail in Section 8.1.

7.5 Profiles at different rotational transforms

By changing the ratio of the helical and toroidal magnetic field strength we can change the rotational transform. The resulting rotational transform ι is calculated by Equation (6.2).

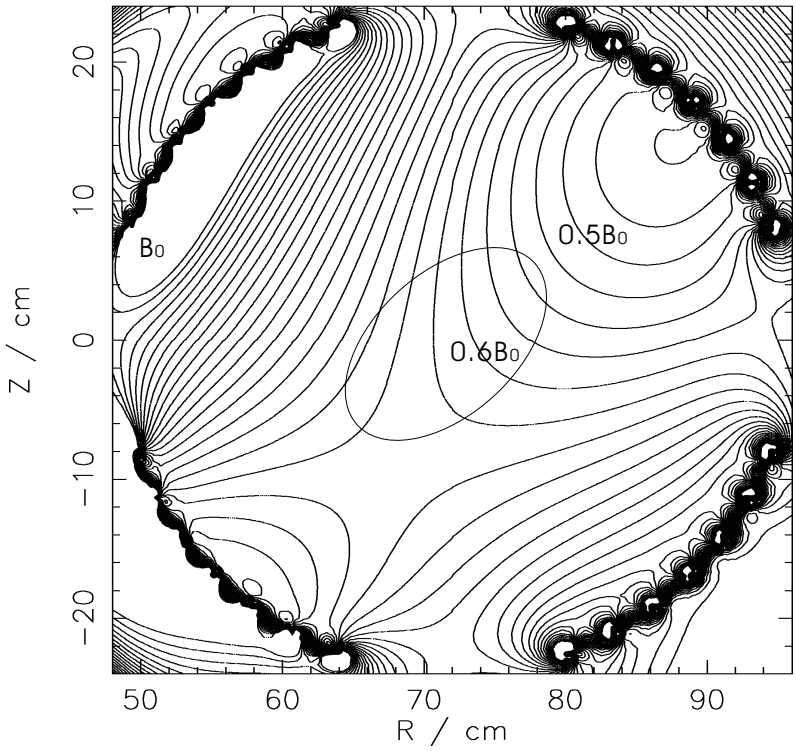

Figure 7.16: Plot of the magnetic field strength contour lines at $\varphi = 36°$. For $B = 0.6B_0$, the field strength for the second harmonic layer is at the top of plasma edge. It seems that the ECR magnetrons heat up the plasma mainly near the second harmonic resonance. The ECR heating at 2.45 GHz can not penetrate the plasma because of the high electron density. The electron density must be less than the cut-off density which is determined by plasma frequency for collective bulk plasma heating.

The plasma radius a is larger at smaller ι, and for some ι configurations magnetic islands exist inside the LCFS. The physical location of an island can be important. For example, if it is located equidistant from the plasma core and the edge it may hinder the poloidal transport because it is a sort of spatially discrete point. Islands located in the plasma edge are of special interest for island divertor research in stellarators.

To study different plasma configurations in WEGA, the vacuum magnetic flux surfaces were calculated for different rotational transforms at $\varphi = 36°$ (Figure 7.17). For $\iota = 0.26$ large internal magnetic islands exist while for $\iota = 0.37$ only small islands form at the edge. The plasma minor radius a of both configurations is almost twice as large as the radius of the configuration with $\iota = 0.56$ (see Figure 7.9), which was studied in the previous sections.

Figure 7.18 shows the He II intensity, ion temperature, and flow velocity profiles for $\iota = 0.26$ and 0.37 at full ECRH power. The He II intensity profile is flatter for $\iota = 0.26$ and the ion temperature profile is equally flat for both configurations. Since the plasma size is doubled (compared to the $\iota = 0.56$ case) the width of profiles is much broader. However, the largest difference between the two rotational transform configurations is the poloidal flow profile. For $\iota = 0.26$ the flow profile shows two

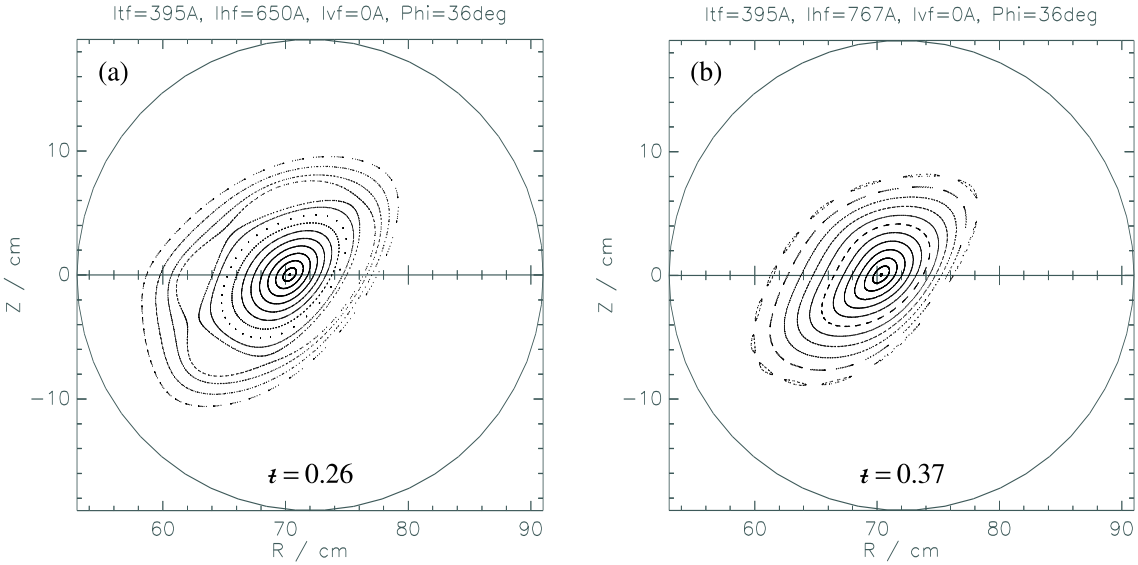

Figure 7.17: Plots of magnetic flux surfaces of the rotational transform (a) 0.26 and (b) 0.37 at $\varphi = 36°$.

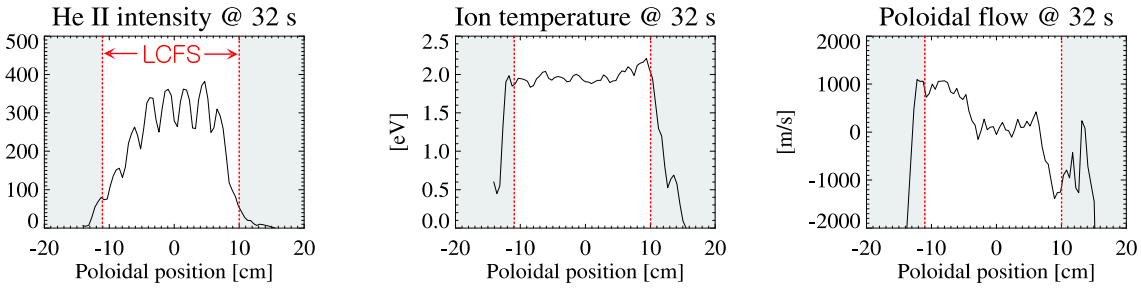

(a) Profiles at $\iota = 0.26$

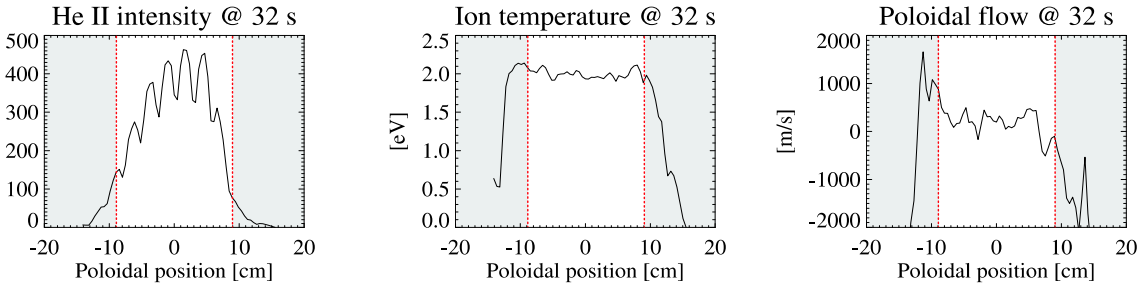

(b) Profiles at $\iota = 0.37$

Figure 7.18: Profiles of the He II intensity, ion temperature, and flow velocity for rotational transforms of (a) 0.26 and (b) 0.37 at full ECRH power. The profiles are broader because of the larger plasma radius at smaller rotational transforms, and the ion temperature profile is flat. The flow velocity profile is significantly different for different rotational transforms. It is reproducible and seems to be due to the island positions.

regions of constant velocity where the internal islands are located. The shape of the profile looks like a stair step while for $t = 0.37$ the velocity peaks at the very edge of the plasma. Although the profile is averaged along the viewing line, it seems clear that the different flow profile shapes are connected with the islands.

7.6 Reversed toroidal magnetic field direction

Measurements were done with reversed toroidal magnetic field, complementing the results in the previous sections. Figure 7.19(a) illustrates the $E \times B$ drift for the

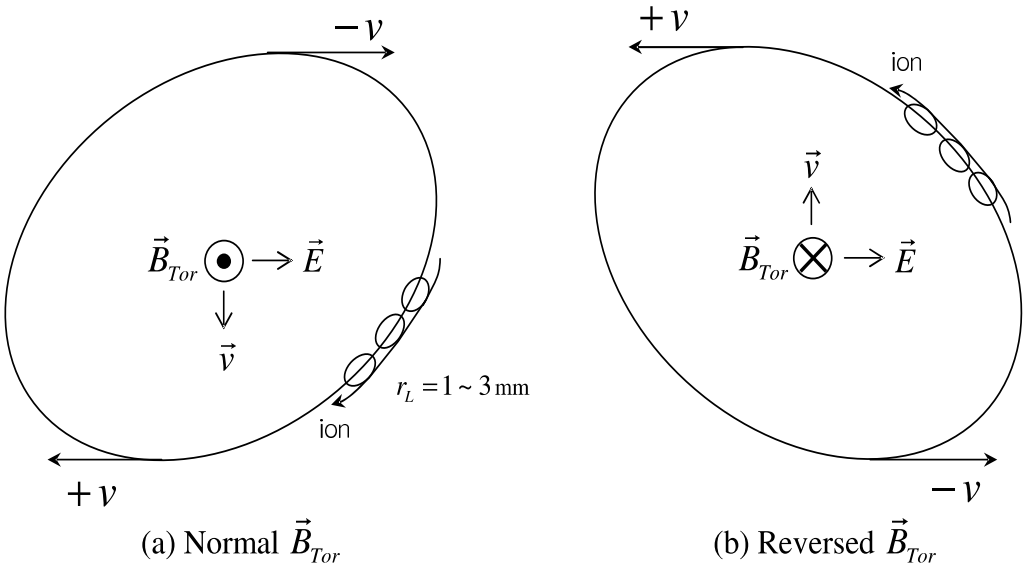

Figure 7.19: Illustrations of the $E \times B$ drift at (a) normal and (b) reversed toroidal magnetic field direction. Since the Lamor radius of the ion is very small compared to the plasma radius, the observed flow velocity is a macroscopic drift. The diamagnetic drift also has the same direction for the ion, but only the $E \times B$ drift is illustrated in this figure.

standard magnetic field configuration, where the flow velocity is negative at the top of the plasma and positive at the bottom. Since the velocity is observed from the right hand side of the plasma, the direction of the observed drift motion coincides with direction of the $E \times B$ flow velocity. Figure 7.19(b) illustrates the direction of the $E \times B$ drift when the toroidal magnetic field is reversed. In this case the elliptical shape of the magnetic flux surfaces are mirroring, and the polarity of the velocity at the top and bottom is reversed due to the opposite direction of the toroidal magnetic field. Figure 7.20 shows measurements taken with the MOSS spectrometer for a discharge with reversed toroidal magnetic field. The first four graphs are typical traces of a discharge for this reversed field experiment as a function of time, and the others are the poloidal profiles of the He II intensity, ion temperature, and poloidal flow velocities at 20, 28, and 33 s. Since the shape of the magnetic flux surface is mirrored and the shape of plasma has slightly changed, the intensity and temperature profiles are a bit different, but the magnitudes are more or less the

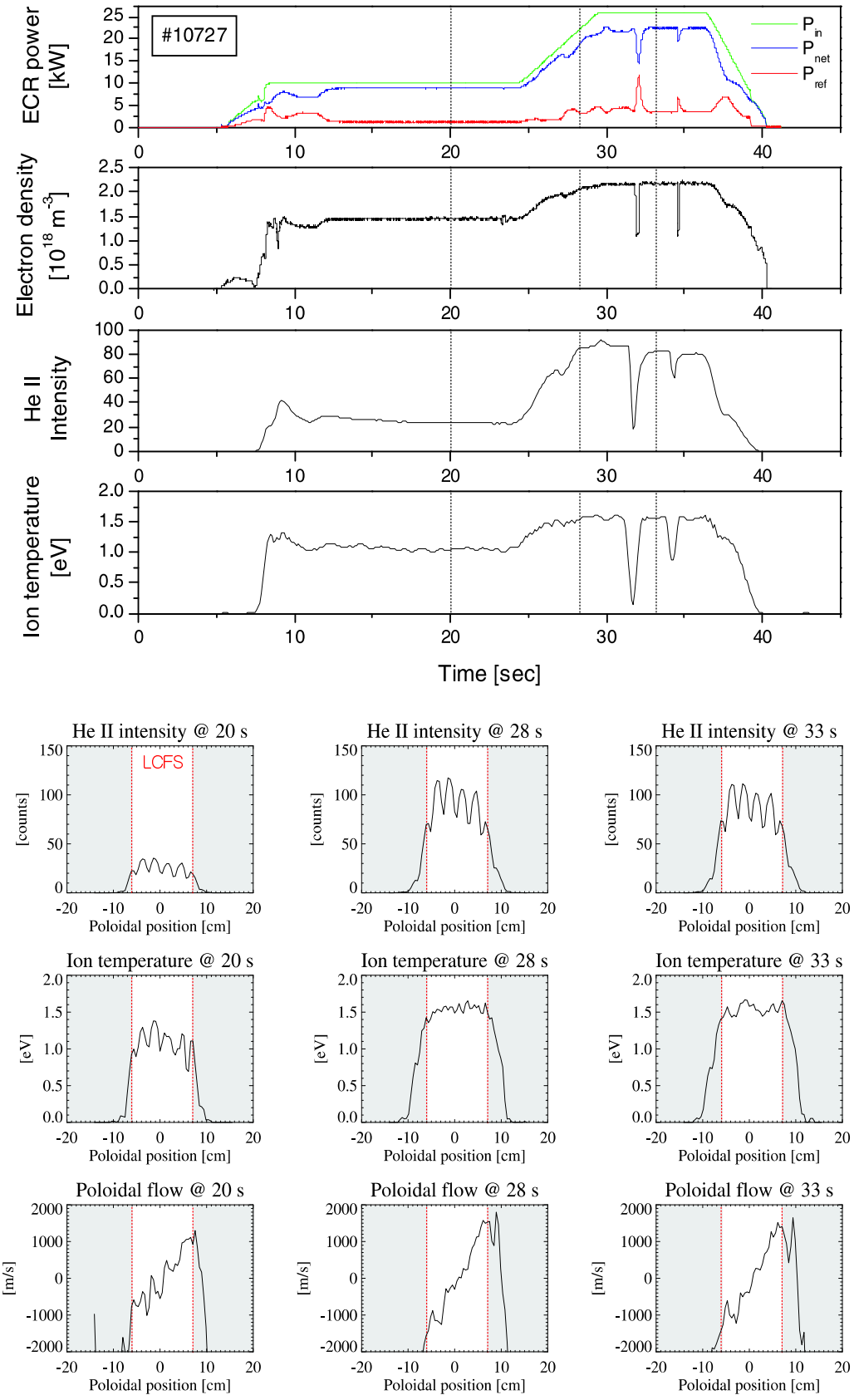

Figure 7.20: Typical traces of a discharge in which reversed poloidal flow measurements were performed (top), and poloidal profiles at 20, 28, and 33 s (bottom). The direction of the flow velocity is reversed due to the reversed toroidal magnetic field direction.

same. The most interesting result of the experiment is given by the last three poloidal flow profiles at the bottom of the figure. The direction of the velocities at the top and bottom of the plasma reverse (Figure 7.19). With reversed field direction the velocity is increasing with ECRH power. The magnitude of the velocity is similar to the standard field configuration.

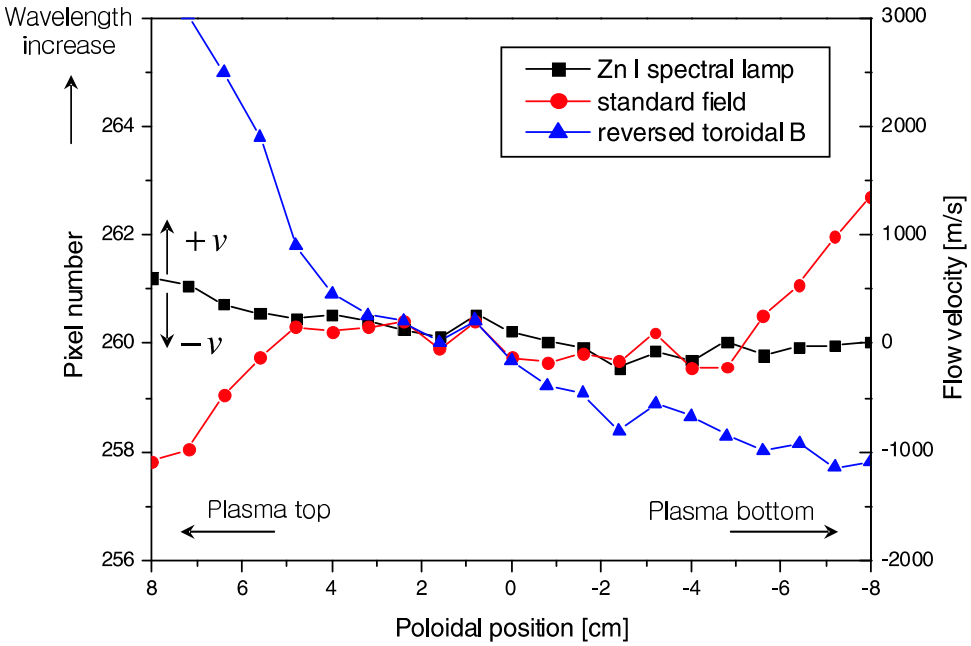

Figure 7.21: Plots of fitted line centers at each viewing chord of the Echelle grating spectrometer. The square-point line in the middle is from a Zn I line at 468.0 nm of a spectral lamp and shows the alignment of the fiber array. When the toroidal magnetic field direction is reversed, the direction of the Doppler line shift (triangle-point) is also reversed. One pixel shift corresponds to a velocity change of 500 m/s. The polarity of the flow velocity is shown on the right hand y-axis. The measured flow velocity is around ±1000 m/s.

To crosscheck this result, we have measured the Doppler shift of the He II lines at 469.6 nm with the Echelle grating spectrometer while viewing the same poloidal plane through a beam splitter in front of the MOSS system as introduced in Section 6.2.2. Figure 7.21 shows the result from the Echelle grating spectrometer. In the middle of the figure the line marked by squares indicates the measured location of the line center of the Zn I line at 468.0 nm of a spectral lamp which was used as a reference for the line shift and thus the flow velocity measurements with the fiber array. The other two lines show the line shift of the He II line at 468.6 nm along the chord number at normal and reversed toroidal magnetic field directions.
When the light source moves a distance vt toward the observer, the Doppler shift is given by

$$\lambda = \lambda_0 \sqrt{\frac{1 + v/c}{1 - v/c}} \tag{7.2}$$

Solving this equation for v gives

$$v = c\sqrt{\frac{\lambda^2 - \lambda_0^2}{\lambda^2 + \lambda_0^2}} \tag{7.3}$$

For the dispersion of 1.11×10^{-3} nm/pixel at 468.6nm, a 1 pixel shift corresponds to a velocity change of 500 m/s. The flow velocity at the top and bottom of the plasma is therefore about $\pm$1000 m/s. This confirms the MOSS measurements.

7.7 Gas mixture

We have reported the results of the Helium plasmas in the previous sections. In this section the MOSS results from mixed-gas plasmas of Hydrogen and Helium are discussed. These are the first mixed-gas experiments performed on WEGA. To do this we modified the gas valve system and controlled the flow of the Helium manually and that of Hydrogen automatically. One goal was to find the gas mixture ratio which maximizes the ion temperature. During the discharges the Hydrogen gas flow rate was decreased uniformly from 8.3 sccm[1] to 6.0 sccm. The Helium gas flow rate was held constant during a discharge, but it was increased on a shot by shot basis. Figure 7.22 shows the trace parameters for 0.5 sccm and 1.0 sccm Helium gas flow rates. While decreasing the Hydrogen gas flow rate, both the electron density and the ion temperature were increased. This behavior is different to that of a pure Helium plasma. For a 1.0 sccm Helium gas flow rate we found that a mixture ratio of 7.4:1 maximizes the density and temperature at given machine control parameters. The electron density was similar to the density observed in a pure Helium plasma, but the ion temperature was approximately 1.0 eV higher.
Figure 7.23 shows the profiles at 20, 23, 30, and 35 s of the 1.0 sccm Helium gas flow discharge shown in Figure 7.22(b). The He II intensity is almost twice as high as in a pure Helium plasma and it clearly shows the LCFS boundary. The ion temperature profile is slightly peaked while the pure Helium plasmas were very flat, and even when the temperature is higher, for example at 20 and 23 s, the width of the profile is getting narrower and thereby closer to the LCFS size. Ion temperature profiles are clearly different from those in pure Helium plasmas.

[1]standard cubic centimeter per minute, 1 sccm = 1.69×10^{-3} Pa $\cdot$ m^3/s

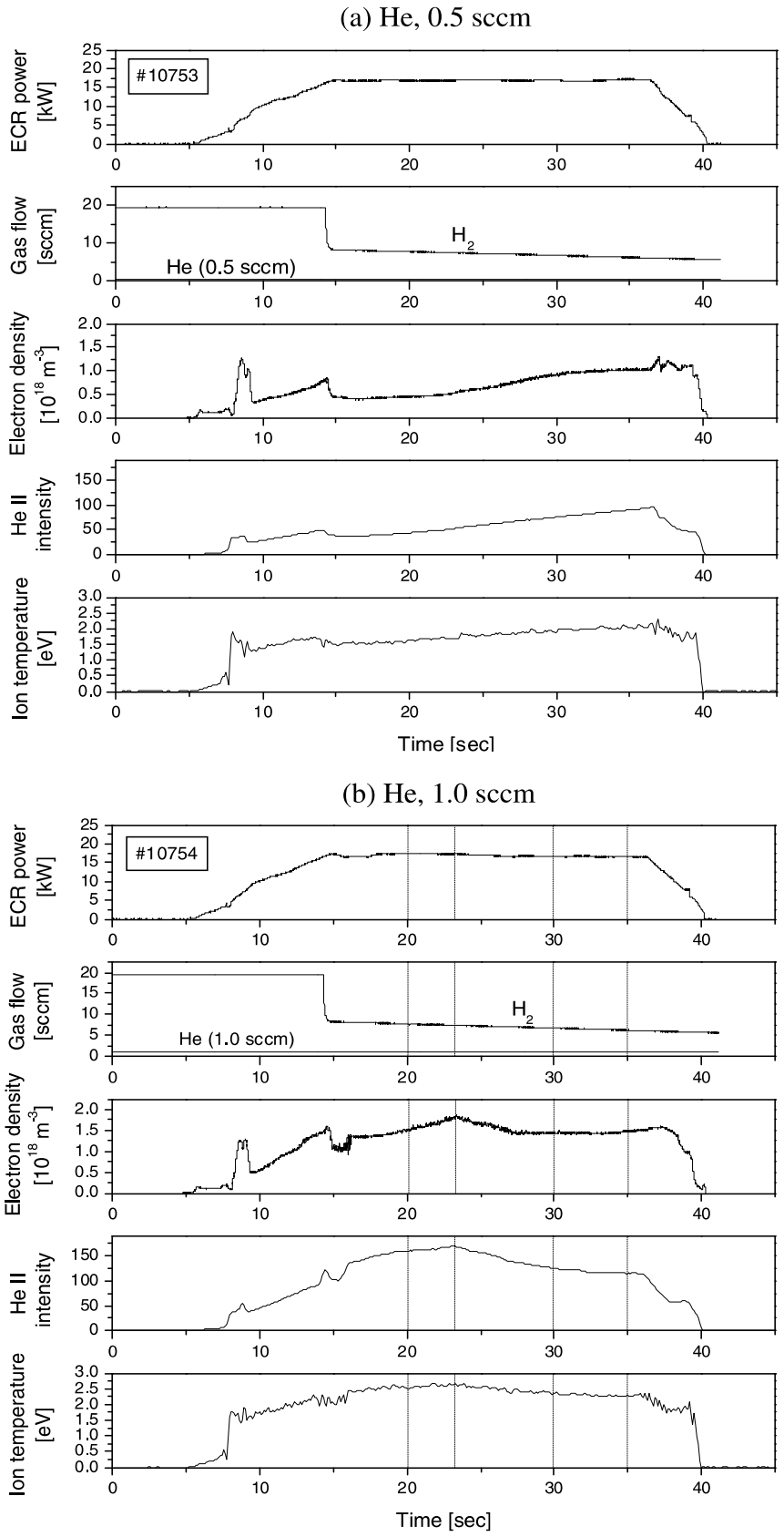

Figure 7.22: Plots of trace parameters of the mixture gas experiment. (a) For a Helium flow rate of 0.5 sccm, the electron density and ion temperature were increased continuously while decreasing the Hydrogen gas flow rate uniformly from 8.3 sccm to 6.0 sccm, (b) but for a 1.0 sccm Helium flow rate with the same Hydrogen flow rate decrease there was a gas mixture ratio of 7.4:1 (at 23 s), that maximize the density and temperature.

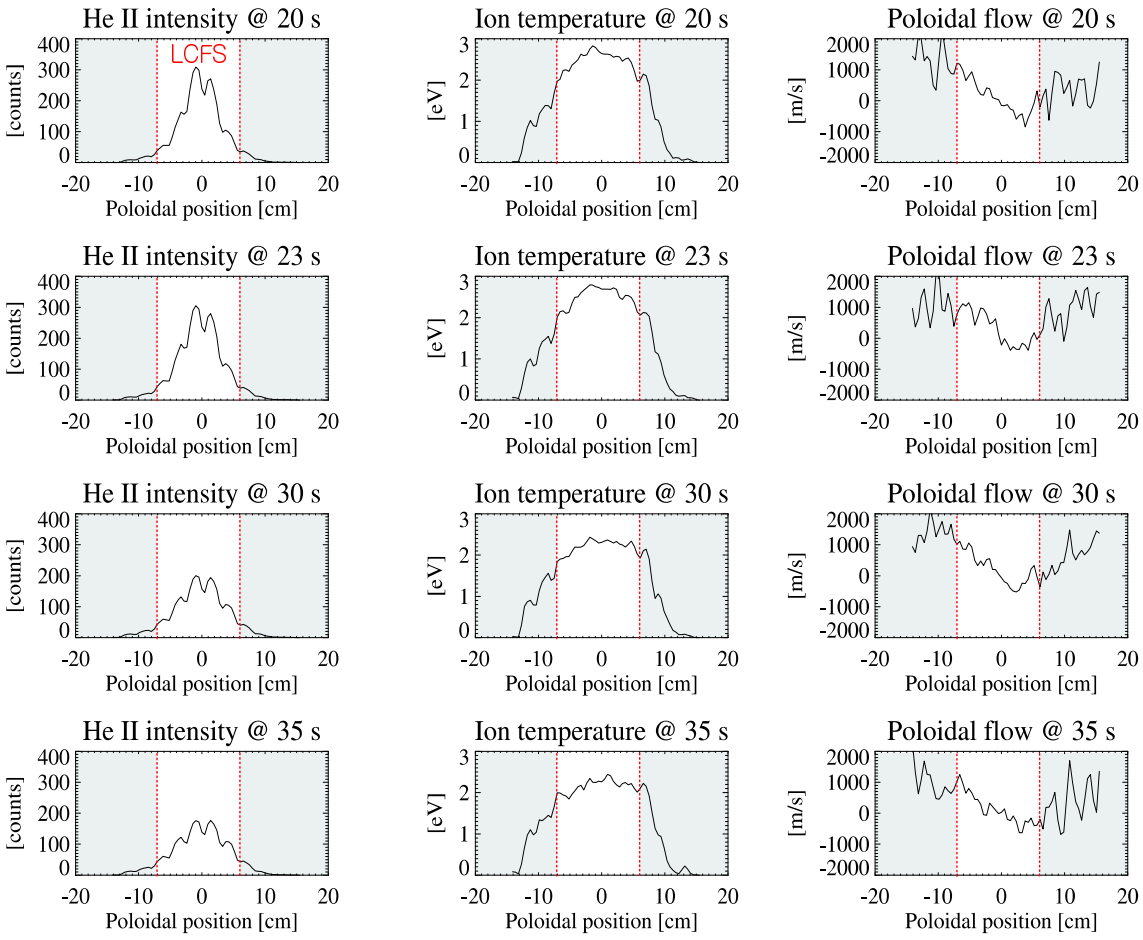

Figure 7.23: Profiles of the He II intensity, ion temperature, and flow velocity at 20, 23, 30, and 35 s of a mixture gas plasma shown in Figure 7.22(b)

8

Discussion

In this chapter we discuss the dependency of profiles on machine control parameter changes such as ECR power, gas flow rate, rotational transform, and the direction of toroidal magnetic field. The status of the ECR heating in WEGA and the estimation of the ion energy confinement time are also discussed, along with further detailed discussion of the poloidal flow.

8.1 Ion temperature behavior in WEGA

In Helium plasmas, when the ECRH power was increased by 400 %, no significant increase of the electron temperature was observed, and the ion temperature increased by only $50 \sim 80$ %. Depending on the wall condition, the maximum ion and electron temperature at the center of plasma with full (26 kW) ECRH power was $1.5 - 2.0$ eV and $7 - 8$ eV, respectively.
Since the WEGA stellarator can be operated with three different gases, H_2, He, and Ar, it affects the plasma condition. When spectral lines of one of these gases still showed up in an overview spectrum for many hours or days after changing the working gas, the ion temperature was always found to be somewhat higher than in the pure gas case. This effect was consistent with the observation that the ion temperature in the gas mixture experiments was always significantly higher. Studies of highly charged ions in gas mixture plasmas have been reported in [54]. According to that study, there are various mixing effects: (a) lowering the average charge state, which reduces the electron loss rate and thereby increases the electron density, (b) ion cooling resulting from the mass effect in ion-ion collisions, (c) increase of the electron density because of the better ionization efficiency of the added gas, and (d) increase of the plasma stability caused by reduction of the plasma potential. Of these effects, the last two effects are probably the cause of the increase in electron density and ion temperature together in the gas mixture experiment. As we have shown in Section 7.3, while decreasing the gas fill pressure, the ion temperature was increased, and at lower gas pressure the plasma potential was smaller. Since this result was from the Helium gas pressure scan experiment we can suppose that the electron

density increase was due to the better ionization efficiency of the added Helium gas and the ion temperature increase was due to the decrease of the Hydrogen gas flow rate during the discharge. A few seconds later, after the maximum temperature and density point at 23 s, the ion temperature decreased while the density slightly increased, as shown in Figure 7.22(b). It was the first gas mixture experiment and there were some technical problems for further experiments. Since the mixed gas plasma produces very interesting results, further investigations are necessary not only experimentally but also theoretically for better understanding.

According to the ion and electron temperature results, the ECR heating in WEGA is not effective. The O-mode heating has a cutoff at the electron plasma frequency, and the electron cyclotron is only accessible for densities below the cutoff, so $n_e < n_c$ is required for collective interaction of the electromagnetic wave with the entire plasma. If $\omega_{pe} > \omega_{in}$, the incident electromagnetic wave interacts only with electrons at the surface of the plasma. The required source frequency for the entire plasma heating in Hz is therefore given by

$$\omega_{in} = \omega_c \geq \omega_{pe} \sim 9\sqrt{n_e} \tag{8.1}$$

where ω_{pe} is the electron plasma frequency and ω_{in} is the ECRH source frequency. The plasma frequency in WEGA is about 12.7 GHz for $n_e = 2 \times 10^{18}$ m^{-3}, which is much larger than the ECRH source frequency at 2.45 GHz. This is probably the main reason for the inefficient ECR heating in WEGA. Figure 8.1 illustrates the

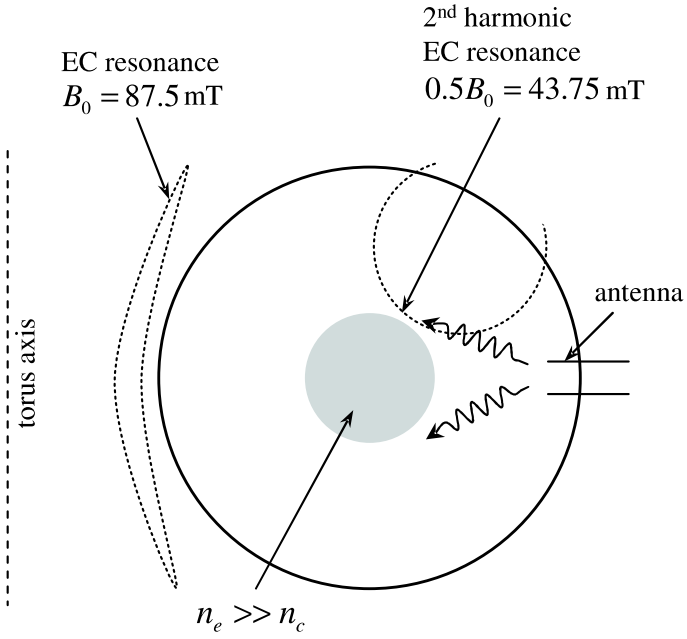

Figure 8.1: Schematic of the location of resonances in the WEGA stellarator. Edge heating using the second harmonic resonance produces the highest temperature plasma within the machine capacity but its efficiency is very low due to the limitation of the heating at densities much higher than the cutoff, $n_e \gg n_c$.

location of resonances which produce the highest temperature plasma within the

machine capacity. We have placed B_0 at the center of the plasma and decreased the magnetic field to half. At $0.6B_0$, the second electron cyclotron resonance layer is located at the top edge as shown in Figure 8.1. The electromagnetic wave interacts only with the edge plasma. At the center of the plasma the heating efficiency is poor due to the lack of resonances.

8.2 Estimation of the ion energy confinement time

Using MOSS and Echelle spectrometers, the ion temperature profiles were measured as a function of time. The MOSS spectrometer has the advantage of good temporal and spatial resolution compared to the grating spectrometer. Here we determine the temporal evolution of the ion confinement time during a discharge as obtained from a power balance equation using measured plasma parameters.
In a plasma it can be expected that energy transfer between ions and electrons must be small since $m_e \ll m_i$. If we consider a direct elastic collision between the two species, we see that

$$\Delta E_{ei} \approx \frac{m_e}{m_i} E_e < \Delta E_{ee} \sim E_e < \Delta E_{ii} \sim E_i \tag{8.2}$$

This tells us that the ion-ion collision is one of the most effective energy transfer mechanisms. However, for an ECR heated plasma, only the electrons respond to the cyclotron waves and only the electrons are heated directly. The ions in this case will be heated collisionally by the energetic electrons.
The importance of collisions is described by the collision time which is the average time it takes for a particle to suffer a collision. For singly charged ions the electron-ion collision time τ_{ei} ($\equiv \nu^{-1}$) is given by [2] :

$$\tau_{ei} = \frac{3}{2}(2\pi)^{3/2} \frac{\varepsilon_0^2 m_i T_e^{3/2}}{n_i m_e^{1/2} e^4 \ln\Lambda} = \frac{m_i}{2m_e}\tau_{ee} \tag{8.3}$$

This is the expression for the collision time of light electrons colliding with heavy ions. $\ln\Lambda = \ln 4\pi n\lambda_D^3$ is the resulting form of the collision impact parameter (Coulomb logarithm) which is calculated by [56]

$$\ln\Lambda = 6.6 - \frac{1}{2}\ln\left(\frac{n[\mathrm{m}^{-3}]}{10^{20}}\right) + \frac{3}{2}\ln T_e[\mathrm{eV}] \tag{8.4}$$

The Coulomb logarithm for Helium plasmas in WEGA is $10.5 - 11.5$. Expressing T in eV, for singly charged ions,

$$\tau_{ei} = 3.16 \times 10^{14} \frac{T_e^{3/2}}{n_i \ln\Lambda} \tag{8.5}$$

$$\tau_{ee} = 3.44 \times 10^{11} \frac{T_e^{3/2}}{n_i \ln \Lambda} \tag{8.6}$$

$$\tau_{ii} = 2.08 \times 10^{13} \frac{T_i^{3/2}}{n_i \ln \Lambda} \tag{8.7}$$

The ion energy confinement time τ_{Ei} is determined by the ion energy power balance equation [57]. We assume that hot electrons transfer their energy to the cold ions only by elastic Coulomb collisions ($T_e > T_i$). Then the power density transferred from electrons to ions is [58]

$$Q_{ei} = \frac{\frac{3}{2} n_e (T_e - T_i)}{\tau_{ei}} \tag{8.8}$$

and the corresponding power density of the ions is

$$P_i = \frac{\frac{3}{2} n_i T_i}{\tau_{Ei}} \tag{8.9}$$

Here the ion energy power balance equation can be written as

$$Q_{ei} - P_i = \frac{n_e (T_e - T_i)}{\tau_{ei}} - \frac{n_i T_i}{\tau_{Ei}} = 0 \tag{8.10}$$

τ_{Ei} is the ion energy confinement time which can also be written as ($n_i \approx n_e$)

$$\tau_{Ei} = \frac{T_i}{T_e - T_i} \tau_{ei} \tag{8.11}$$

Figure 8.2 shows the ion energy confinement time as obtained from Equation (8.11) as a function of time together with trace parameters of a typical plasma discharge in WEGA. Since the electron temperature $T_e = 7 - 8$ eV is measured only at 37 s from a fast Langmuir probe for a radial scan, the electron temperature is assumed to be 4 times higher than the ion temperature during the discharge. The ion energy confinement time is about 0.1 ms at the maximum ECRH power. The confinement time is somewhat higher during ramp up the ECRH power (25 s - 30 s).
The electrons relax to a Maxwellian distribution within a few τ_{ee} followed by ions in a few τ_{ii}. Finally, after a time of τ_{ei}, equilibration of the electron and ion temperatures takes place. Since $\tau_{ei} \gg \tau_{ii} \gg \tau_{ee}$ and the ion confinement time is not only dependent on the electron-ion energy transfer efficiency at a given density but is also related to the total ECRH power due to $\tau_{ei} \propto T_e^{3/2}$, the global and ion energy confinement times should be of the same order.

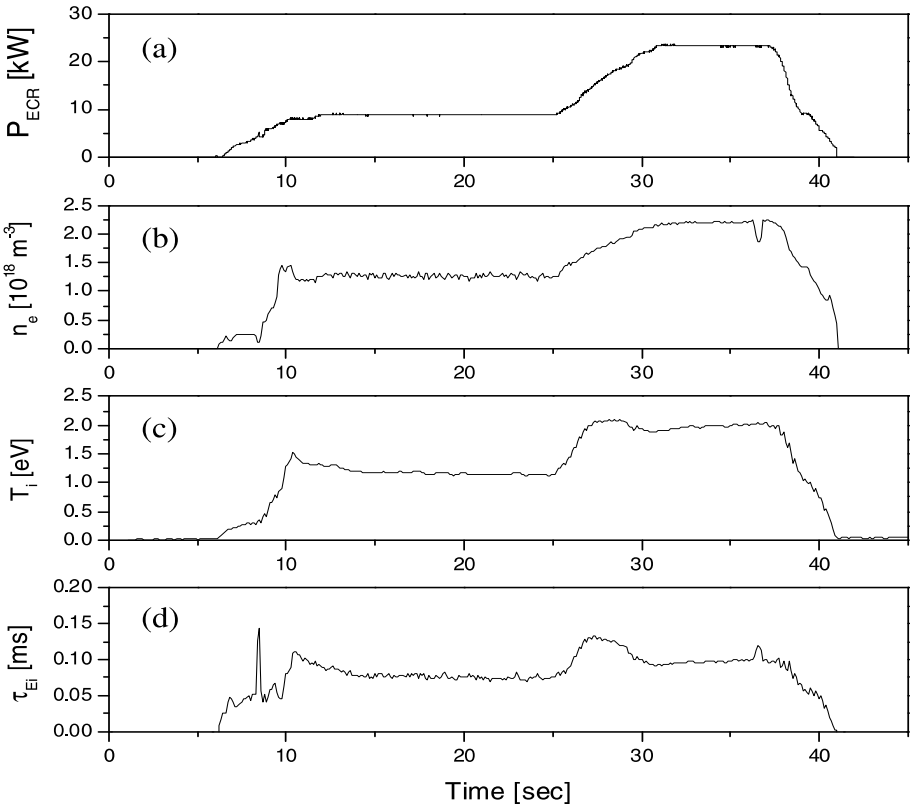

Figure 8.2: Time traces of (a) net ECRH power, (b) electron temperature, and (c) ion temperature, of a typical Helium discharge in WEGA and (d) an estimated ion energy confinement time. The ion energy confinement time is about 0.1 ms at a maximum ECRH power.

8.3 Poloidal rotations in WEGA

The poloidal flow velocity has been measured for a number of different plasma conditions. The plasma flow velocity $\boldsymbol{v}_\perp$ perpendicular to $\boldsymbol{B}$ is given by the sum of the $E \times B$ and diamagnetic drift

$$\boldsymbol{v}_\perp = \frac{\boldsymbol{E} \times \boldsymbol{B}}{B^2} - \frac{\nabla \boldsymbol{p} \times \boldsymbol{B}}{qnB^2} = \boldsymbol{v}_E + \boldsymbol{v}_D \tag{8.12}$$

The direction of the $E \times B$ drift, $\boldsymbol{v}_E$, and the diamagnetic drift for ions, $\boldsymbol{v}_D$, are the same as for the guiding centers because $\boldsymbol{E}$ and $-\nabla \boldsymbol{p}$ point in same direction. Figure 8.3 illustrates the directions of the two drifts for the normal direction of $\boldsymbol{B}_{Tor}$. It is obvious that the direction of the flow changes if $\boldsymbol{B}_{Tor}$ is reversed. This was experimentally demonstrated in WEGA as presented in Section 7.6. The magnitude of $\boldsymbol{v}_D$ in m/s can be computed from the formula [15]

$$\boldsymbol{v}_D = \frac{T}{B}\Lambda^{-1} \tag{8.13}$$

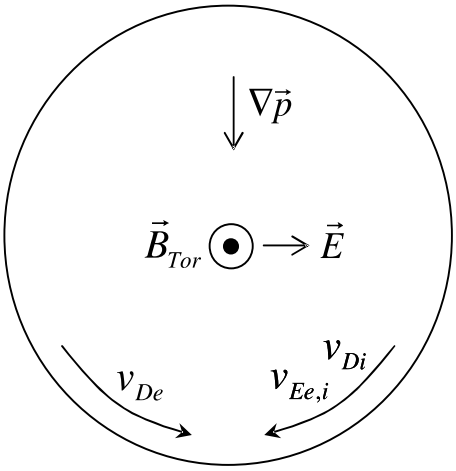

Figure 8.3: Directions of the $E \times B$ and diamagnetic drift for ions and electrons.

where T is in eV, B is in T, and Λ is the density scale length $n/(\partial n/\partial r)$ in m. Since the electron density profile measured with the fast Langmuir probe is flat inside the LCFS, $\boldsymbol{v}_D$ for WEGA is within 10 % of the measured flow velocity of $800 - 1200$ m/s. The measured poloidal flow is therefore mainly due to the $E \times B$ drift. If we write $E = v_E \cdot B$ from the $E \times B$ drift term in Equation (8.12), the expected electric field strength is around $40 - 70$ V/m for $\boldsymbol{v}_E = 800 - 1200$ m/s. This estimation agrees with the measured radial electric field using the fast reciprocating Langmuir probe in Figure 7.14(b).

9

Summary and Conclusions

This thesis has presented design and construction of a 2-dimensional (2D) imaging MOSS (Modulated Optical Solid State) spectrometer and the results of plasma physics investigations in the WEGA stellarator using the MOSS spectrometer.
To design and optimize the MOSS spectrometer properly we have created a coherence simulation code with a model for the He II line at 468.6 nm and the C III line at 464.9 nm. The He II line at 468.6 nm consists of 13 individual lines within a narrow wavelength interval of 0.05 nm which cannot be resolved, and the C III triplet at 464.9 nm is widely separated over an interval of 0.4 nm. Within the model description it is justified to assume the Doppler broadening to be dominant such that the line shape of each individual line is a Gaussian. Since our plasma is confined by magnetic fields, also the Zeeman splitting of the lines had to be included in the simulation model. The simulation was performed for weak (0.1 T) and strong (2.5 T) magnetic field in the temperature range of $0 - 100$ eV. An important notion is the *fringe visibility*, which describes the envelope of the autocorrelation function of the spectrum. It was demonstrated that in principle ion temperatures can be measured even in the case of a complex multiplet or for many individual lines as long as they all have equal width. However, the widely separated multiplet lines in the C III filtered case compared with He II lines result in a more complicated fringe visibility in the time delay. We therefore decided to use the He II line for the first MOSS spectrometer study.
To test the suitability of a MOSS system as a possible W7-X divertor diagnostic, measurements on the partially optimized stellarator W7-AS were done. Wendelstein 7-AS was equipped with an island divertor, which was inspected by the MOSS spectrometer on a preparatory level. After the experimental campaign, the MOSS spectrometer was greatly improved and the development of the design was completed. Firstly, a calibration system for 2D imaging was constructed which provides absolute temperature values with the 3-frame modulation technique. Secondly, to reduce the instrument effect induced by natural birefringence of the electro-optic modulator, the Lithium niobate modulator was replaced by a Lithium tantalate crystal. The improved MOSS spectrometer was installed on the WEGA stellarator to study relatively low temperature plasmas ($T_i < 3$ eV). The experiments on the WEGA

stellarator provided an excellent opportunity to perform a proof-of-principle demonstration of the system performance of the diagnostic concept. Similar temperatures, though at higher densities, are typical also for stellarator divertor experiments. The MOSS spectrometer, however, can also be optimized for high temperature plasma measurements.

The investigations were done by changing the primary machine control parameters such as ECR heating power and neutral gas pressure. The ion temperature of Helium plasmas in WEGA is $1.5 - 2.0$ eV at maximum (25 kW) Electron Cyclotron Resonance Heating (ECRH) power. The He II emission intensity is linearly proportional to the heating power but the ion temperature mainly increases at the outer region of the Last Closed Flux Surface (LCFS) at higher ECRH power. The ion temperature profile becomes broader and flatter as the power is increased. He II emission intensity and ion temperature profiles obviously behave differently, which is related to the fact that the second magnetron (20 kW) seems to heat mainly the plasma edge region. To study the dependencies of ion temperature and poloidal flow on the neutral gas pressure and thereby the ion drag force the gas pressure was varied in the range of the machine for proper steady state discharge operation. It turns out that the width of the He II intensity profile corresponds to the size of the LCFS, and the He II emission intensity increases with increasing gas pressure. The ion temperature increases with decreasing gas pressure and the profiles become flatter. The poloidal flow velocity is negative at the top of the plasma and positive at the bottom of the plasma. The drift speed is around $500 - 1000$ m/s and it is somewhat faster at higher ECRH power.

Magnetic field scan experiments were also carried out to investigate the behavior of the ECR heating in WEGA. The He II line intensity at $0.6\mathrm{B}_0$ (with $B_0 = 87.5$ mT) is almost twice as high as the next highest intensity at $0.5\mathrm{B}_0$. The ion temperature also reached a maximum at $0.6\mathrm{B}_0$ of $T_i = 1.5-2.0$ eV. The ion temperature at $5-10$ cm poloidal position (top position) was similar for $0.5\mathrm{B}_0 - 0.7\mathrm{B}_0$, but only at $0.6\mathrm{B}_0$ the ion temperature has a symmetric profile. The profile is also slightly broader compared to the other cases. The higher ion temperature at $0.6\mathrm{B}_0$ and increased local heating efficiency at the top of the plasma seems to be due to edge plasma heating at the second harmonic resonance. Since the ECRH source frequency at 2.45 GHz is too low to penetrate the plasma at an electron density of 2×10^{18} m^{-3} (cutoff density $n_c = 7.4 \times 10^{16}$ m^{-3}) the microwave heating could only occur in the lower density edge region.

To make sure that the observed velocity was induced by the plasma we reversed the toroidal magnetic field direction. In this case the elliptical cross section of the magnetic flux surface is mirrored. Indeed, the direction of the velocity at the top and the bottom of the plasma reverses if the toroidal magnetic field direction is reversed. To crosscheck the results we measured the Doppler line shift with a conventional Echelle grating spectrometer while also viewing the same poloidal plane using a beam splitter in front of the MOSS spectrometer. The flow speed at the top

and the bottom of the plasma was observed by both diagnostics to be about ±1000 m/s.

We also measured the ion temperature profiles for a two component (H_2+He) neutral gas plasma. To find the relative gas mixture ratio which gives the highest Helium ion temperature, the (dominant) Hydrogen gas flow rate was decreased uniformly from 8.3 sccm to 6.0 sccm. The Helium gas flow rate was kept constant during a discharge but was increased on a shot by shot basis. For a 1.0 sccm Helium gas flow rate, we found that a mixture ratio of 7.4:1 maximizes the density ($n_e = 1.7 \times 10^{18}$ m^{-3}) and ion temperature ($T_i = 2.7$ eV) at given machine control parameters. The He II emission intensity is almost two times higher than in pure Helium plasma and the ion temperature profile is more peaked than in pure Helium plasmas. The poloidal flow is little affected by the Helium contamination of the plasma.

Using the measured plasma parameters the ion energy confinement time is estimated to be around 0.1 ms for Helium plasmas at maximum ECRH power of 26 kW. The poloidal flow in WEGA is shown to be mainly due to the E × B drift.

In conclusion, the capabilities of the newly designed and constructed MOSS spectrometer were successfully demonstrated on the WEGA stellarator. The high throughput MOSS spectrometer provides a 2D distribution of the ion temperature and flow velocity as a function of time, at a 20 times higher time resolution than an Echelle grating spectrometer at a given He II light intensity. Since calibration and demodulation procedures are performed in situ the MOSS spectrometer can be used as a primary *trace* diagnostic for steady state plasma discharges. The 2D imaging capability of the MOSS spectrometer will be very valuable to study the 3D structures of the W7-X island divertor. The high light intensity typically emitted by divertor plasmas will allow the use of fast readout CCD cameras and therefore measurements with significantly higher time resolution. We find the MOSS spectrometer being an advanced Doppler imaging plasma diagnostic with great future potential.

A

Appendix

A.1 Estimation of the Zeeman splitting

The Zeeman effect that occurs for spectral lines resulting from a Zeeman transition between singlet states is traditionally called the Normal Zeeman effect, while that which occurs when the total spin of either the initial or final states, or both, are nonzero is called the Anomalous Zeeman effect for the case of a weak magnetic field. When the magnetic field is sufficiently strong, the Anomalous Zeeman effect is called the Paschen-Back effect. The regime of the two Zeeman effects was discussed in Section 3.3.2.
In this Appendix, the estimation of the Anomalous Zeeman and Paschen-Back effects will be shown for the line emission of the $4d^2D_{5/2} \rightarrow 3p^2P_{3/2}$ He II line. Both line splitting mechanisms are illustrated in Figure 2.1 and 2.2.

A.1.1 Anomalous Zeeman effect

In order to calculate the Anomalous Zeeman effect, recall Equations (2.28) and (2.29)

$$\Delta E = g m_j \left(\frac{e\hbar B}{2m_e} \right) = g m_j \mu_B B \tag{A.1}$$

$$g = 1 + \frac{j(j+1) + s(s+1) - l(l+1)}{2j(j+1)} \tag{A.2}$$

From Equation (A.2) we compute the Landé g factors to use in computing the ΔE values from Equation (A.1) as follows :

For the $4d^2D_{5/2}$ level : $l = 2, s = 1/2, j = 5/2$

$$g_u = \frac{6}{5} \tag{A.3}$$

For the $3p^2P_{3/2}$ level : $l = 1, s = 1/2, j = 3/2$

$$g_l = \frac{4}{3} \tag{A.4}$$

and from Equation (A.1):

For the $4d^2D_{5/2}$ level :

$$\Delta E_u = \frac{6}{5} m_j (5.79 \times 10^{-9}\,\text{eV/gauss}) B \tag{A.5}$$

For the $3p^2P_{3/2}$ level :

$$\Delta E_l = \frac{4}{3} m_j (5.79 \times 10^{-9}\,\text{eV/gauss}) B \tag{A.6}$$

where $5.79 \times 10^{-9}\,\text{eV/gauss}$ is the Bohr magnetron. The longest wavelength line $m_j = +\frac{1}{2} \rightarrow m_j = +\frac{3}{2}$ will have undergone a net energy shift of

$$(3.474 \times 10^{-9} B) - (11.58 \times 10^{-9} B) = -8.106 \times 10^{-9} B \tag{A.7}$$

The shortest wavelength line $m_j = -\frac{1}{2} \rightarrow m_j = -\frac{3}{2}$ will have undergone a net energy shift of

$$(-3.474 \times 10^{-9} B) + (11.58 \times 10^{-9} B) = 8.106 \times 10^{-9} B \tag{A.8}$$

The total energy difference between these two photons is

$$\Delta E_t = \Delta E_u - \Delta E_l = -1.621 \times 10^{-8} B\,\text{eV/gauss} \tag{A.9}$$

Since $\lambda = 1/f = hc/E$, then $\Delta\lambda = -(hc/E^2)\Delta E$, where $E = hc/\lambda$. We then have

$$\Delta\lambda = -\left(\frac{\lambda^2}{hc}\right) \Delta E_t = 0.029\text{Å} \tag{A.10}$$

where $\lambda = 4685.705$ Å, $c = 2.998 \times 10^8$ m/s, $h = 6.62 \times 10^{-34}$ J/s, $1\,\text{eV} = 1.6 \times 10^{-19}$J, and $B = 0.1\,\text{T}$. The Possible quantum numbers in the shell with $n = 1, 2, 3, 4$ are tabulated in Table A.1.

Table A.1: Possible quantum numbers in the shell with $n = 1, 2, 3, 4$

n	l	m_l	m_s	m_j	L	Shell
1	0	0	$\pm 1/2$	$\pm 1/2$	S	K
2	1	1	$\pm 1/2$	$+3/2$	P	L
		0	$\pm 1/2$	$\pm 1/2$		
		-1	$\pm 1/2$	$-3/2$		
3	2	2	$\pm 1/2$	$+5/2$	D	M
		1	$\pm 1/2$	$+3/2$		
		0	$\pm 1/2$	$\pm 1/2$		
		-1	$\pm 1/2$	$-3/2$		
		-2	$\pm 1/2$	$-5/2$		
4	3	3	$\pm 1/2$	$+7/2$	F	N
		2	$\pm 1/2$	$+5/2$		
		1	$\pm 1/2$	$+3/2$		
		0	$\pm 1/2$	$\pm 1/2$		
		-1	$\pm 1/2$	$-3/2$		
		-2	$\pm 1/2$	$-5/2$		
		-3	$\pm 1/2$	$-7/2$		

A.1.2 Paschen-Back effect

The splitting in a strong magnetic field is called the Paschen-Back effect. For example, recall Equation (2.30)

$$\Delta E = (m_l + 2m_s)\left(\frac{e\hbar B}{2m_e}\right) = (m_l + 2m_s)\mu_B \cdot B \tag{A.11}$$

where transitions have to satisfy the selection rules

$$\Delta m_s = 0, \Delta m_l = 0, \pm 1 \tag{A.12}$$

The transition of the $4d^2D_{5/2} \rightarrow 3p^2P_{3/2}$ He II line splits into 9 lines. For example,

For the $4d^2D_{5/2}$ level of $m_j = -5/2$

$$\Delta E_u = -3 \cdot (5.79 \times 10^{-9})B \tag{A.13}$$

For the $3p^2P_{3/2}$ level of $m_j = -3/2$

$$\Delta E_l = -2 \cdot (5.79 \times 10^{-9})B \tag{A.14}$$

The energy difference between the two states is

$$\Delta E_t = \Delta E_u - \Delta E_l = -5.79 \times 10^{-9} B\,\mathrm{eV/gauss} \tag{A.15}$$

Table A.2: Zeeman splitting of the $4d^2D_{5/2} \rightarrow 3p^2P_{3/2}$ He II line at $B = 0.1\,\mathrm{T}$

m_j^{upper}	m_j^{lower}	Polarization	Weak Zeeman	Paschen-Back
-5/2	-3/2	σ	4685.694	4685.694
-3/2	-3/2	π	4685.707	4685.705
-3/2	-1/2	σ	4685.693	4685.694
-1/2	-3/2	σ	4685.719	4685.715
-1/2	-1/2	π	4685.705	4685.705
-1/2	+1/2	σ	4685.692	4685.694
+1/2	-1/2	σ	4685.718	4685.715
+1/2	+1/2	π	4685.704	4685.705
+1/2	+3/2	σ	4685.690	4685.694
+3/2	+1/2	σ	4685.716	4685.715
+3/2	+3/2	π	4685.703	4685.705
+5/2	+3/2	σ	4685.715	4685.715

Table A.3: Zeeman splitting of the $4d^2D_{5/2} \rightarrow 3p^2P_{3/2}$ He II line with various B fields

B [T]	$\Delta\lambda_{weak-Zeeman}$[Å]	$\Delta\lambda_{Paschen-Back}$[Å]
0.1	0.029	0.020
0.5	0.144	0.102
1.0	0.287	0.205
1.5	0.431	0.308
2.0	0.574	0.410
2.5	0.628	0.513
3.0	0.861	0.615

and the line shift at $B = 0.1\,\mathrm{T}$ is

$$\Delta\lambda = -\left(\frac{\lambda^2}{hc}\right)\Delta E_t = 0.0102\text{Å} \tag{A.16}$$

Since $\lambda = 4685.705$Å, the line is shifted to 4685.715Å. All the other lines are tabulated in Table A.2 with the calculated result of the Anomalous Zeeman effect. Table A.3 shows the Zeeman splitting of the line transition with various B field strengths.

A.1.3 Relative intensities of Zeeman components

Since Zeeman components have different values of intensities at each shifted wavelength, the profile of the Zeeman splitting also depends on the relative intensities of each Zeeman component. In Section 3.2.2, the relative intensities of multiplet lines were discussed. Each individual line has a relative line intensity with respect

to the strongest one among them. See, for example, the relative line intensity of the $4d^2D_{5/2} \rightarrow 3p^2P_{3/2}$ transition in Table 3.2. The relative intensity of the line is 0.3646 with respect to the strongest transition, $4f^2F_{7/2} \rightarrow 3d^2D_{5/2}$. The total intensity of all Zeeman components of the transition must be 0.3646. The intensities shown in Figure 2.1 were simply calculated from the rule of the relative line intensities of Zeeman components tabulated in Table 2.2. It doesn't take into account the relative intensity of other individual lines. The correct one which has a total intensity of 0.3646 is shown in Figures 3.11 (anomalous Zeeman) and 3.12 (Paschen-Back) in red.

A.2 Two dimensional Radon transform

To understand the internal structure or property of an object without any damage to it, a variety of proving and reconstruction techniques have been developed in many fields such as physics, astronomy, material science, biology, medicine, etc. Among these fields the success of the technology associated with medical imaging by use of Computerized Tomography (CT) is a good example. The appropriate unifying mathematical framework for a large number of reconstruction techniques is the Radon transform [46]. The Radon transform is used in this thesis to describe any line L for viewing the plasma in a Euclidean coordinate system. In this chapter, the definition of the two-dimensional Radon transform will be introduced. For the three or higher dimensional transform, and their detailed applications, refer to [46].

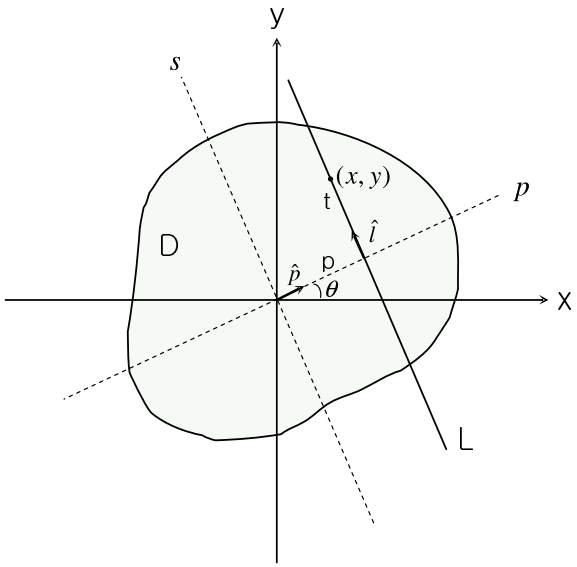

Figure A.1: Line $L(p, \theta)$ through domain $D(x, y)$ and its original (x, y) and rotated (p, s) coordinates.

The internal property of the object may be identified as some function f in an orthogonal coordinate system and the profile may be identified as the Radon transform

of f. If L is any line in the plane, then the mapping is defined as the line integral of f. The two-dimensional Radon transform of f is

$$\check{f}(p,\theta) = \mathbb{R}f = \int_L f(x,y)ds \tag{A.17}$$

where ds is an increment of length along L. The equation of the line L is given by

$$p = x\cos\theta + y\sin\theta \tag{A.18}$$

and the domain D represents an object in the coordinate system, as illustrated in Figure A.1(a). Consider a new coordinate system labelled by p and s which is rotated by the angle θ as indicated in Figure A.1(b). Then the transform can be written as

$$\check{f}(p,\theta) = \int_{-\infty}^{\infty} f(p\cos\theta - s\sin\theta, p\sin\theta + s\cos\theta)ds \tag{A.19}$$

since

$$x = p\cos\theta - s\sin\theta \tag{A.20}$$

$$y = p\sin\theta + s\cos\theta \tag{A.21}$$

Furthermore, in terms of the new unit vectors,

$$\hat{p} = (\cos\theta, \sin\theta) \tag{A.22}$$

$$\hat{l} = (-\sin\theta, \cos\theta) \tag{A.23}$$

equation (A.19) becomes

$$\check{f}(p,\hat{p}) = \int_{-\infty}^{\infty} f(p\hat{p} + t\hat{l})dt \tag{A.24}$$

Note that a scalar parameter t can be found such that $\mathbf{x} = p\hat{p} + t\hat{l}$. The notation $\check{f}(p,\theta)$ and $\check{f}(p,\hat{p})$ may be used interchangeably depending on whether it is desired to emphasize the dependence on the vector $\hat{p}$ or the scalar θ. Finally, note that the equation of the line (A.18) may be written as

$$p = \hat{p}\cdot\mathbf{x} = x\cos\theta + y\sin\theta \tag{A.25}$$

Then the transform may be written as an integral by allowing the Dirac delta function to select line $p = \hat{p}\cdot\mathbf{x}$,

$$\check{f}(p,\hat{p}) = \int f(\mathbf{x})\delta(p - \hat{p}\cdot\mathbf{x})d\mathbf{x} \tag{A.26}$$

This equation is important for extending the transform to three or higher dimensions. For more details, refer to [46].

There is a fundamental connection between the Radon transform and the Fourier transform. For example, if $\check{f}$ is expressed as a function of the radial coordinate p and angular coordinate θ, then

$$\check{f}(u, v) = \int_{-\infty}^{\infty} \check{f}(p, \theta) e^{-i2\pi qp} dp \tag{A.27}$$

with $u = q\cos\theta$ and $v = q\sin\theta$. Here the Fourier transform of f of two real variables is given by

$$\mathcal{F}_2 f = \check{f}(u, v) = \int_{-\infty}^{\infty}\int_{-\infty}^{\infty} f(x, y) e^{-i2\pi(ux+vy)} dxdy \tag{A.28}$$

and the Radon transform of f is given by

$$\mathbb{R}f = \check{f}(p, \theta) = \int_{-\infty}^{\infty}\int_{-\infty}^{\infty} f(x, y)\delta(p - x\cos\theta - y\sin\theta) dxdy \tag{A.29}$$

where δ is the Dirac delta function.

A.3 Derivation of the function $\phi(\theta, \psi)$ for small θ

To derive the phase difference in terms of θ and ψ, recall $\phi(\theta)$ from Equation (4.58)

$$\phi(\theta) = \frac{2\pi L}{\lambda}(n_e\cos\theta_e - n_o\cos\theta_o) \tag{A.30}$$

Here Equation (4.59) can be derived by solving for $\cos\theta_e$ and $\cos\theta_o$ in terms of θ and ψ. To do this, we begin by writing Snell's law for the extraordinary and ordinary rays

$$n_{air}\sin\theta = n_e(\psi)\sin\theta_e \tag{A.31}$$

$$n_{air}\sin\theta = n_o(\psi)\sin\theta_o \tag{A.32}$$

For the extraordinary ray, Equation (A.31) can be written as

$$\frac{\sin\theta}{\sin\theta_e} = n_e(\psi) \tag{A.33}$$

and its inverse square is equal to Equation (4.39). we then obtain

$$\frac{\sin^2\theta_e}{\sin^2\theta} = \frac{\cos^2\phi}{n_o^2} + \frac{\sin^2\phi}{n_e^2} \tag{A.34}$$

Substituting $\sin^2\theta_e = 1 - \cos^2\theta_e$ into the above equation, and rearranging for $\cos\theta_e$ we obtain

$$\cos\theta_e = \sqrt{1 - \frac{\sin^2\theta\cos^2\psi}{n_o^2} - \frac{\sin^2\theta\sin^2\psi}{n_e^2}} \tag{A.35}$$

Similarly, by Equation (A.32)

$$\cos\theta_o = \sqrt{1 - \frac{\sin^2\theta}{n_o^2}} \tag{A.36}$$

Substituting Equations (A.35) and (A.36) into Equation (A.30), we obtain

$$\phi(\theta,\psi) = \frac{2\pi L}{\lambda}\left(n_e\sqrt{1 - \frac{\sin^2\theta\cos^2\psi}{n_o^2} - \frac{\sin^2\theta\sin^2\psi}{n_e^2}} - n_o\sqrt{1 - \frac{\sin^2\theta}{n_o^2}}\right) \tag{A.37}$$

This equation is the phase difference in terms of θ and ψ which was introduced in Equation (4.59). Here, if θ is very small so that $\sin^2\theta$ is much smaller than n_o^2 and n_e^2, then Equation (A.37) can be simplified by using a binomial series,

$$(1+x)^p = 1 + px + \frac{p(p-1)}{2!}x^2 + \cdots \tag{A.38}$$

where $|x| < 1$ and p is any real number. In the case of Equation (A.37), it may be enough to consider only the first and second terms in the series since $p(p-1)/2!$ is $1/8$ and the square root of very small values of x is negligible. Then the terms in the parentheses of Equation (A.37) can be calculated as

$$\begin{aligned}
& n_e\sqrt{1 - \frac{\sin^2\theta\cos^2\psi}{n_o^2} - \frac{\sin^2\theta\sin^2\psi}{n_e^2}} - n_o\sqrt{1 - \frac{\sin^2\theta}{n_o^2}} \\
= \;& n_e\left[1 - \frac{1}{2}\left(\frac{\sin^2\theta\sin^2\psi}{n_e^2} + \frac{\sin^2\theta\cos^2\psi}{n_o^2}\right)\right] - \left[n_o\left(1 - \frac{\sin^2\theta}{2n_o^2}\right)\right] \\
= \;& n_e - n_o - \frac{\sin^2\theta\sin^2\psi}{2n_e} - \frac{n_e\sin^2\theta\cos^2\psi}{2n_o^2} + \frac{n_o\sin^2\theta}{2n_o^2} \\
= \;& n_e - n_o - \frac{\sin^2\theta\sin^2\psi}{2n_e} - \frac{n_e\sin^2\theta\cos^2\psi}{2n_o^2} + \frac{\sin^2\theta\sin^2\psi}{2n_o} + \frac{\sin^2\theta\cos^2\psi}{2n_o} \\
= \;& n_e - n_o + \frac{\sin^2\theta\sin^2\psi}{2}\left(\frac{1}{n_o} - \frac{1}{n_e}\right) - \frac{\sin^2\theta\cos^2\psi}{2}\left(\frac{n_e}{n_o^2} - \frac{1}{n_o}\right) \\
= \;& (n_e - n_o) + \frac{\sin^2\theta\sin^2\psi}{2n_e n_o}(n_e - n_o) - \frac{\sin^2\theta\cos^2\psi}{2n_o^2}(n_e - n_o) \\
= \;& (n_e - n_o)\left[1 - \frac{\sin^2\theta}{2n_o}\left(\frac{\cos^2\psi}{n_o} - \frac{\sin^2\psi}{n_e}\right)\right]
\end{aligned} \tag{A.39}$$

Finally, by Equations (A.37) and (A.39), we obtain

$$\phi(\theta,\psi) \approx \frac{2\pi BL}{\lambda}\left[1 - \frac{\theta^2}{2n_o}\left(\frac{\cos^2\psi}{n_o} - \frac{\sin^2\psi}{n_e}\right)\right] \tag{A.40}$$

This is the function $\phi(\theta,\psi)$ for small θ which was introduced in Equation (4.60).

Bibliography

[1] G. Gamow, *Quantum Theory of the Atomic Nucleus*, Zeitschrift für Physik, 51, 204, (1928)

[2] John Wesson *1977, Tokamaks, 2nd ed.*, Oxford University Press, New York

[3] Spitzer L. Jr. *U.S. Atomic Energy Comission Report*, No. NYO-993 (PM-S-1), (1951)

[4] I. E. Tamm and A. D. Sakharov, *in Plasma physics and the problem of controlled thermonuclear reactions*, (edited by M. A. Leontovich), Pergamon, Oxford, (1961)

[5] M. Otte, J. Lingertat and F. Wagner, *Operation of the WEGA Stellarator with Vertical Field and Compensation Coils*, 30th EPS Conference on Contr. Fusion and Plasma Phys., St. Petersburg, ECA Vol. 27A, P-1.9, (2003)

[6] WVII-A Team, *in Plasma Physics and Controlled Nuclear Fusion Research*, (Proc. 6th Int. Conf. Berchtesgaden, 1976), Vol. 2, IAEA Vienna, 81, (1976)

[7] F. Wagner, et al., *Major Results from Wendelstein 7-AS Stellarator*, Fusion Energy Conference, IAEA, OV2/4, (2002)

[8] J.-H. Feist and the W7-X Construction Team, *Status of WENDELSTEIN 7-X Construction*, 14th International Stellarator Workshop, I.Mo7, (2003)

[9] A. IIYOSHI, et al., *Overview of the Large Helical Device project*, Fusion Energy Conference, IAEA, OV1/4, (1998)

[10] D. van Houtte, et al., *Recent fully non-inductive operation results in Tore Supra with 6 min, 1 GJ plasma discharges*, Nuclear Fusion, 44, L11, (2004)

[11] LEE, G. S., et al., *The KSTAR Project: Advanced Steady-state Superconducting Tokamak Experiment*, Nuclear Fusion, 40, 575, (2000)

[12] A. Sakasai, et al., *Advanced fusion technologies developed for JT-60 superconducting tokamak*, Nuclear Fusion, 44, 329, (2004)

[13] Y. Shimomura, et al., *ITER Overview*, Nuclear Fusion, 39, 1295, (1999)

[14] R. H. Huddlestone and S. L. Leonard, *1965, Plasma Diagnostic Techniques*, Academic Press, New York

[15] Francis F. Chen *1990, Plasma physics and controlled fusion*, Plenum press, New York

[16] D. Salzmann, *1998, Atomic Physics in Hot Plasmas*, Oxford University Press, New York

[17] H. Haken, H. C. Wolf, *2000, The Physics of Atoms and Quata*, Springer, Stuttgart

[18] H. R. Griem, *1964, Plasma Spectroscopy*, McGraw-Hill, New York

[19] W. Lochte-Holtgreven*1995, Plasma Diagnostics*, AIP press, Woodbury, NY

[20] G. W. F. Drake *1996, Atomic, Molecular, and Optical Physics Handbook*, AIP Press, Woodbury, NY

[21] G. Bekefi *1976, Principle of Laser Plasmas*, Wiley, New York

[22] Peter A. Jansson *1984, Deconvolution with Applications in Spectroscopy*, Academic Press, London

[23] F. Schreier, *The Voigt and complex error function: A comparison of computational methods*, J. Quant. Spectrosc. Radiat. Transfer 48, 743, (1992)

[24] H. R. Griem, *1974, Spectral Line Broadening by Plasmas*, Academic Press, New York

[25] P. A. Tipler, R. A. Llewellyn, *1999, Modern Physics*, W. H. Freeman and Company, New York

[26] H. A. Bethe, E. E. Salpeter, *1977, Quantum Mechanics of One- And Two-Electron Atoms*, Plenum Publishing Corporation, New York

[27] D. H. Sampson, *On statistical equilibrium among the sublevels of hydrogenic atoms and ions*, J. Phys. B : Atom. Molec. Phys., Vol. 10, No. 5, (1977)

[28] John Hey *Multiplet oscillarator strengths and transition probabilities for neutral oxygen*S. -Afr. Tydskr. Fis. 10, 118, (1987)

[29] W. L. Wiese, M. W. Smith, B. M. Glennon *1966, Atomic Transition Probabilities, Volume I Hydrogen Through Neon*, NSRDS, Washington D.C. Berlin

[30] Stanley Bashkin and John O. Stoner, Jr. *1975, Atomic energy levels and Grotrian diagrams*, American Elsevier Publishing Company, New York

[31] Igor I. Sobelman *1979, Atomic Spectra andRadiative Transitions*, Springer-Verlag, Berlin

[32] John Howard, *Vector tomography applications in plasma diagnostics*, Plasma Physics and Controlled Fusion 38, 489, (1996)

[33] John Howard, *Modulated optical solid-state spectrometer applications in plasma diagnostics*, Review of Scientific Instrument 70, 368, (1999)

[34] J. Howard, C. Michael, F. Glass, and A. D. Cheetham, *Optical coherence techniques for plasma spectroscopy*, Review of Science Instrument 72, 888, (2001)

[35] John Howard, *Electro-optically modulated polarizing Fourier-transform spectrometer for plasma spectroscopy applications*, Applied Optics 41, 197, (2002)

[36] C. A. Michael, J. Howard, and B. D. Blackwell, *The MOSS camera on H-1NF*, Review of Scientific Instrument 72, 1034, (2001)

[37] James C. Wyant, *Fringe localization*, Applied Optics 17, 1853, (1978)

[38] Grant R. Fowles, *1975, Introduction to modern optics*, Holt, Rinehart and Winston, New York

[39] Amnon Yariv and Pochi Yeh, *1984, Optical Waves in Crystals - Propagation and Control of Laser Radiation*, John Wiley and Sons, New York

[40] Max Born and Emil Wolf, *1975, Principle of Optics*, Pergamon Press, Oxford

[41] J. V. Hofmann, et al., *Stellarator optimization studies in W7-AS*, Plasma Phys. Control. Fusion, 38, A193, (1996)

[42] P. Grigull, et al., *First island divertor experiments on the W7-AS stellarator*, Plasma Physics and Controled Fusion 43, A175-A193, (2001)

[43] R. König, et al., *Island divertor spectroscopy at the Wendelstein W7-AS stellarator* Rev. Sci. Instrum, 74, 3, 2052, (2003)

[44] D. Dorst, *2000, WEGA-Experimeten im IPP / TI Greifswald*, IPP/E3, Greifswald

[45] W. H. Steel, *1983, Interferometry*, Cambridge University Press, Cambridge

[46] Stanley R. Deans, *1993, The Radon transform and some of its applications*, Krieger publishing company, Malabar, Florida

[47] R. S. Weis and T. K. Gaylord, *Lithium Niobate: Summary of Physical Properties and Crystal Structure*, Applied Physics A 37, 191, (1985)

[48] Anthony J. Servizzi, Joseph T. Boyd, S. Sriram, and Stuart A. Kingsley, *Extraordinary-mode refractive-index change procuded by the linear electro-optic effect in $LiNbO_3$ and reverse-poled $LiNbO_3$*, Applied Physics 34, 4248, (1995)

[49] M. Otte, J. Lingertat, and F. Wagner, *Operation of the WEGA Stellarator with Vertical Field and Compensation Coils*, 30th EPS Conference on Plasma Phys. and Contr. Fusion, P-1.10, (2003)

[50] Technical note 6, *ECHELLE CRATINGS*, Spectra-Physics, New-York

[51] Melles Griot, *1999, The practical application of light*, Melles Griot inc.

[52] Kinga Horvath, *2004, Private Communications*

[53] Y. Podoba, K. Horvath, H.P. Laqua, J. Lingertat, and F. Wagner, *Electron cyclotron heating at the WEGA stellarator*, 14th International stellarator workshop, P.M027, (2003)

[54] A. G. Drentje, et al., *Role of low charge state ions in electron cyclotron resonance ion source plasmas*, Review of Scientific instruments, Vol. 71, No. 2, 623, (2000)

[55] H. P. Laqua, et al., *Resonant and Nonresonant Electron Cyclotron Heating at Densities above the Plasma Cutoff by O-X-B Mode Conversion at the W7-AS Stellarator*, Physical review letters, Vol. 78, No. 18, 3467, (1997)

[56] T.J.M. Boyd and J.J.Sanderson, *2003, The physics of plasmas*, Cambridge University Press, Cambridge

[57] R. Balbin, et al., *Ion confinement studies on the TJ-II stellarator*, 14th International Stellarator Workshop, P.We1, (2003)

[58] C. Lechte, J. Stöber, and U. Stroth, *Plasma parameter limits of magnetically confined low temperature plasmas from a confined particle and power balance*, Physics of plasmas, Vol. 9, No. 6, 2839, (2002)

Acknowledgements

First and foremost, I have sincere gratitude to Prof. Thomas Klinger and Prof. Friedrich Wagner who allowed me to join the excellent International Max-Planck Research School (IMPRS) in IPP Greifswald. It was a great opportunity to realize my long-cherished dream of becoming a physicist.
I would like to thank again Prof. Thomas Klinger, my academic supervisor or Doktorvater in German, who was always very kind to me, and I learned many things from him. His word always inspired me to further efforts.
I would like to express my gratitude to my scientific supervisor, Dr. Ralf König, for kindly providing guidance throughout my study. It was a great pleasure to me to conduct this thesis under his supervision.
I have great pleasure in expressing my deep sense of gratitude and indebtedness to Dr. John Howard at the Australian National University (ANU) whose comments were always of the greatest help.
My sincere gratitude goes to Dr. Johann Lingertat, Dr. Matthias Otte, Mr. Dieter Aßmus, and Ms. Kinga Hovart who made almost 700 plasma shots in WEGA for me. I would never have finished my study without their help.
I am grateful to Dr. Clive Michael at ANU, Dr. Andreas Dinklage, Dr. Jürgen Baldzuhn, Dr. Martin Schmidt, and Dr. Andreas Werner for answering my questions.
I am also grateful to Mr. Klaus Grosser and Andre John for their technical support.
I owe my deep regards to Dr. Henning Thomsen and Dr. Neil McTaggart for valuable suggestions, guidance and constant encouragement to bring this thesis to the present form.
Needless to say, I am grateful to all of my colleagues at IPP Greifswald and the IMPRS. I am especially thankful to Mani (Dr. Narayanan Ramasubramanian) who was my best friend during my time in Germany.
I would also like to thank Kyu-Dong and Jacob who shared a big office with me during the last several months. We have discussed many useful things during our daily life.
Finally, I acknowledge my parents whose inspirations made me work hard. This thesis I dedicate to my parents.